ABSTRACT

LUGO, RAFAEL ANDRES. Statistical Entry, Descent, and Landing Flight Reconstruction with Flush Air Data System Observations using Inertial Navigation and Monte Carlo Techniques. (Under the direction of Dr. Robert Tolson.)

A method is introduced to consider flush air data system (FADS) pressures using a technique based on inertial navigation to reconstruct the trajectory of an atmospheric entry vehicle. The approach augments the recently-developed Inertial Navigation Statistical Trajectory and Atmosphere Reconstruction (INSTAR), which is an extension of inertial navigation that provides statistical uncertainties by utilizing Monte Carlo dispersion techniques and is an alternative to traditional statistical approaches to entry, descent, and landing trajectory and atmosphere reconstruction.

The method is demonstrated using flight data from the Mars Science Laboratory (MSL) entry vehicle, which contained an inertial measurement unit and a flush air data system called the Mars Entry Atmospheric Data System (MEADS). An MSL trajectory and atmosphere solution that was updated using landing site location in INSTAR is first presented. This solution and corresponding uncertainties, which were obtained from Monte Carlo dispersions, are then used in a minimum variance algorithm to obtain aerodynamic estimates and uncertainties from the MEADS observations. MEADS-derived axial force coefficient and freestream density estimates and uncertainties are also derived from the minimum variance solutions independent of the axial force coefficients derived from computation fluid dynamics (CFD), which have relatively high *a priori* uncertainty. Results from probabilistic analyses of the solutions are also presented.

This dissertation also introduces a method to consider correlated CFD uncertainties in INSTAR. From *a priori* CFD uncertainties, CFD force and pressure coefficients are dispersed in a Monte Carlo sense and carried over into the reconstructions. An analysis of the subsequent effects on the trajectory, atmosphere, and aerodynamic estimates and statistics is presented.

Trajectory, atmospheric, and aerodynamic estimates compare favorably to extended Kalman filter solutions obtained by the MSL reconstruction team at NASA Langley Research Center. The uncertainties obtained through the methods from this work are generally smaller in magnitude because of assumptions made regarding sources of error in the MEADS pressure transducer uncertainties. Using data-derived uncertainties in the pressure measurement noise covariance results in aerodynamic parameter estimate uncertainties that are in better agreement with the uncertainties derived from the Monte Carlo dispersions. CFD database errors dominate the uncertainties of parameters derived from aerodatabase axial force coefficients.

Statistical Entry, Descent, and Landing Flight Reconstruction with Flush Air Data System Observations using Inertial Navigation and Monte Carlo Techniques

by
Rafael Andres Lugo

A dissertation submitted to the Graduate Faculty of
North Carolina State University
in partial fulfillment of the
requirements for the Degree of
Doctor of Philosophy

Aerospace Engineering

Raleigh, North Carolina

2014

APPROVED BY:

Robert Tolson Chair of Advisory Committee	Fred DeJarnette
Andre Mazzoleni	Paul Ro

ProQuest LLC.
789 East Eisenhower Parkway
P.O. Box 1346
Ann Arbor, MI 48106 - 1346

Biography

Rafael Lugo was born on July 18th, 1985 to Gabriel and Ana Maria Lugo in Wilmington, North Carolina. He is the older brother of Miguel Lugo. Having attended Snipes Elementary School, D.C. Virgo Middle School, and New Hanover High School, Rafael was accepted to North Carolina State University in 2003. He graduated with a Bachelor of Science in aerospace engineering in the spring of 2007, and was subsequently accepted into NC State University's graduate school. He conducted his graduate research at NASA Langley Research Center in Hampton, Virginia through a joint venture with NC State University and the National Institute of Aerospace. He received his Master of Science degree in aerospace engineering in the spring of 2011. Through this program Rafael worked with NASA Langley's Atmospheric Flight and Entry Systems Branch and participated in materials testing for inflatable atmospheric decelerators, scale model aeroballistic testing for both the Crew Exploration Vehicle and Mars Science Laboratory, and most recently, Mars Science Laboratory trajectory reconstruction. Rafael currently resides in Hampton.

Acknowledgements

First and foremost, I am extremely grateful for the time, effort, and guidance my advisor, Dr. Robert Tolson, dedicated to me and my work. I am honored and privileged to have been able to work with him these past few years. I am also indebted to Robert Blanchard of the National Institute of Aerospace, who has devoted a great deal towards helping me in my research. I consider myself very fortunate to have been inspired by the experience, intuition, and kindness of both of these gentlemen.

Dr. Chris Karlgaard and Prasad Kutty (Analytical Mechanics Associates, Inc.) were also instrumental by providing many insightful discussions, suggestions, and reviews. I am indebted to my NASA mentor, Mark Schoenenberger (NASA Langley Research Center), who directed the aeroballistic testing that would eventually become the framework of this dissertation and offered a great deal of technical support. I feel it a privilege to have been able to work with him. I also thank Michelle Munk (NASA Langley Research Center) for programmatic support.

I extend special thanks to my committee members, Dr. Andre Mazzoleni, Dr. Fred DeJarnette, and Dr. Paul Ro (North Carolina State University), for their time, understanding, and support. I was fortunate to have Dr. Mazzoleni and Dr. DeJarnette as instructors for several undergraduate and graduate courses, and as I consider the work presented here a culmination of my academic career, it is not an exaggeration to say that I could not have done this without them.

I thank Chris Kuhl, Dr. Michael Hemsch (NASA Langley Research Center), and John Van Norman (Analytical Mechanics Associates, Inc.) for insightful discussions and comments on pressure transducers and computational fluid dynamics. I am also grateful to my first NASA mentor at Langley, Steven Hughes, who introduced me to the way things work at NASA.

The NC State and NIA administration and staff were also very supportive, and I am grateful for their time and effort. The work presented in this dissertation was supported by NASA Cooperative Agreements NNX12AF93A and NNL09AA00A.

Many thanks are due to my friends and fellow graduate students Michael Grimes, Chris Jones, Erik Axdahl, Patrick Chai, Steven Tobin, Lindsey Barr, Charlie Cimet, Alex Stramel, Jessie Quinlan, Nicole Pothier, Duncan McGillivray, Jamie Wilson, Morgan Silverman, Audrey Staples, Scott Bednar, Casey Thomas, and John Gaebler for helping me make it through graduate school in one piece. I am particularly grateful to Dr. Lynn Huh for his friendship throughout my graduate school career. I am lucky to have had friends that shared the same trials and tribulations.

Finally, I am most grateful to my family and loved ones, who have unwaveringly supported me these many years through college and graduate school, and beyond. To my parents Gabriel and Ana Maria, my brother Miguel, and my girlfriend Caitlin, I say thank you—for everything—and I love you.

Table of Contents

List of Tables

List of Figures

List of Abbreviations

Abbreviations

CDF	cumulative distribution function
CEV	Crew Exploration Vehicle
CG	center of gravity
CM	center of mass
EDL	entry, descent, and landing
EI	entry interface
FADS	flush air data system
GNC	guidance, navigation, and control
GPS	Global Positioning System
IMU	inertial measurement unit
INSTAR	Inertial Navigation Statistical Trajectory and Atmosphere Reconstruction
J2000	Julian date at noon, 1 January 2000
LAURA	Langley Aerothermal Upwind Relaxation Algorithm
LS	least squares
MEMS	micro electro-mechanical system
MER	Mars Exploration Rover
MLE	maximum likelihood estimator, maximum likelihood estimate
MPF	Mars Pathfinder
MSL	Mars Science Laboratory
MEADS	Mars Entry Atmosphere Data System
MEDLI	Mars Entry Descent and Landing Instrumentation
MVAP	minimum variance with *a priori*
NASA	National Aeronautics and Space Administration
PDF	probability distribution function
SSE	Sensor Support Electronics
TLNS	thin layer Navier-Stokes
TPS	thermal protection system

Coordinate frames

CS	cruise stage frame
DS	descent stage frame
EME2000	Mars-centered Earth mean equator and equinox of J2000 frame
M	Mars-centered Mars mean equator and prime meridian of t_0 frame
MME2000	Mars-centered Mars mean equator and prime meridian of J2000 frame
R	rover frame
SC	spacecraft frame
b	body frame

List of Nomenclature

Scalars

A	axial force, integrator constant
B	bias, integrator constant
C	non-dimensional coefficient
J_2	second dynamic form factor (zonal harmonic)
L	lift, bias limit
M	Mach number
$\mathcal{M}$	molar mass
N	normal force, number of Monte Carlo dispersions
NL	nonlinearity
O	observation
P	atmospheric pressure
Q	ascending node of the Mars mean equator of date plane with respect to the Earth mean equator of J2000 plane
R	planet radius
$\mathcal{R}$	gas constant
S	maximum cross-sectional area of vehicle normal to axis of symmetry
SF	scale factor
T	atmospheric temperature
X	inertial frame position vector component, random observation
Y	inertial frame position vector component, side force
Z	inertial frame position vector component
a	speed of sound, pressure transducer bias, minimum bound of uniform distribution, integrator constant
b	pressure transducer scale factor, maximum bound of uniform distribution, integrator constant
c	pressure transducer nonlinearity
d	maximum diameter of spacecraft
h	altitude, bin width, bandwidth
k	number of variables, number of bins
l	rolling moment
m	pitching moment, mass
n	yawing moment, number of observations
p	roll rate
q	pitch rate, dynamic pressure
r	yaw rate, distance between center of planet and spacecraft, radius
t	time
u	body frame velocity vector component
v	body frame velocity vector component, volume
w	body frame velocity vector component
x	random variable

Ω	planetary rotation rate
ε	random value
γ	ratio of specific heats
μ	mean, standard gravitational parameter
ρ	atmospheric density, magnitude of position vector, correlation
σ	standard deviation, variance, uncertainty

Vectors

F	total force
M	total moment
a	acceleration
d	eigenvalues
e	Euler axis
g	acceleration due to gravity
i, **j**, **k**	unit vectors
q	quaternion
r	position
v	velocity
x	state
y	measurements, observations
ε	measurement errors
μ	*a priori* state, mean value
ω	angular velocity of spacecraft

Matrices

A, B	sensitivity matrix
C	transformation matrix
I	identity matrix
R	correlation matrix
V	array of eigenvectors
W	weighting matrix
Γ	covariance matrix

Angles

α	angle of attack, right ascension
β	angle of sideslip
δ	declination
ϕ	roll, sensor misalignment, latitude, phase angle
γ	flight path angle
λ	right ascension
η	cone angle
θ	pitch, incidence angle, longitude
ψ	yaw
ζ	clock angle

Subscripts/Superscripts

T	total, matrix transpose
b	body frame
f	final time or condition
i	initial time or condition, ith component of vector or series
n	inertial frame
ref	reference condition
t	total
x, y, z	Cartesian vector components
∞	freestream, ambient, or static conditions
0	initial time or condition

Functions

E	expected value or expectation
F	probability distribution function
J	cost function
$\mathcal{N}$	normal distribution
Pr	probability
p	probability density function
U	uncertainty function
G, f, g	general functions
ϕ	normal probability density function
Φ	normal cumulative distribution function

Miscellaneous

Δ	arbitrary interval
δ	infinitesimal interval
$\dot{x}$	(dot embellishment) time rate of change dx/dt
$\tilde{x}$	(tilde embellishment) measured quantity
$\hat{x}$	(carat embellishment) estimated quantity, unit vector
$\overline{x}$	(bar embellishment) modeled quantity
$\breve{x}$	(arc embellishment) dispersed quantity

Chapter 1: Introduction

> **NAVIGATION** (nævə'geɪʃ(ə)n), *n*. [late 13th cent. Old French] The art or science of directing the movements of an aircraft or spacecraft, esp. with regard to the determining of position and course by the use of instruments, electronic aids, etc.
>
> *Oxford English Dictionary, Third Edition*

> I am well convinced that Aerial Navigation will form a most prominent feature in the progress of civilization.
>
> *George Cayley, aeronautical engineer, 1804*

Guidance, navigation, and control, often abbreviated GNC, is a broad field of engineering that is of particular importance in autonomous vehicles. *Guidance* is the process of directing a vehicle from the present location to the destination. *Navigation* is the process of determining the present location of a vehicle relative to the destination using estimates and observations of the current state and surroundings. *Control* is the process of maintaining the course and stability of the vehicle. Whether it is a sailboat crossing an ocean or a satellite orbiting a planet, the process of determining the vehicle state is essential for accurate navigation, and is the fundamental component of this dissertation.

Many navigation techniques exist, some of which date back centuries. Ancient mariners used *dead reckoning*, a technique in which position is determined by taking into account the ship's present speed and course heading at regular intervals, using the classical $distance = speed \times time$.[1] Dead reckoning is particularly susceptible to accumulation errors since errors in position and velocity estimates affect later estimates when no information about the surroundings or environment is used. Despite this danger, however, the technique has been used successfully for centuries. Perhaps most

famously, Christopher Columbus made four voyages from Spain to the so-called New World using only dead reckoning, returning each time with exceptional accuracy.[2] These are shown in Figure 1.1.

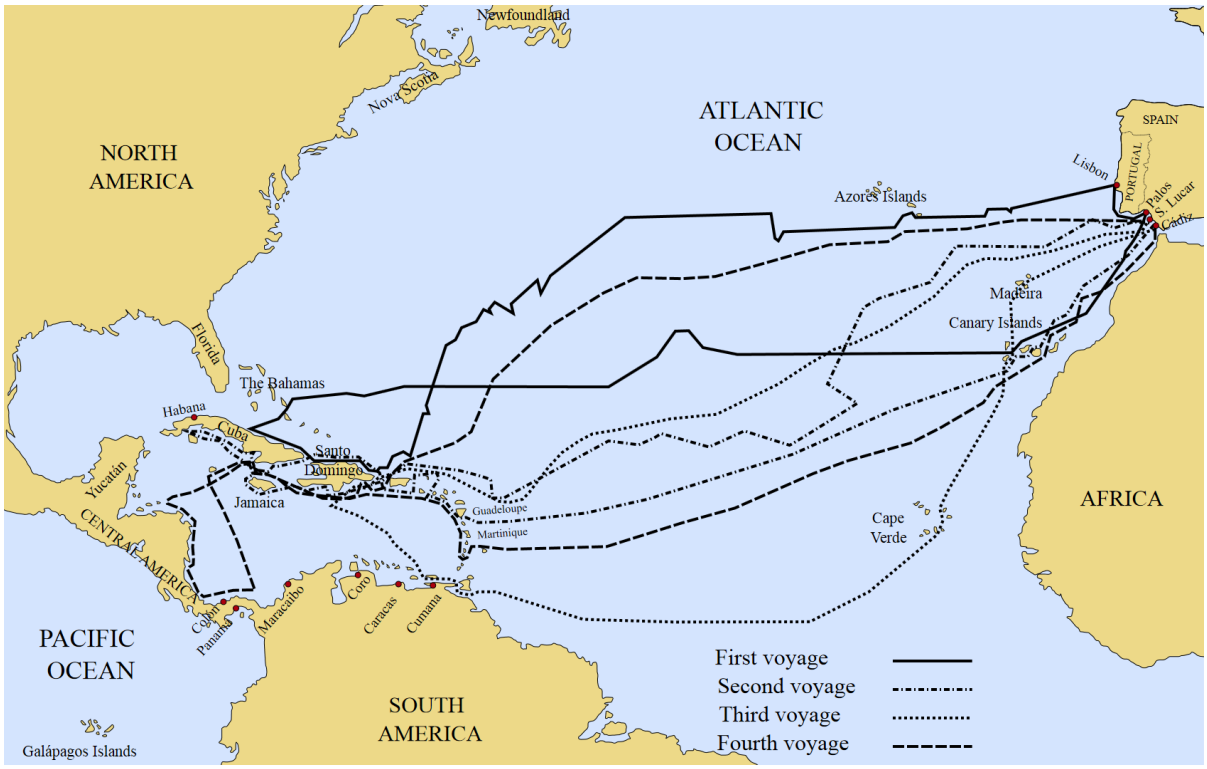

Figure 1.1. The four voyages of Christopher Columbus, navigated using dead reckoning.[*]

Eventually it was discovered that the angles between the stars in the sky and the local horizon could be used with yearly celestial almanacs to obtain an estimate, or fix, of the ship's current location independent of previous position estimates, thus correcting or eliminating accumulation errors. This resulted in the method of *celestial navigation*.[2]

The rise of powered flight and the early rocketry work of Robert Goddard in the early 20th Century spurred development of automated navigation methods that relied on data from sensors located onboard the vehicle.[†] Austrian engineer Johannes Boykow formulated such a technique in the

[*] http://en.wikipedia.org/wiki/Voyages_of_Christopher_Columbus, accessed 25 March 2013.

[†] Although mathematical formulations of sensor-based navigation did not begin in earnest until this time, in 1873 the Irish scholar and philosopher Joseph John Murphy wrote a letter to the journal *Nature* in which he described, as a response to a letter on animal navigation by Charles Darwin, a process by which the position and heading of a train carriage could be obtained by tracking and integrating the movements of a free-swinging ball suspended from the roof of the carriage.

late 1920s, but was unable to demonstrate it successfully with contemporary instruments before his death in 1935.[3] It was not until late 1944 that Wernher von Braun, technical director of the Nazi V-2 rocket program, implemented a variation of Boykow's method to guide missiles to their targets using onboard gyroscopes and an accelerometer. The V-2 GNC system, while effective, was crude in that it was designed simply to maintain a stable, roughly vertical flight to a certain altitude. After World War II and the relocation of von Braun and his engineers to the United States, Cold War fueled interest in self-guided intercontinental ballistic missiles (ICBMs) led a team headed by Charles Draper of MIT to refine and formalize the method into the now-standard *inertial navigation*. Draper's designs, informed by the V-2 systems, were implemented with increasingly accurate sensors in a variety of vehicles in the 1950s and 1960s, including the Atlas ICBM and the Apollo spacecraft. Today, inertial navigation is still extensively used in terrestrial, marine, aerial, and space applications.[4]

Inertial navigation requires the use of three mutually orthogonal accelerometers and three mutually orthogonal gyroscopes typically contained in a single package called an inertial measurement unit[*] (IMU). By numerically integrating acceleration and angular rate measurements provided by these sensors, the vehicle position, velocity, and attitude may be continuously propagated from an initial state, which is in turn fed to the navigation computer to update guidance and control routines.[4] Thus, despite tremendous advances in technology[†] since the days of sextants and almanac table lookups, inertial navigation is essentially a much more accurate version of dead reckoning.

Modern navigation systems often augment IMU data with information from other sources. Terrestrial vehicles, for example, use the Global Positioning System (GPS), a network of Earth satellites broadcasting radio timing signals that are used to quickly determine the present location of the GPS receiver to within a few meters.[5] Spacecraft such as interplanetary probes, however, must rely on internal sensors, radiometric tracking from Earth ground stations, or—paralleling the terrestrial form of celestial navigation—known and fixed star positions to determine the current state.

In modern times, a significant navigation challenge has been the robotic exploration of Mars and its atmosphere.[6] Beginning in the 1970s, NASA has successfully landed seven surface assets in the form of landers and rovers: Viking 1 & 2 (landed 20 July & 3 September 1976), Mars Pathfinder (4 July 1997), Mars Exploration Rover A & B (4 & 25 January 2004), Mars Phoenix (25 May 2008), and Mars Science Laboratory (6 August 2012). Placing these rovers and landers on the surface

---

Unfortunately, Murphy postulated that while such a device may work in theory, "such delicacy of mechanism is not to be hoped for." (Murphy, J. J., "A Mechanical Analogy," *Nature*, 1873.)

[*] Also referred to as an inertial reference unit (IRU) or, when coupled with a navigation computer, an inertial navigation system (INS).

[†] Early IMUs, such as those aboard the Apollo spacecraft, were gimbaled, meaning that they were isolated and stabilized from the vehicle using gyroscopes. While this simplified the navigation algorithms at a time when portable computing power was at a premium, the units were bulky and had many moving parts. Most modern IMUs are strapdown, meaning that they are attached to the "rigid body" of the vehicle, and many utilize micro electro-mechanical system (MEMS) technology that result in cheaper units that can fit on platforms as small as a smartphone, but require more complex computations.

requires the vehicle to go through an entry, descent, and landing (EDL) sequence through the Mars atmosphere. A notional Mars EDL sequence is shown in Figure 1.2.

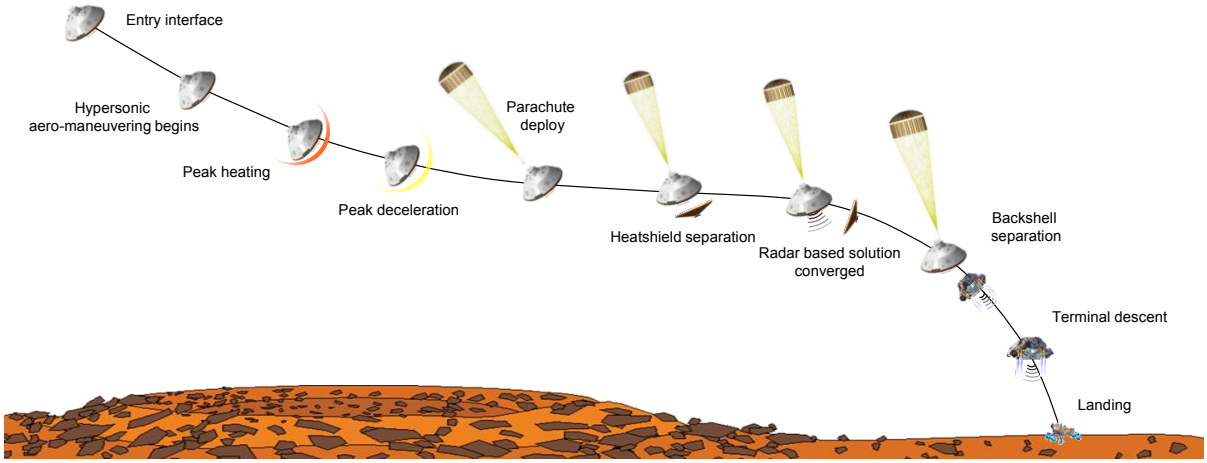

Figure 1.2. Notional entry, descent, and landing sequence.

For Mars EDL, the point of entry interface is typically defined at the time at which the vehicle is at an altitude of 125 km from the surface. The hypersonic phase of the EDL sequence is characterized by high-temperature gas dynamics, during which the vehicle undergoes peak heating and deceleration while protected by the heat shield. All Mars entry missions to date have utilized a parachute to reduce the vehicle velocity when deployed at low supersonic or transonic Mach numbers. The heat shield is discarded to enable ground acquisition with the landing radar, after which the backshell, which provides the interface between the parachute and rover or lander, separates and terminal descent operations are initiated. Methods of terminal descent and landing vary. The most recent Mars mission, MSL, used a "Skycrane" maneuver in which the rover was lowered to the surface with a tether from a hovering platform, but other solutions include crushable landing struts (Viking), descent thrusters (Viking/Mars Exploration Rover/Phoenix), and/or impact-absorbing airbags (Pathfinder/Mars Exploration Rover).

Post-flight analysis of the data collected during the EDL sequence enables post-flight reconstructions of the trajectory, aerodynamics, and atmosphere along the flight path.[7,8,9,10,11,12] The results of these reconstructions in turn present opportunities to validate pre-flight model predictions and aid in planning of future missions.

For each of the Mars missions, the reconstructions utilized both inertial navigation and statistical reconstruction techniques, the latter of which was typically comprised of variations of the Kalman

filter. Statistical techniques blend all available data and provide uncertainties, but often require assumptions regarding probability and careful "tuning" of the process noise covariance. Inertial navigation makes no such assumptions and is totally data-driven; if the IMU measurements and initial conditions were perfect, the solution obtained through inertial navigation would be the true trajectory. Of course, measurements are never perfect, and furthermore inertial navigation by itself does not provide any useful statistics. Therefore, the purpose of the present work is to present an alternative to traditional statistical reconstruction methods that is based on classical inertial navigation, takes into account observations other than those made by the IMU, and provides useful solution statistics.

Ultimately, understanding and quantifying vehicle entry dynamics in the Martian atmosphere and how they compare to expectations is critical to the success of future missions to the Red Planet and beyond. In the next section, this environment and the implications it presents with regard to navigation will be discussed.

1.1 Mars and its Atmosphere

The planet Mars, so named after the Roman god of war and colloquially referred to as the Red Planet due to its reddish appearance, has been studied for at least 3,500 years. The ancient Babylonians and Egyptians were known to have tracked the orbital characteristics as Mars is easily observable in the night sky with the naked eye, though their interests were mostly superstitious and lacked scientific reasoning. The Greeks attempted to explain Mars's apparently peculiar orbital behavior, but their elaborate solutions were ultimately flawed as they used geocentric models of the Solar System. Middle-Eastern and Eastern astronomers made some advancements while Europe underwent the so-called Dark Ages, but it was in the 16th and 17th centuries that astronomers such as Tycho Brahe, Johannes Kepler, Galileo Galilei, Giovanni Cassini, and Christiaan Huygens pioneered systematic observations of the Red Planet.[13]

Observation of the surface of Mars began in 1610, when Galileo became the first to observe Mars using a telescope. As even these early telescopes revealed global-scale features on Mars, over the next 300 years its surface was mapped by dozens of astronomers. Perhaps most notably, in 1877 the astronomer Giovanni Schiaparelli published a map of Mars, shown in Figure 1.3, on which he identified a vast network of straight, narrow features he called *canali*. This was translated to English as canals, which was mistakenly construed as being artificial in nature.[*] The revelation that there apparently existed artificial constructs on the surface of Mars spurred many dubious claims, such as those by Percival Lowell,[13] that Mars was inhabited by sentient Martians—an idea that remained popular even well after it was determined that Mars was incapable of supporting the vast water

[*] The word *canal* does not necessarily refer to an artificial construct and may be used to describe natural geographic features. The nature of this apparent misunderstanding is unclear, but it is likely that the idea of Martian canals captivated a public yearning to know more about the Cosmos.

oceans, lakes, and rivers that the 19th Century maps seemed to imply.* Despite this incident, many of the names Schiaparelli applied to various Martian features are still in use today.

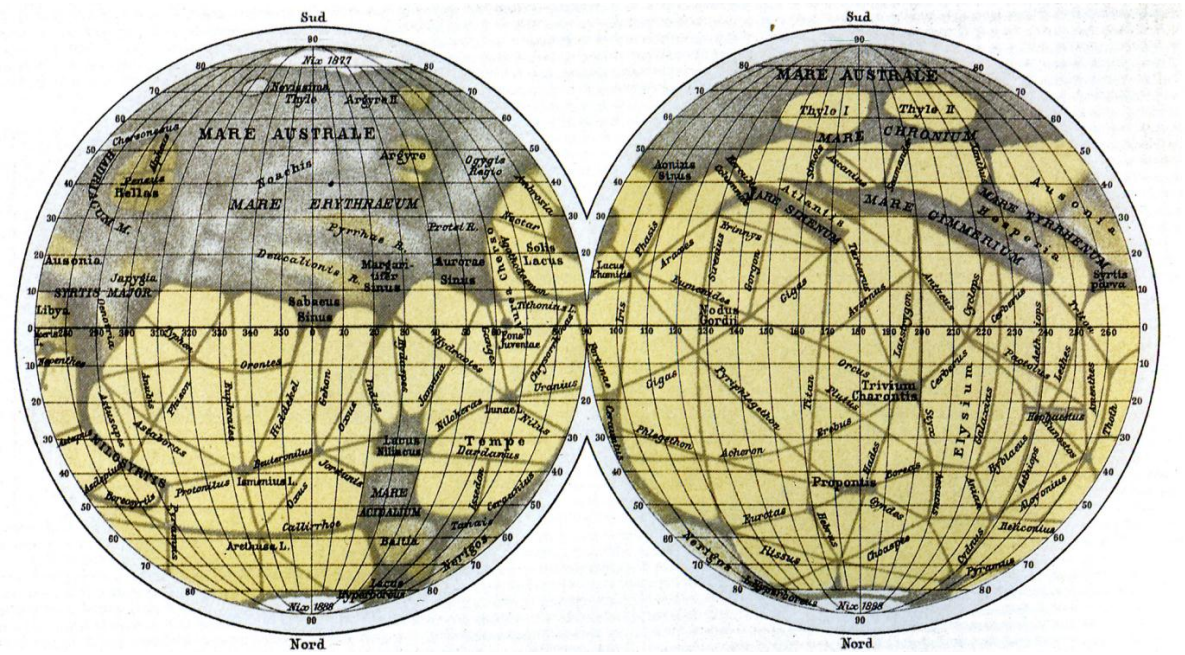

Figure 1.3. Martian "canals" as mapped by Giovanni Schiaparelli.†

Robotic observation and exploration of Mars was achieved in the second half of the 20th Century, triggered by the rapid advancement of post-World War II technology coupled with the Space Race between the United States and the Soviet Union. Early mission planning placed an emphasis on surface exploration until it was proposed that the vehicle entry phase could provide valuable information about the structure of the atmosphere.[14,15]

Photographs from the Mariner 9 spacecraft in 1971 and the later Viking orbiters provided critical information about the Mars surface and atmosphere (and finally dispelled any notions of artificial canals or structures). The photos also confirmed the presence of massive dust storms that had puzzled

* The concept of life on Mars has become thoroughly embedded in popular imagination, famously exemplified by the hostile Martians in Orson Welles' now-infamous 1938 radio adaptation of H. G. Wells' *The War of the Worlds*. Even today, the robotic exploration of Mars is in part driven by the search for evidence of past life. At the time of this writing, definitive evidence of life on Mars remains elusive, though it has been determined that Mars was in fact once covered with water oceans and rivers in its early history.

† http://planetologia.elte.hu/ipcd/ipcd.html?cim=schiaparelli1888, accessed 18 January 2013.

early Mars observers, including Schiaparelli.[16] A Mars dust storm photographed by Viking Orbiter 2 is shown in Figure 1.4.

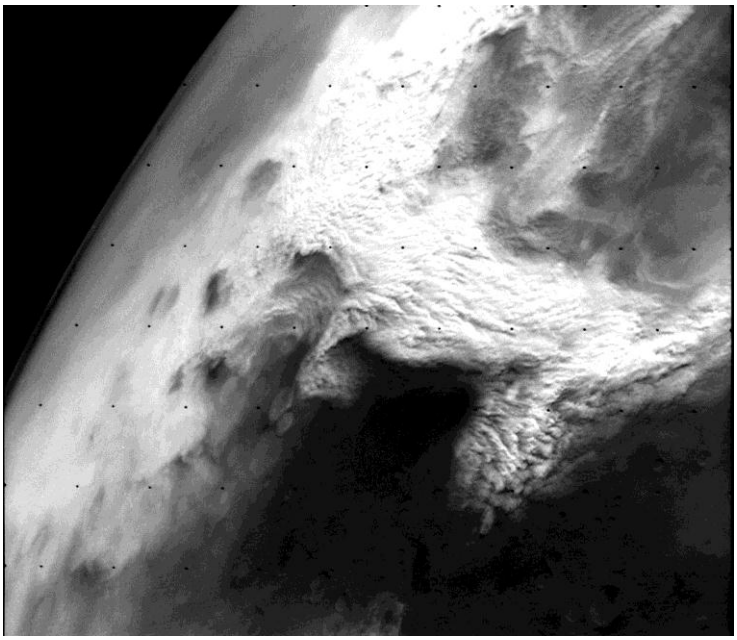

Figure 1.4. Dust storm in the Thaumasia region of Mars, photographed by Viking Orbiter 2.[*]

Some relevant physical characteristics of Mars are listed in Table 1.1. Characteristics of the Martian atmosphere are listed in Table 1.2 and the atmospheric chemical composition is listed in Table 1.3 (both of which are adapted from Ref. 17).

Table 1.1. Physical characteristics of Mars.

Parameter	Symbol	Value
Radius (km)	R	3396.19
Standard gravitational parameter (km^3/s^2)	μ	42828.376212
Second dynamic form factor (zonal harmonic)	J_2	$1.95639057765\times10^{-3}$
Rotation rate (rad/s)	Ω	7.088212079×10^{-5}

[*] http://nssdc.gsfc.nasa.gov/imgcat/html/object_page/vo2_176b02.html, accessed 13 August 2013.

Table 1.2. Characteristics of Mars atmosphere and comparison to Earth.

Parameter	Earth	Mars
Surface pressure (mb)	1014	4.0 to 8.7
Surface density (kg/m^3)	1.217	~0.020
Scale height (km)	8.5	11.1
Average temperature (K)	288	~210
Mean molecular weight (g/mol)	28.97	44.01

Table 1.3. Composition of Mars atmosphere.

Chemical species	Percentage
Carbon dioxide	95.32
Nitrogen	2.70
Argon	1.60
Oxygen	0.13
Carbon monoxide	0.08
Water, nitrogen oxide, hydrogen-deuterium-oxygen, krypton, xenon	<0.1

From a qualitative standpoint, the Martian atmosphere is quite cold and thin when compared to that of Earth. The low density in particular poses a significant challenge to landing on Mars, since there is less drag and parachutes are less effective.[6] Thus, although parachutes are used to slow the vehicle, they provide insufficient drag to soft-land a vehicle by themselves. The Mars Science Laboratory rover *Curiosity*, which is significantly more massive than previous landers and rovers, was placed at a higher altitude than previous missions by the "Skycrane" landing system that will be discussed in more detail in Chapter 2.

1.2 Fundamentals

The work presented in this dissertation explores post-flight reconstruction of spacecraft trajectory and atmosphere, specifically with regard to Mars atmospheric entry, descent, and landing (EDL) navigation. Knowledge of the vehicle dynamics and atmosphere are essential, as trajectory reconstruction involves, to varying degrees, the disciplines of aerodynamics, gas dynamics, probability, and estimation theory. A review of the fundamental topics in these disciplines in the context of navigation and reconstruction will be presented in Chapter 3.

1.2.1 Definitions

In this dissertation, the *trajectory* is the position, velocity, and orientation history of a vehicle in a specified reference frame. The *atmosphere* is the ambient density, pressure, and temperature along the vehicle flight path as a function of altitude. The *aerodynamics* of the vehicle are the forces, moments,

and other parameters that are induced by the dynamic interactions with the flow field during flight. Generally, trajectory and atmospheric parameters are derived from flight data measured *in situ* during entry. The *state* formally refers to the set of parameters that define the position and velocity of the vehicle, but in the present work it will be used to include the attitude. It may also refer to other groups of parameters, such as the atmospheric state or the aerodynamic state. *Redundant data* are any observations other than those required for inertial navigation.

There are four types of quantities that will be frequently used throughout this work. *True quantities*, represented by the unembellished symbol x, are the actual and unknowable values of the parameter being estimated. *Measurements* or *observations*, represented by $\tilde{x}$, are quantities returned by sensors and instrumentation. *Estimates*, represented by $\hat{x}$, are quantities returned by statistical algorithms designed to give a "best guess" of the true values x by using the measurements $\tilde{x}$. *Modeled quantities*, represented by $\overline{x}$, are produced by mathematical representations of a system that simulate the relevant physical processes.

1.2.2 Error and Uncertainty

In recent years, there has been an effort to take a more formal approach to quantifying the accuracy of the quantities in question, particularly in the field of computational fluid dynamics.[18] *Errors* are differences between the true or expected values and the observations or estimates. *Uncertainties* describe the confidence in the precision and accuracy of the observation or estimate in a statistical sense by characterizing the contributions of the different error sources, and are sometimes informally described as estimates of the errors. In the field of metrology, the uncertainty corresponds to the range or spread of observed values for a measured parameter. In the field of statistics, the uncertainty may be obtained from the covariance in an estimator or from the dispersions in a Monte Carlo analysis. In each case, the uncertainty is closely related to the *standard deviation*, which describes how much a parameter varies from its true or expected value. These particular definitions are widely used in metrology and statistics; more formal definitions are used in model verification and validation and are provided in Ref. 19.*

Errors may be categorized as random or systematic. *Random* errors vary from measurement to measurement and are due to lack of precision or instrument noise. For example, repeatedly measuring the height of a coffee table with a meter stick might result in values that range between 0.96 and 0.98 m with a mean value of 0.97 m; thus, the table may be said to have a height of 0.97±0.01 m. The ±0.01 m term is the uncertainty due to random errors. *Systematic* errors are consistent between measurements and may be due to poor calibration, lack of knowledge of the relevant physics, poor assumptions or models, etc., and are more difficult to quantify. For example, the aforementioned

* A measurement or estimate is essentially meaningless without an accompanying uncertainty. For example, an accelerometer reading of 10 m/s^2 may be (perhaps incorrectly) construed to be useful until the uncertainty in that measurement is determined to be ±50 m/s^2. Ideally, the errors lie within the range of uncertainty.

meter stick may actually have been 2 cm short of a meter; thus, the measurements were systematically biased by 2 cm. If the true and unknowable height is 0.99 m, then the solution lies outside of the uncertainty—a situation that may be rectified only by using a more accurate meter stick or improving the knowledge of the length of the current meter stick. In practice, *a priori* estimates of instrumentation errors are typically provided by the manufacturer. These errors may later be estimated in a statistical process and compared to the *a priori* value.

In summary, one of the fundamental challenges of reconstruction—and indeed, of any field involving data analysis—is obtaining accurate estimates of the unknowable true values using erroneous observations and imperfect models.

1.2.3 Notation

In this dissertation, vectors are series of elements arranged in a column or row and are represented by boldfaced uppercase or lowercase Roman or Greek letters. Scalar quantities or vector components are represented by italicized, lightface letters. Boldface is used exclusively for vectors and quaternions. Notation is illustrated with the arbitrary vector **v** (column vectors are typically used so that the quantity $\mathbf{v}^{\mathrm{T}}\mathbf{v}$ is a scalar):

$\mathbf{v}$	vector
$\hat{\mathbf{v}}$	unit vector
$\lvert\mathbf{v}\rvert$ or v	Euclidian norm of vector, i.e. $\sqrt{\mathbf{v}^{\mathrm{T}}\mathbf{v}}$
v_i	*i*th component of vector

Components of a vector are the projections of the vector onto the coordinate system axes, and are typically identified with numeric subscripts such that $\mathbf{v}=[v_1,v_2,...,v_n]^{\mathrm{T}}$. For the special case of a three-dimensional Cartesian vector, an ordered triplet may be used, i.e., $\mathbf{v}=[v_x,v_y,v_z]^{\mathrm{T}}$ or $\mathbf{v}=v_x\hat{\mathbf{i}}+v_y\hat{\mathbf{j}}+v_z\hat{\mathbf{k}}$, where $\hat{\mathbf{i}}$, $\hat{\mathbf{j}}$, and $\hat{\mathbf{k}}$ are unit vectors that identify the orthogonal axes of the coordinate system such that $\hat{\mathbf{i}}=[1,0,0]^{\mathrm{T}}$, $\hat{\mathbf{j}}=[0,1,0]^{\mathrm{T}}$, and $\hat{\mathbf{k}}=[0,0,1]^{\mathrm{T}}$. In general, the symbols *x*, *y*, and *z* are reserved for identifying components of a three-dimensional Cartesian vector (when used as subscripts) or axes of a Cartesian coordinate system (when used as normal scripts) in three-dimensional Euclidian space.

Matrices are rectangular arrays of elements and are represented by non-emphasized uppercase Roman or Greek letters. Notation is illustrated with the arbitrary matrix M:

M	matrix
M^{-1}	matrix inverse
M^{T}	matrix transpose
M_{ij}	component of matrix in the *i*th row and *j*th column
$\det(\mathrm{M})$	determinant of matrix
$\mathrm{diag}(\mathrm{M})$	diagonal of matrix

Vectors and scalars may be considered special cases of the matrix. For example, a matrix with dimensions $m \times n$ is a vector if $m = 1$ or $n = 1$. Similarly, a scalar is a matrix with dimensions $m = n = 1$. A matrix with more than two dimensions is referred to as an array.

Although every effort has been made to maintain consistency in notation and terminology in this work, exceptions will be widespread due to historical convention and practicality. The observant reader will have already noticed an abuse of notation: an estimate is signified by a letter embellished with a carat, which also signifies a unit vector. In general, the context will resolve ambiguities.

This dissertation will use the International System of Units (SI). In this system, the base units of length, mass, time, and temperature are the meter (m), kilogram (kg), second (s), and kelvin (K), respectively. The derived units of force, pressure, and energy are the newton (N), pascal (Pa), and joule (J), respectively.

1.3 Previous Work and Principal Issues

Historically, there have been two common trajectory reconstruction techniques. Probabilistic or statistical approaches process measurements in a stochastic algorithm that minimizes a payoff function defined by system models. Examples of these methods include weighted least squares, minimum variance, extended and unscented Kalman filters, etc.[20,21,22] Statistical methods may utilize *a priori* information and blend various types of observations to reduce solution uncertainties, which are readily available from estimator covariances. These techniques, however, often require assumptions of probability distribution functions and use of dynamical models, such as for aerodynamics, data and state noise, observation equations, etc. Furthermore, statistical filters often require "tuning" of the process noise or *a priori* covariance to ensure convergence.[20] Despite these apparent issues, statistical techniques have been used extensively and successfully for decades. In particular, the Kalman filter has been used in a wide variety of applications since its development in the early 1960s, from GPS-based automobile navigation to satellite tracking.

The other common trajectory reconstruction technique is inertial navigation, a deterministic method in which the vehicle position and velocity are propagated using acceleration and angular velocity measurements from an IMU.[4] This method has been used on every* NASA Mars mission and has proven to be a relatively straightforward and fast trajectory reconstruction technique.[7-12] It is identical to the algorithm used aboard spacecraft to determine position and velocity during entry for navigation purposes.† Inertial navigation does not require the use of models to relate the observations to the vehicle dynamics (with the exception of gravity models, which are often well-known), and does

---

* Mars Pathfinder (1997) carried a single gyroscope for spin stabilization about the principal axes, so the attitude could not be propagated using angular rate measurements as in classical inertial navigation.

† The term "inertial navigation" formally refers to the navigation technique used by vehicles equipped with an IMU to determine position and velocity during flight. The same algorithm, however, is used post-flight for reconstruction purposes, and therefore in the present work "inertial navigation" may refer to either the navigation or reconstruction technique.

not rely on pre-flight simulations or computational fluid dynamics (CFD). However, as it is a deterministic method, inertial navigation lacks the advantages of statistical techniques, namely that in its classical form it cannot incorporate redundant data (pressure, altimetry, etc.), and solution statistics are unavailable. This dissertation focuses on addressing these limitations.

1.3.1 Inertial Navigation and Atmosphere Reconstruction with Statistics

A technique has recently been developed that uses the inertial navigation approach to trajectory reconstruction in a Monte Carlo dispersion process to take advantage of available redundant observations (that is, any observations other than body accelerations and angular velocities) and obtain parameter uncertainties. This process, called Inertial Navigation Statistical Trajectory and Atmosphere Reconstruction (INSTAR), utilizes the inertial navigation algorithm to reconstruct the trajectory and a classical approach to reconstruct the atmosphere. Statistics are introduced by using Monte Carlo dispersion techniques that are often used in pre-flight design and development of EDL missions. Thus, the INSTAR method enables the inclusion of redundant data types as well as a statistical approach to estimating parameter uncertainties, but still uses the framework of inertial navigation. INSTAR also does not require any linearization and is therefore well-suited to nonlinear problem. A particular advantage of this approach is that it permits specification and estimation of arbitrary probability distributions throughout the process, which enables analysis of parameter solutions in probability space.

In the trajectory reconstruction component of the INSTAR process, illustrated in the Venn diagram in Figure 1.5, the initial state conditions and IMU error parameters are dispersed in a Monte Carlo sense using specified uncertainties. From these dispersed initial conditions, the observed IMU accelerations and angular rates are integrated using inertial navigation to obtain a set of dispersed reconstructed trajectories. Though not shown here, dispersed atmosphere profiles may be obtained from the trajectory and an initial atmospheric state using a classical atmosphere reconstruction technique. Redundant data not normally used in inertial navigation such as landing site location, altimetry, air data system observations, etc. are then used to constrain the dispersed trajectories in the "measurement space" to the subset that satisfies those observations. Trajectory and atmosphere probability density functions and parameter uncertainties in the form of standard deviations may then be obtained from this subset of constrained trajectories and atmospheres.

The fundamental concept of INSTAR, namely using redundant data to update parameter uncertainties in a Monte Carlo process, was introduced by Blanchard and Tolson and demonstrated by Huh using flight data from the X-43A Hyper-X research vehicle, using GPS tracking data as the redundant observations.[23] The primary interest in that analysis was reconstruction of the aerodynamic forces and moments and how the corresponding uncertainties compared to uncertainties in pre-flight CFD aerodynamic databases. Reconstruction and analysis of the atmosphere and related parameters was not included, which is of greater significance in EDL.

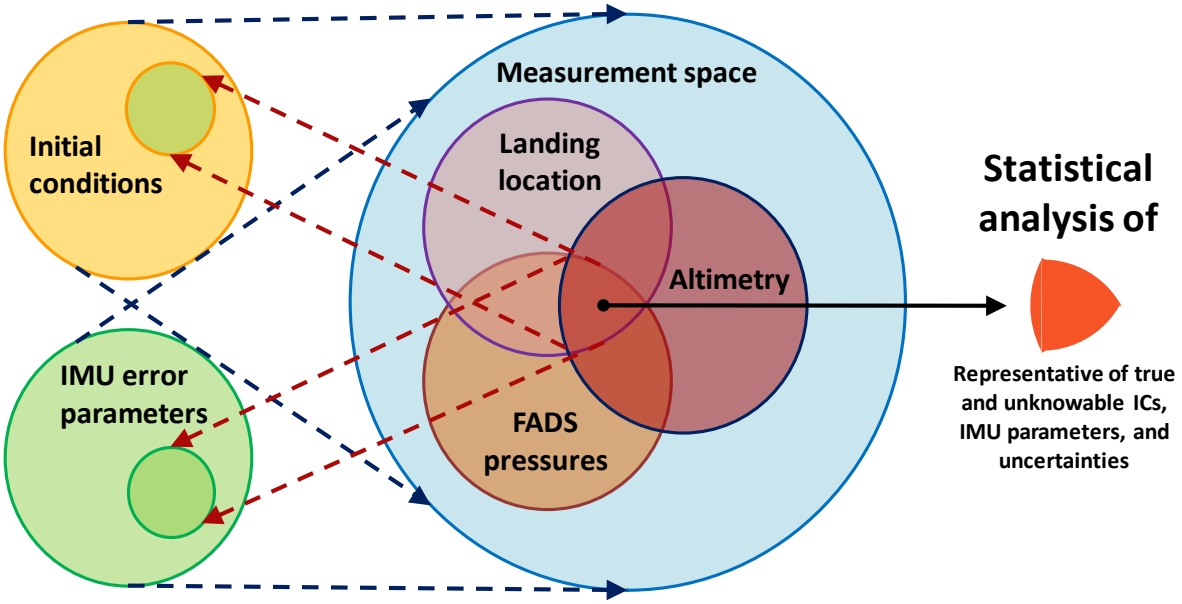

Figure 1.5. INSTAR trajectory reconstruction process.

The process was also demonstrated by Blanchard *et al.* using flight data from Mars Science Laboratory EDL sequence and using the landing site as the redundant observation.[24] It was determined that simply using the landing site significantly constrained the range of possible trajectories, thus reducing the uncertainty in the initial state conditions. In this application, however, reconstruction of the atmosphere was also excluded. A revised approach to including landing site, with atmosphere reconstruction, will be presented in Chapter 4.

1.3.2 Flush Air Data Systems

A flush air data system (FADS) provides pressure measurements along the surface of a vehicle using pressure transducers. FADS pressure data may be used in conjunction with CFD, wind tunnel data, and/or Newtonian flow approximations to estimate aerodynamic parameters and associated uncertainties. The original FADS-based parameter estimation algorithm based on least squares was developed for the Shuttle Entry Air Data System (SEADS),[25,26] and was later applied to other vehicles such as the X-43 Hyper-X.[27] FADS instrumentation was also used in free-flight aeroballistic experiments of scale models of the Crew Exploration Vehicle (CEV) in 2008 and 2009, as well as scale models of Mars Science Laboratory in 2012.[28,29,30] These experiments were conducted at Aberdeen Proving Grounds in Maryland as a joint effort between NASA Langley Research Center (LaRC) and the US Army Research Laboratory (ARL). In each of these free-flight tests, the estimation techniques described in Ref. 30 were used to estimate the aerodynamic parameters and

associated uncertainties from the FADS pressure data. Most recently, a flush air data system was flown on Mars Science Laboratory in the form of the Mars Entry Atmospheric Data System (MEADS). A variation of the original formulation was applied to pressure data from this mission.[31,32]

A complete description of the FADS-based statistical estimation method with results using MSL MEADS pressures will be discussed in §4.3. This algorithm will be used extensively to address how pressures from a flush air data system may be considered within the INSTAR framework, and how the inclusion of these data validate or improve estimates and uncertainties beyond statistical approaches.

1.3.3 Uncertainties in Computational Fluid Dynamics

Computational fluid dynamics (CFD) plays a significant role in mission planning and atmosphere reconstruction. Typically, CFD provides tables of aerodynamic coefficients and surface pressures. Experimental wind tunnel data may be used to validate and augment the CFD results. Because CFD models are not perfectly representative of the flow field, various trajectory parameters are dispersed in a Monte Carlo sense and dispersed CFD solutions are obtained. Uncertainties from these dispersions are then said to be representative of the accuracy of the CFD model. In general, CFD data uncertainty is difficult to quantify and until recently, uncertainties were sometimes not even available.[18] Furthermore, CFD solutions are typically run in a grid (i.e., pressures are given at designated Mach numbers, angles of attack, and port location on the heat shield). Different grids are used to study effect of node spacing, geometry, etc. until the solution is determined to be insensitive to the grid. However, between any two grid points, data must be interpolated, leading to more errors and uncertainty. This dissertation will address how the effects of uncertainties and correlations in CFD data may be characterized and quantified within the INSTAR framework.

FADS-based reconstruction methods rely on CFD model pressures, and therefore model pressure errors are tied to the solution errors. Furthermore, CFD errors affect density estimates, as the axial force coefficient needed to compute density is obtained from CFD. This dissertation will address how FADS-derived density and axial force coefficient estimates may be reconciled with IMU- and CFD-derived density and axial force coefficient estimates.

1.3.4 Summary of Principal Issues

The principal issues that will be addressed in this dissertation may be summarized as follows:

1. How INSTAR solutions may be interpreted in a probabilistic sense,
2. How the effects of uncertainties and correlations in CFD tables may be characterized and quantified within the INSTAR framework,
3. How FADS pressures may be considered using INSTAR, and how the inclusion of these data validate or improve estimates and uncertainties beyond traditional statistical approaches, and

4. How FADS-derived density and axial force coefficient estimates may be reconciled with IMU- and CFD-derived density and axial force coefficient estimates.

1.4 Contributions

The objectives of this dissertation are to formally develop an alternative to traditional statistical approaches to EDL reconstruction, to implement it using flight data with multiple sources of redundant observations, and to compare the resultant estimates and uncertainties to those from corresponding Kalman filter solutions. Pursuant to these objectives, the recently-developed reconstruction scheme based on inertial navigation, called INSTAR, is extended to include atmosphere reconstruction by utilizing the classical approach to obtaining freestream density, pressure, and temperature. INSTAR provides statistical uncertainties by utilizing Monte Carlo dispersion techniques.

A method is introduced to consider FADS pressures in the INSTAR approach by first assuming that the trajectory estimates and uncertainties cannot be appreciably improved using FADS after introducing landing site as a redundant observation. This trajectory solution is then used in a minimum variance algorithm in conjunction with Monte Carlo dispersions to obtain aerodynamic estimates and uncertainties from FADS observations. Atmospheric parameters and uncertainties are then derived from the FADS minimum variance solutions and compared to those derived from INSTAR. A method to interpret INSTAR trajectory solutions in a probabilistic sense is also presented.

This dissertation also introduces a method to consider correlated CFD uncertainties in INSTAR. Using *a priori* CFD uncertainties, CFD force and pressure coefficients are dispersed in a Monte Carlo sense and carried over into the reconstructions. An analysis of the subsequent effects on the trajectory, atmosphere, and aerodynamic estimates and statistics is presented.

These techniques are implemented in INSTAR and demonstrated using flight data from the Mars Science Laboratory entry vehicle, which contained an IMU and a flush air data system called MEADS. A complete set of trajectory, aerodynamic, and atmospheric parameter estimates and uncertainties are presented, along with comparisons to statistical Kalman filter solutions.

1.5 Overview

A roadmap for this dissertation is shown in Figure 1.6. All of the topics fall under the broad subject of planetary entry, descent, and landing navigation. The numbered circles indicate chapter numbers.

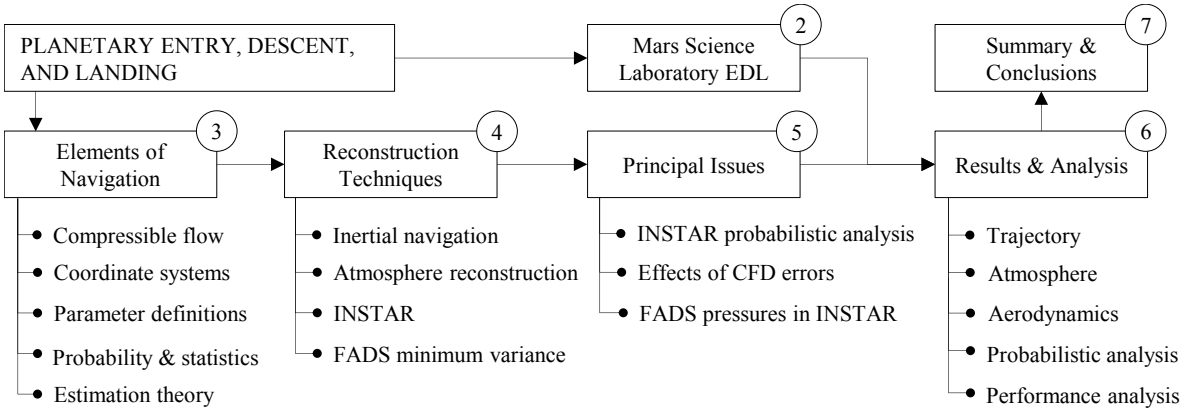

Figure 1.6. Dissertation roadmap.

An overview of the Mars Science Laboratory mission, hardware, and data in the context of trajectory reconstruction is provided in Chapter 2. The elements and definitions that form the basis of the more advanced methods of navigation and reconstruction are then established in Chapter 3. The reconstruction methodologies used in this dissertation are reviewed in detail in Chapter 4. The development and validation of the techniques used to address the principal issues that are the main subject of the dissertation are presented in Chapter 5. The results of applying these techniques to the MSL EDL data are presented and discussed in Chapter 6. Finally, the conclusions drawn from the results, a summary of the dissertation, and topics and applications that may be explored in future investigations are presented in Chapter 7.

Chapter 2: Mars Science Laboratory

Mars Science Laboratory is a Flagship NASA mission that landed in Gale Crater on 6 August 2012, and is currently the largest and most sophisticated vehicle ever sent to Mars.[33] It presents an opportunity to apply the methods and techniques developed in this dissertation to an actual Mars flight. A review of the MSL mission, EDL sequence, and data is provided in this chapter.

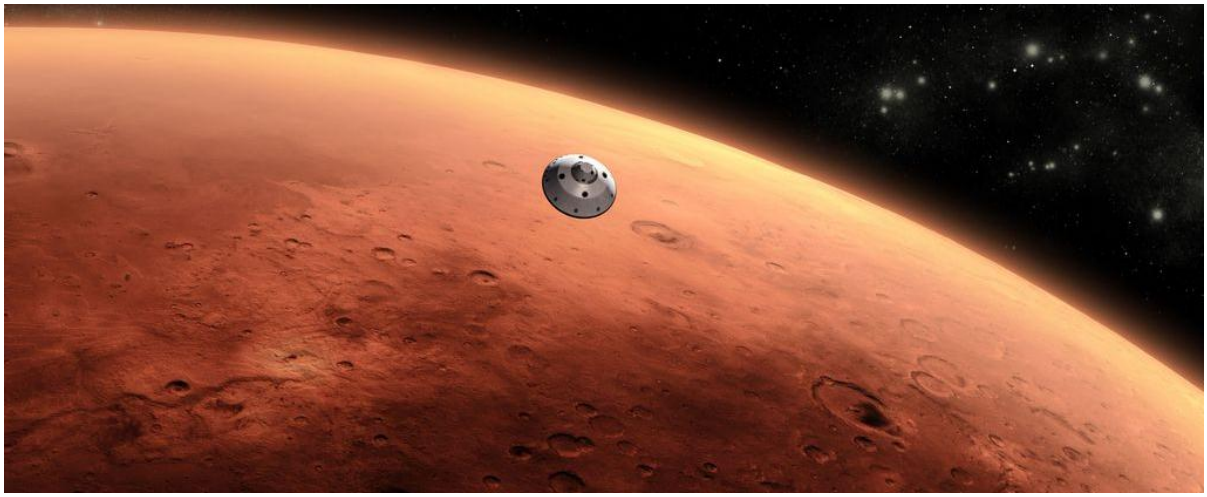

Figure 2.1. Artist's rendering of MSL on approach to Mars.*

* http://mars.jpl.nasa.gov/msl/multimedia/images/?ImageID=3644, accessed 11 November 2013.

Table 2.1 lists some relevant information regarding MSL and comparisons to previous NASA Mars missions. Notably, MSL was heavier, larger, has a higher ballistic coefficient and lift-to-drag ratio, and currently has been the only actively guided entry vehicle to successfully place a surface asset on Mars. The difficulty of placing such a high useful landed mass at such a high altitude in a low-density atmosphere dictated many mission requirements and necessitated the use of the Skycrane maneuver that will be described later in this chapter.

Table 2.1. Comparison of Mars Missions (adapted from Ref. 6).

Landing Year	1976	1997	2004	2008	2012
Mission	Viking 1 & 2	Pathfinder	MER A & B	Phoenix	MSL
Entry velocity (km/s)	4.7	7.26	5.4	5.59	5.8
Ballistic coefficient (kg/m^2)	63.7	62.3	89.8	65	135
Entry mass (kg)	930	585	840	602	3152
Heat shield diameter (m)	3.505	2.65	2.65	2.65	4.518
Hypersonic trim total angle of attack	11.2°	0°	0°	0°	16°
Hypersonic L/D	0.18	0	0	0	0.24
Attitude control	3-axis RCS unguided	2 RPM passive	2 RPM passive	Uncontrolled	3-axis RCS guided
Lift control	CM offset	Non-lifting	Non-lifting	Non-lifting	CM offset
Peak heating rate (W/cm^2)	26	100	44	47	<210
Useful landed mass (kg)	244	92	173	167	800
3σ land. ellipse major axis (km)	280	200	80	100	20
3σ land. ellipse minor axis (km)	100	100	12	21	20
Landing site elevation (km from MOLA)	-3.5	-2.5	-1.9	-4.0	2.0

The MSL flight data have been the subject of intensive post-flight analysis, and various trajectory, aerodynamic, and atmospheric reconstructions using both statistical and deterministic techniques have been carried out.[24,32] A comprehensive and rigorous statistical solution using an iterative extended Kalman filter that blends information from all available data sources, including initial conditions, inertial measurement unit data, FADS pressures, altimetry, and landing site location has also been presented.[34,35] A thorough analysis and discussion by the same reconstruction group of the MSL EDL aerodynamics is provided in Ref. 36.

2.1 Entry, Descent, and Landing Sequence

MSL was launched from Cape Canaveral SLC-41 on an Atlas V 541 on November 26th, 2011, and arrived at Mars and began its entry sequence on August 6th, 2012. Table 2.2 lists the relevant events in the EDL timeline, referenced from t_0. The reference time t_0 is defined to be 9 min (540 s)

prior to entry interface and corresponds to a spacecraft clock time of 397501174.937729 s and a Julian Date of 2456145.71033450.

Table 2.2. MSL event timeline referenced from t_0.

Event	Time (s)
Entry interface	540.00
Guidance start	585.88
Bank reversal 1	612.88
Peak deceleration	620.33
Bank reversal 2	633.88
Bank reversal 3	663.38
Heading alignment	675.63
Entry ballast mass jettison	779.87
Parachute deployment	799.12
Final MEADS measurement	808.86
Heat shield separation	818.87
Radar lock	837.12
Backshell separation	915.92
Powered descent	918.38
Skycrane start	952.89
Touchdown sensed	971.52
Fly away	972.31

Figure 2.2 shows the MSL entry, descent, and landing profile with information obtained post-flight. During interplanetary cruise, the spacecraft was spin-stabilized at 2 rpm with no center of mass offset. Separation of the entry vehicle from the cruise stage occurred at EI-10 min. After a de-spin maneuver, two tungsten balance masses were jettisoned to produce a center of mass offset and enable a lifting trajectory with a hypersonic trim total angle of attack of approximately 16°. Three bank reversal maneuvers were executed during the hypersonic phase to provide range control. After the final heading alignment, six additional tungsten balance masses were jettisoned to remove the center of mass offset and bring the trim angle of attack back to zero. Deployment of the parachute occurred at approximately Mach 1.8, followed by heat shield separation at approximately 19 s later. After 97 s of parachute descent, the decent stage separated from the backshell and the Mars Landing Engines (MLEs) fired at an altitude of 250 m to bring the horizontal velocity to 0 m/s. The Skycrane maneuver was initiated and lowered the rover until touchdown occurred 431 s after EI and approximately 972 s after t_0. Immediately after touchdown, the tether was disconnected from the rover and the navigation computer commanded the decent stage to execute the “flyaway” maneuver, firing the MLEs to bring the descent stage a safe distance from the rover before impacting the surface.

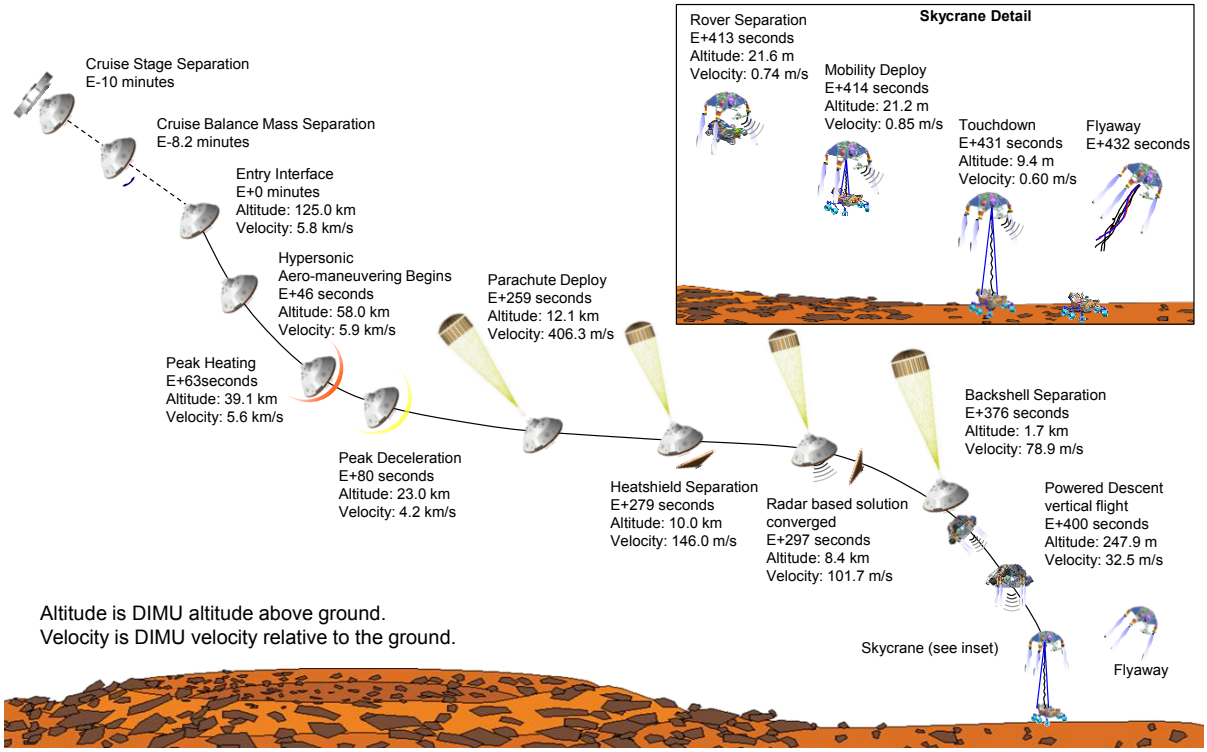

Figure 2.2. MSL entry, descent, and landing profile.[*]

Of particular interest in Figure 2.2 are the regions of the trajectory where observations were made by the various onboard sensors. Radar data were collected 18 seconds after heat shield separation to touchdown. Flush air data system pressure observations are not shown, but useful measurements were made from approximately peak heating to one minute prior to parachute deploy (these limits were defined by the 850 Pa dynamic pressure threshold specified by science objectives, though pressure observations continued to be made until ten seconds prior to heat shield jettison). Location of the landing site was obtained post-flight using photography by existing orbital assets. Finally, throughout the entire EDL sequence the IMU collected continuous body acceleration and angular velocity measurements, which are the main data types used in inertial navigation.

Figure 2.3 is an image taken by MRO that shows the relative locations of the various EDL system elements on the surface of Mars, including the backshell and parachute, descent stage, heat shield, and *Curiosity* rover.

[*] Jet Propulsion Laboratory/CalTech.

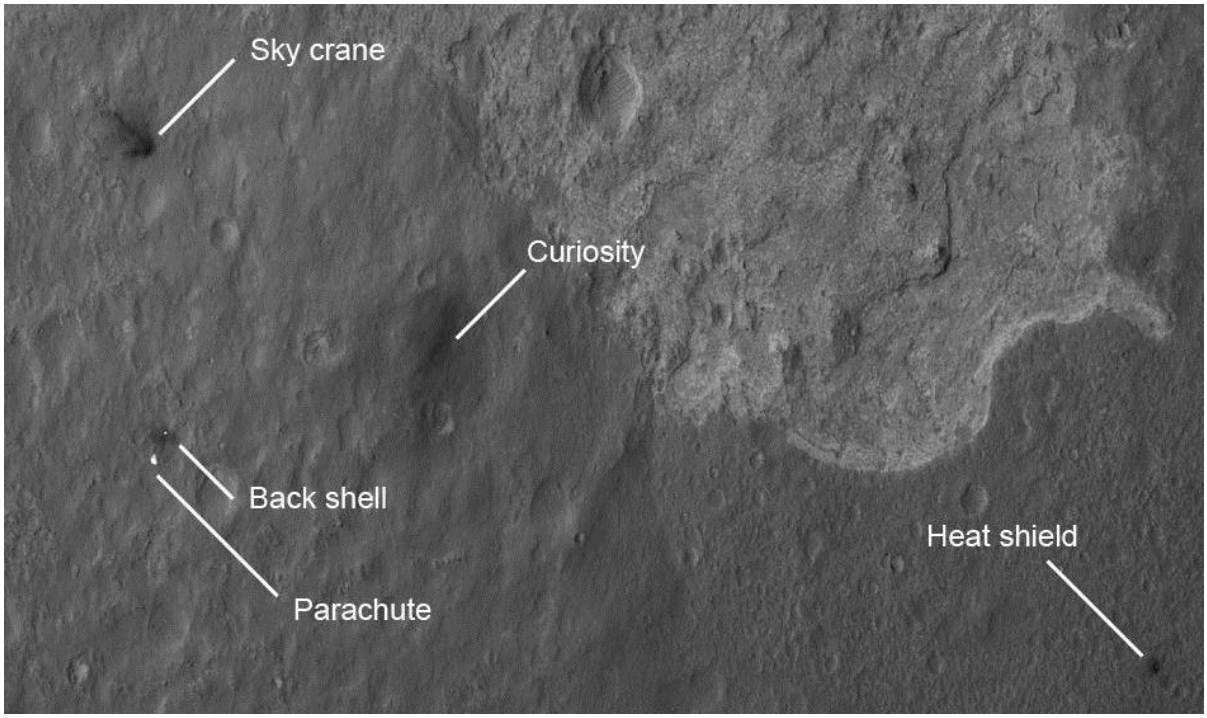

Figure 2.3. Relative locations of entry system components at Gale crater, photographed by MRO. Curiosity is 1500 m from the heat shield, 615 m from the backshell, and 650 m from the Skycrane (descent stage).[*]

2.2 Overview of Flight Systems, Hardware, and Operations

The Mars Science Laboratory cruise and entry vehicle consisted of five major components, shown in Figure 2.4. The cruise stage performed trajectory corrections and provided thermal control to the spacecraft during interplanetary cruise. Just prior to entry and cruise stage separation, it aligned the vehicle orientation for the EDL sequence. The backshell contained the interface to the cruise stage and parachute. The descent stage carried the entry vehicle IMUs, guidance and navigation computer, umbilicals and tethering systems to hold the rover, and engines for the terminal descent and landing phase of the entry. The rover, named *Curiosity*, was carried by the descent stage and lowered to the surface using the Skycrane maneuver. The heat shield protected the vehicle from the extreme thermal environment during the entry phase. The entry vehicle with some dimensions labeled is shown in Figure 2.5.

[*] http://mars.jpl.nasa.gov/msl/multimedia/images/?ImageID=4299, accessed 21 May 2013.

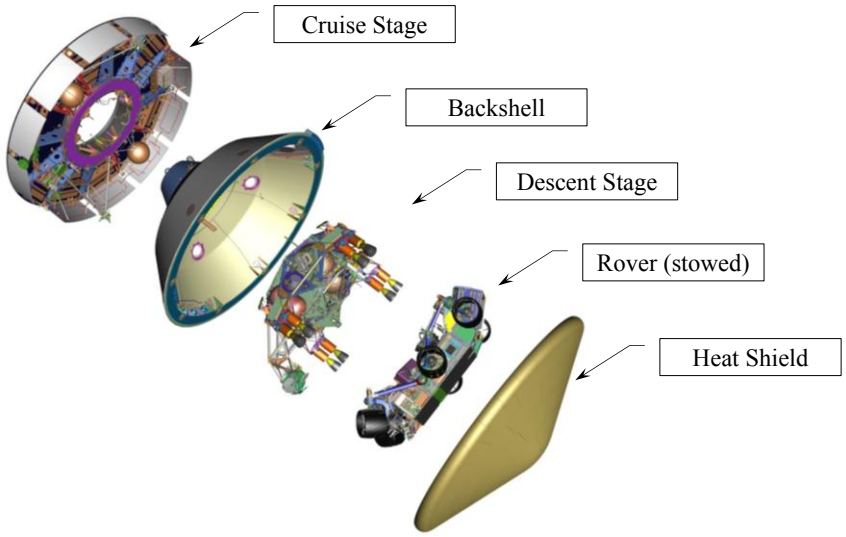

Figure 2.4. Major components of Mars Science Laboratory.[*]

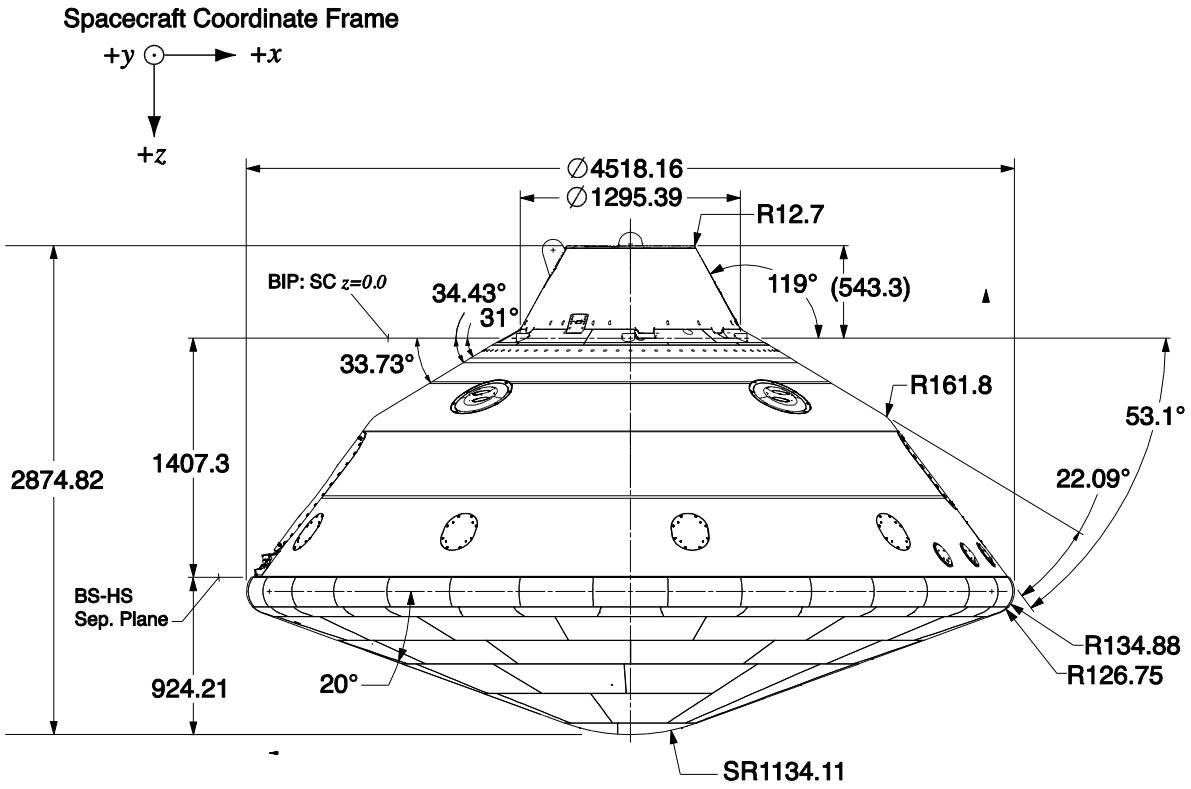

Figure 2.5. Simplified dimensions of MSL entry vehicle (all units in millimeters or degrees).[*]

[*] Jet Propulsion Laboratory/CalTech.

2.2.1 Coordinate Systems

Mars Science Laboratory utilized several coordinate systems fixed to the various components of the spacecraft. Thorough descriptions of coordinate system nomenclature and other frames related to trajectory reconstruction will be discussed in §3.2. Figure 2.6 illustrates the relationship between the cruse stage frame (CS), spacecraft frame (SC), descent stage frame (DS), and rover frame (R). As indicated, the SC and CS frames are coincident.

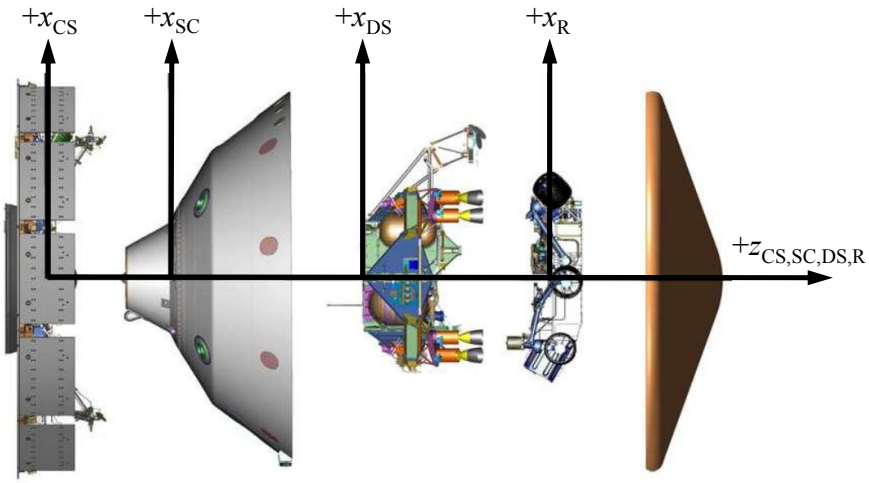

Figure 2.6. Comparison of Mars Science Laboratory coordinate systems.[37] Note that the spacecraft (SC) and cruise stage (CS) frames are coincident.

The origin of the spacecraft frame is the center of the circle defined by three specific separation bolts on the surface of the backshell.[37] The $+z_{SC}$ axis is pointed towards the nose of the heat shield, the $+x_{SC}$ axis is pointed towards the forward direction of the rover, and the $+y_{SC}$ axis completes the right-hand orthogonal frame.

The cruise stage frame, the descent stage frame, and rover frame shown in Figure 2.6 are all defined relative to the spacecraft frame. The orientations of these frames are identical to the spacecraft frame. The center of the cruise stage frame is coincident with the spacecraft frame, the center of the descent stage frame is translated 100 mm down the $+z_{SC}$ axis from the origin of the spacecraft frame, and the center of the rover frame is translated 1300 mm down the $+z_{SC}$ axis from the origin of the spacecraft frame.[37]

The descent IMU (DIMU) frame is the frame in which data from the inertial measurement unit is provided. The description here is that of DIMU-A, the relevance of which will be described in the

next section. The origin of the descent IMU frame is described by a position vector in the descent stage frame:

$$\mathbf{r}^{\mathrm{DIMU/DS}} = \begin{bmatrix} 868.7235 & -640.7420 & 508.0068 \end{bmatrix}^{\mathrm{T}} \text{ mm} \tag{2.1}$$

The $+x_{\mathrm{DIMU}}$ axis is parallel to the descent stage x-y plane, perpendicular to the installation plane, positive into the installation frame, and rotated +207.209° from the $+x_{\mathrm{SC}}$ axis about the $+z_{\mathrm{SC}}$ axis. The $+y_{\mathrm{DIMU}}$ axis is parallel installation plane and one of the reference mirrors and rotated +45° about the $+x_{\mathrm{DIMU}}$ axis to form a 135° angle from the $+z_{\mathrm{SC}}$ axis. The $+z_{\mathrm{DIMU}}$ axis is parallel installation plane and one of the reference mirrors and rotated -45° about the $+x_{\mathrm{DIMU}}$ axis to form a 45° angle from the $+z_{\mathrm{SC}}$ axis. This orientation is shown in Figure 2.7.[37]

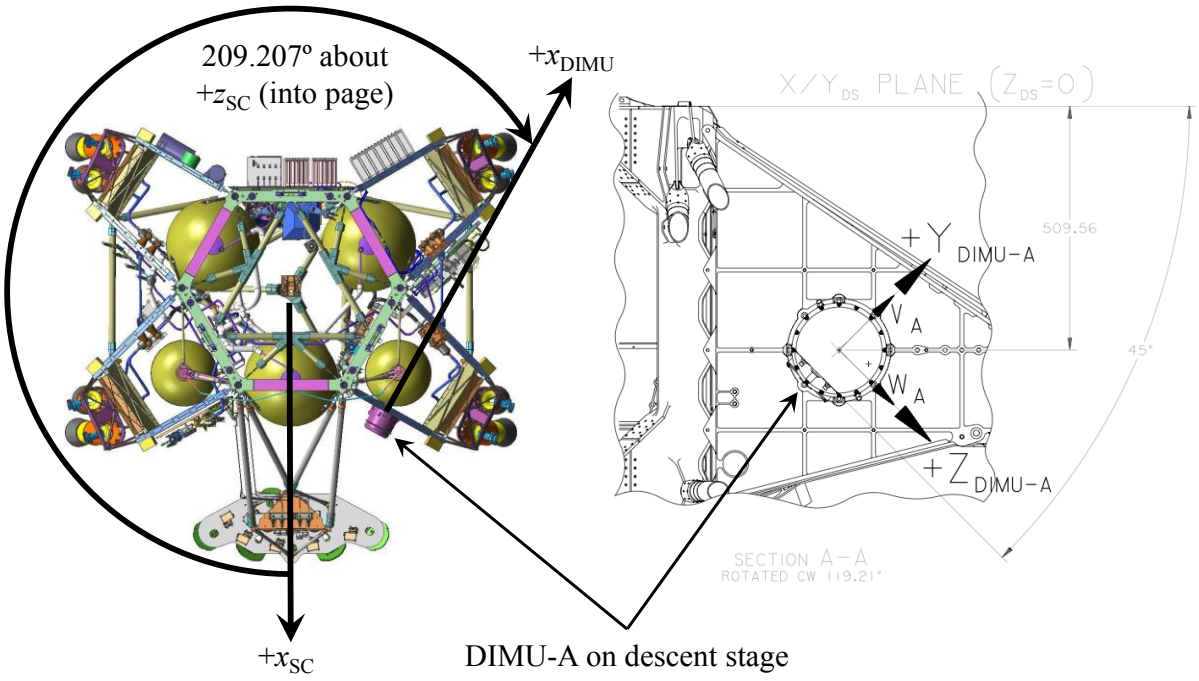

Figure 2.7. MSL DIMU frame orientation relative to descent stage frame.[37]

The as-measured quaternion that describes the rotation from the descent IMU frame to the descent stage frame is[37]

$$\boldsymbol{q}^{\mathrm{DIMU/DS}} = \begin{bmatrix} 0.09656567168731096 \\ -0.3700392720635329 \\ 0.8940638772203431 \\ 0.2332290540048484 \end{bmatrix} \tag{2.2}$$

where the fourth component is the scalar term.

2.2.2 Navigation Sensors

The entry vehicle was equipped with two Honeywell miniature inertial measurement units (MIMUs), also referred to as descent IMUs A and B (DIMU-A and DIMU-B). Only DIMU-A was active during entry due to bandwidth restrictions; for the remainder of this work, the term "IMU" in the context of MSL will refer specifically to this unit.[38] The strap-down* IMUs carried solid-state micro electro-mechanical system (MEMS) accelerometers and solid-state fiber optic gyroscopes to measure vehicle accelerations and angular rates, respectively. The onboard navigation computer used these IMU measurements and inertial navigation to determine the vehicle position, velocity, and orientation and to manage vehicle guidance and control. The DIMU-A unit mounted to the descent stage structure is shown in Figure 2.8.

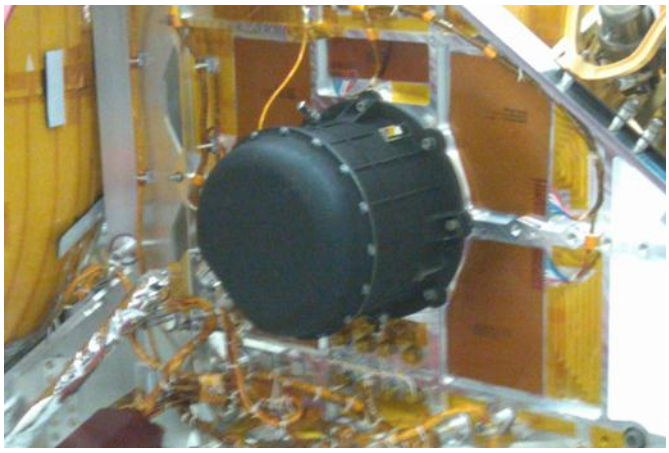

Figure 2.8. MSL descent IMU (DIMU-A).[37]

* A strap-down IMU is one that is attached to the rigid body, as opposed to one on a stabilized gimbaled platform.

The IMU error models are

$$\tilde{\mathbf{a}} = \begin{bmatrix} \tilde{a}_x \\ \tilde{a}_y \\ \tilde{a}_z \end{bmatrix} = \begin{bmatrix} SF_{a,x} & -\phi_z & \phi_y \\ \phi_z & SF_{a,y} & -\phi_x \\ -\phi_y & \phi_x & SF_{a,z} \end{bmatrix} \left(\begin{bmatrix} a_x \\ a_y \\ a_z \end{bmatrix} + \begin{bmatrix} B_{a,x} \\ B_{a,y} \\ B_{a,z} \end{bmatrix} \right) \tag{2.3}$$

$$\tilde{\boldsymbol{\omega}} = \begin{bmatrix} \tilde{\omega}_x \\ \tilde{\omega}_y \\ \tilde{\omega}_z \end{bmatrix} = \begin{bmatrix} SF_{\omega,x} & -\phi_z & \phi_y \\ \phi_z & SF_{\omega,y} & -\phi_x \\ -\phi_y & \phi_x & SF_{\omega,z} \end{bmatrix} \left(\begin{bmatrix} \omega_x \\ \omega_y \\ \omega_z \end{bmatrix} + \begin{bmatrix} B_{\omega,x} \\ B_{\omega,y} \\ B_{\omega,z} \end{bmatrix} \right) \tag{2.4}$$

where B_a and SF_a are accelerometer biases and scale factors, respectively, B_ω and SF_ω are rate gyroscope biases and scale factors, respectively, and ϕ are misalignments. Thus, there are a total of 15 variables that essentially corrupt the measurements of the true and unknowable values. Table 2.3 lists the *a priori* IMU error parameter uncertainties.

Table 2.3. *A priori* IMU error parameter uncertainties.

Parameter	Accelerometer	Gyroscope
Misalignment (3σ)	0.05°	0.05°
Noise (3σ)	0.8665 mg	0.1719 °/s
Quantization	0.54 m/s	0.0618 °/s
Scale factor (3σ)	450 ppm	100 ppm
Bias (3σ)	100 μg	0.03 °/hr

2.2.3 Mars Entry Atmospheric Data System

MSL also carried the Mars EDL Instrumentation (MEDLI) suite.[39,40] MEDLI included a series of seven ports on the heat shield connected to pressure transducers that formed the Mars Entry Atmospheric Data System (MEADS). These transducers measured heat shield surface pressures during the entry and descent phases of the EDL sequence, and are essentially analogous to a flush air data system (FADS). The success of MSL marked the first time that a planetary probe has carried a dedicated flush air data system that directly applied to the reconstruction of aerodynamic and atmospheric properties. It should be noted, however, that the Viking Lander Capsules carried FADS ports (five on the heat shield and one on the backshell), but ultimately only data from the stagnation port was used to aid in reconstruction.[41,42] The MEADS science objectives[40] were to

1. Estimate angle of attack to within 0.5°,
2. Estimate angle of sideslip to within 0.5°, and
3. Measure dynamic pressure to within 2% in a 3σ sense.

Secondary objectives were to estimate Mach number, freestream density, and atmospheric winds from the pressure observations. The MEADS transducer locations on the heat shield are shown in Figure 2.9 (the nominal stagnation region during hypersonic flight is between ports 1 and 2).

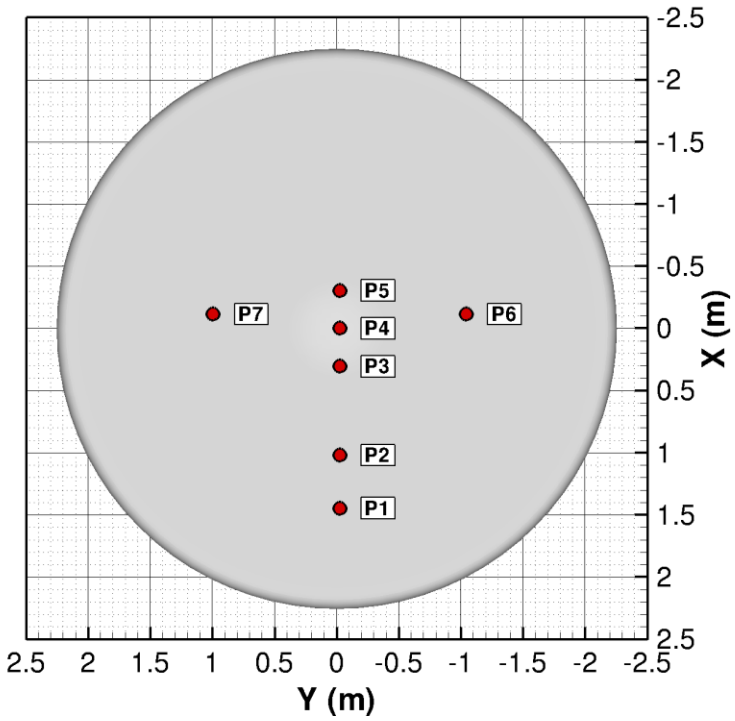

Figure 2.9. MEADS transducer port locations.[35]

MEDLI also included a series of thermocouples embedded in the heat shield to measure the thermal characteristics during entry. Analysis of data from these instruments has been performed[43,44] and will not be discussed further in this dissertation.

The MEDLI sensors were controlled by the Sensor Support Electronics (SSE) unit, a literal "black box" containing electronics to collect data and convert analog signals to digital. The SSE also monitored the spacecraft health and temperature.[40] Photographs of a MEADS transducer and the SEE are shown in Figure 2.10. Figure 2.11 shows the interior of the heat shield (i.e., the side not exposed to the incoming flow during entry) prior to spacecraft assembly. Visible in this photograph are the seven transducers linked by the orange-brown cabling and connected to the SSE box on the left side of the heat shield.

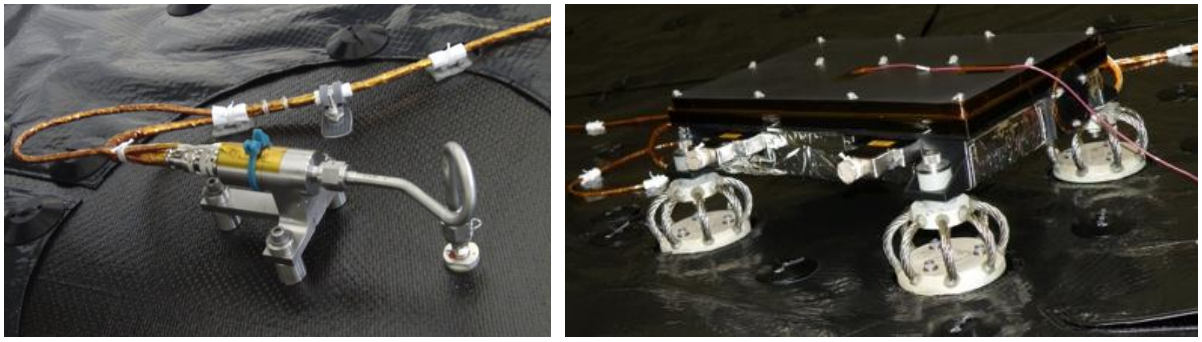

Figure 2.10. MEADS and MEDLI hardware: pressure transducer (left) and SSE (right).[*]

Figure 2.11. Interior of heat shield showing MEDLI hardware.[†]

2.3 Pre-Flight Aerodynamics

The MSL CFD aerodynamic database[45] is a tabulation of the aerodynamic pressure, force and moment coefficients and is generated using the Langley Aerothermal Upwind Relaxation Algorithm (LAURA) (see §3.1 for a discussion of the definition of pressure coefficient and §3.2 for the

[*] http://msl-scicorner.jpl.nasa.gov/Instruments/MEDLI, accessed 29 October 2013.
[†] http://mars.jpl.nasa.gov/msl/multimedia/images/?ImageID=3501, accessed 29 October 2013.

definitions of force and moment coefficients). For MSL, LAURA was run using thin layer Navier-Stokes (TLNS) equations, meaning that longitudinal viscous gradients were neglected. Pre-flight analysis indicated that these gradients did not contribute significantly to the solutions.[45]

The CFD database is separated into two sets of tables and interpolation wrappers, one for surface pressure coefficients and one for force and moment coefficients. The pressure coefficients are tabulated as a function of Mach number, angle of attack, and pressure port clock and cone angle:

$$C_{P,\mathrm{CFD}} = f\left(M_\infty, \alpha, \beta, \eta, \zeta\right) \tag{2.5}$$

Other geometric constants such as port diameter are also specified.

The force and moment coefficient tables are set up as a function of freestream velocity, Mach number and total angle of attack:

$$C_{A,\mathrm{CFD}} = f\left(V_\infty, M_\infty, \alpha_\mathrm{T}\right) \tag{2.6}$$

Depending on the flow regime, either velocity or Mach number is used to interpolate into the tables (Knudsen number may also be used). These parameters will be defined in Chapter 3.

The force and moment coefficient database accounts for the base pressure correction, which is an adjustment to the pressure and axial force coefficient below Mach 6 due to backshell flowfield effects. The correction is

$$C_{P,base} = -C_{A,base} = a_0 + \frac{a_1}{M_\infty} + \frac{a_2}{M_\infty^2} + \frac{a_3}{M_\infty^3} \tag{2.7}$$

where $a_0 = 0.0083253$, $a_1 = 0.112933$, $a_2 = -1.801004$, and $a_3 = 1.288481$.[45] This correction is sometimes referred to as the Viking base pressure correction because the constants are derived from measurements taken by the Viking entry vehicles.*

It is necessary to note the relationship between the surface pressure coefficient and the axial force coefficient. For a blunt body, the axial force coefficient is approximately equal to the integral of the pressure coefficient across the surface of the heat shield with corrections for backshell/base pressure contributions, or

$$C_A \approx \iint_S C_P dS + C_{A,base} \tag{2.8}$$

The implications of this relationship will be discussed further in Chapters 5 and 6.

LAURA surface pressure coefficient solutions near the stagnation region are well-characterized and are supported by analytical flowfield solutions. However, confidence in LAURA solutions decreases near the edges of the heat shield where the surface deflection angle increases sharply and no analytical solutions exist. This leads to larger variances in CFD surface pressure distribution

* The 1976 Viking entry vehicles were the first, and so far only, capsules equipped with FADS pressure ports on the backshell. The base pressure adjustment described here was derived (though not published) from these measurements by R. A. Mitcheltree of NASA Langley Research Center, and has also been used for the Pathfinder, MER, and Phoenix entry vehicles.

solutions near these areas.[46] Thus, while there may be relatively low uncertainty in the CFD surface pressure coefficient at a given point, particularly at the stagnation region, the uncertainty in the CFD axial force coefficient, which is strongly dependent on the surface pressure coefficient distribution per Eq. (2.8), is significantly higher. The CFD uncertainties will be discussed further in §5.3.

2.4 Landing Site

The MSL landing site was determined by the MSL Landing Location Working Group from MARDI data relative to a surface map derived from the High Resolution Imaging Science Experiment (HiRISE). Note that because the IMU used in the reconstruction process was located on the descent stage, the altitude at touchdown was 9.4 m, which is equivalent to the length of the descent stage tether and the height of the rover. The targeted and measured landing site values are listed in Table 2.4.[47]

Table 2.4. MSL targeted and measured landing site.

Parameter	Targeted	Measured
East longitude λ	137.4019°	137.4417°
Areocentric latitude δ	-4.5965°	-4.5895°
Radius r	3391134.0 m	3391133.3 m
Radius + tether & rover (9.4 m)	--	3391142.7 m

Landing site uncertainties from radio tracking were unavailable, so it is assumed that the landing site is known to an accuracy of 150 m in any direction. This assumption may be interpreted differently depending on the assumed probability distribution. For a uniform distribution, 150 m is interpreted to be the bounds of the interval on which the distribution is nonzero. For a normal distribution, 150 m is interpreted to be the standard deviation in a 3σ sense. See §3.3 for further discussion of probability distributions. The measured landing site will also be referred to in this work as the reference landing site.

2.5 Flight Data

Existing orbital assets such as Mars Reconnaissance Orbiter (MRO) enabled high-bandwidth communications between MSL and Earth tracking stations. Accelerations in the descent stage frame are shown in Figure 2.12, angular rates are shown in Figure 2.13. Significant EDL events are labeled to identify causes of change in signal behavior.

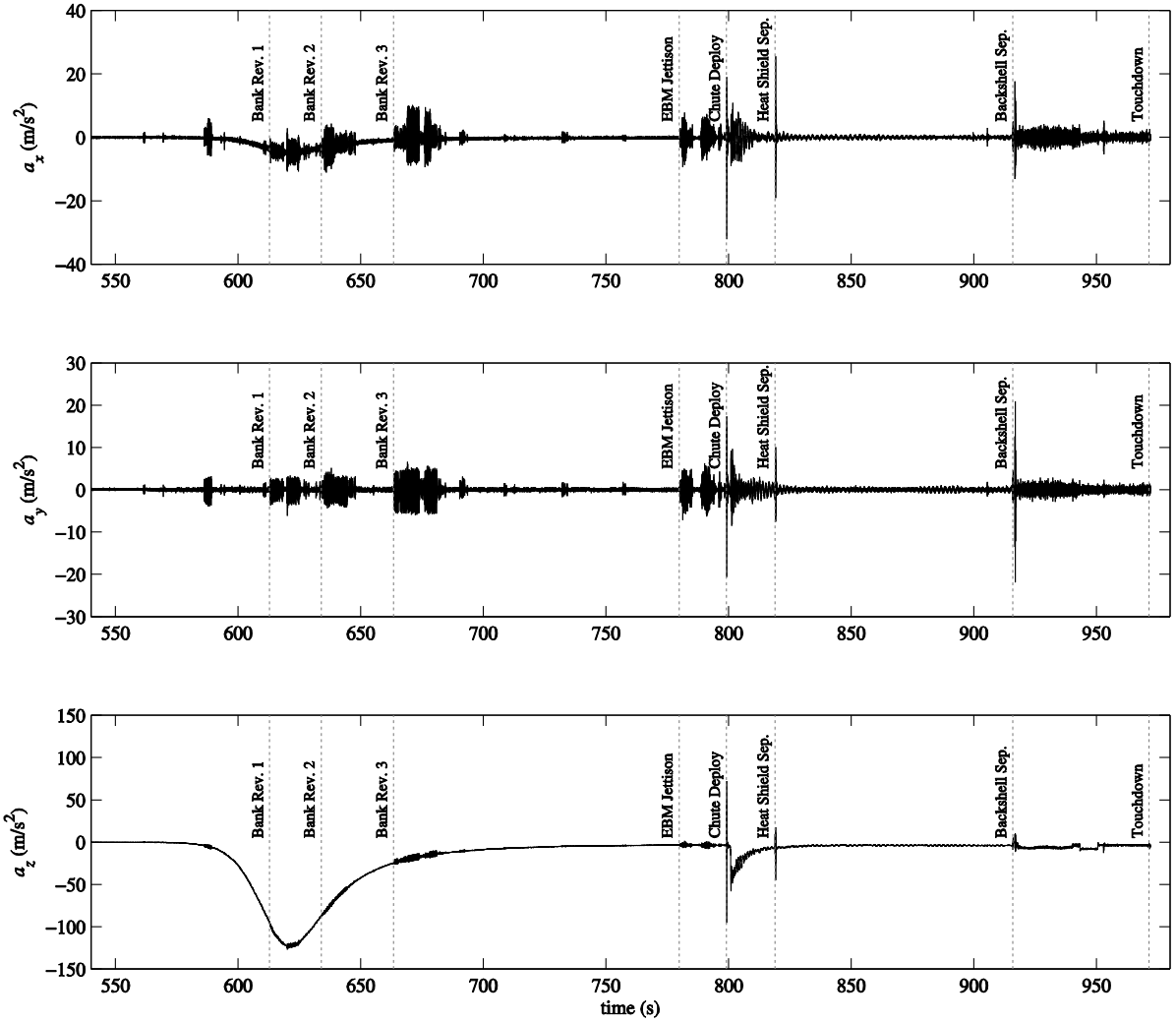

Figure 2.12. Body frame accelerations.

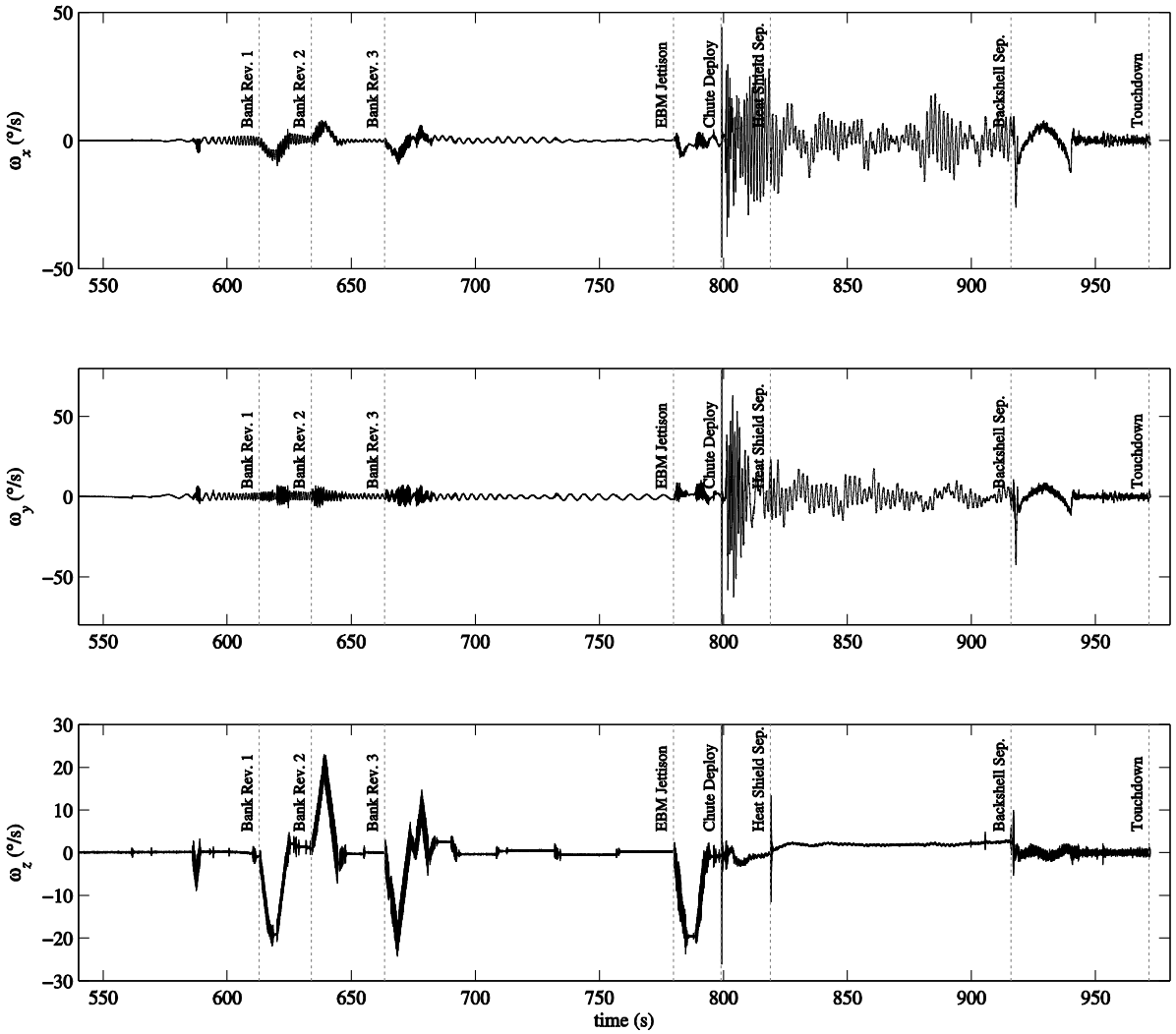

Figure 2.13. Body frame angular rates.

The MSL IMU data consists of 200 Hz engineering unit accelerations **a** and angular rate measurements $\boldsymbol{\omega}$ expressed in the body frame. The data are interpolated to a unified time vector with 0.005 s time intervals using a nearest-neighbor technique to satisfy the uniform time step requirement of the integrator. The onboard navigation computer provides filtered accelerations at 64 Hz.

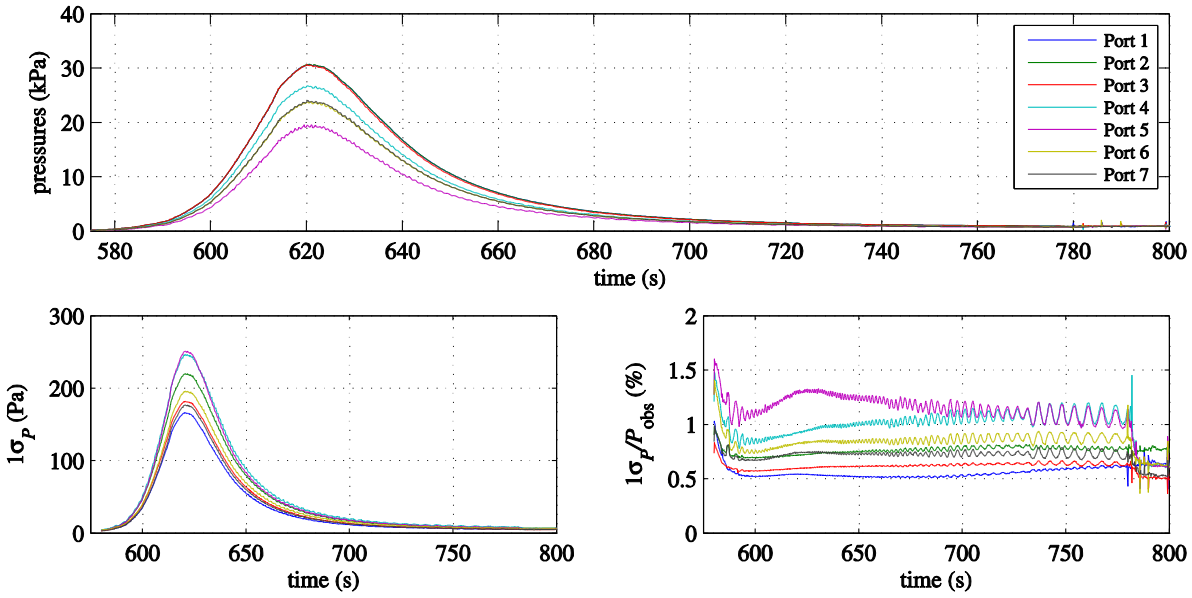

Figure 2.14. MEADS pressure measurements and *a priori* uncertainties as absolute values and percentage of observations.

Pressure data were collected at 8 Hz by the MEADS transducers and are shown with the instrument uncertainties[48] in Figure 2.14. The onboard navigation computer tagged each of the seven pressure histories with a separate time vector. The pressure measurements are interpolated to the time vector associated with port 4 and smoothed using a 3-point running mean.

Chapter 3: Elements of Atmospheric Entry Navigation

In this chapter the topics, theories, and definitions that form the basis of navigation in the context of trajectory and atmosphere reconstruction are established. A brief overview of compressible flow and applications to flush air data systems is first presented. The various coordinate systems and parameters that will be used throughout this work are then defined, followed by an overview of concepts in probability, statistics and estimation theory as it pertains to the present work.

3.1 Compressible Flow

This review of compressible flow is intended to provide a framework for understanding the fundamental aspects of entry, descent, and landing. Thorough treatments of compressible flow and hypersonic flight are provided in Refs. 49, 50, and many other textbooks.

Compressible flow is a moving fluid that is susceptible to changes in density ρ as a function of pressure *P*, such that

$$d\rho = \rho\tau dP \tag{3.1}$$

where τ is a measure of the compressibility of the fluid. Generally, gases have much higher compressibility than liquids (i.e., $\tau_{gas} > \tau_{liquid}$), so that small changes in pressure produce large changes in density. Thus, for compressible flow, Bernoulli's equation

$$P + \tfrac{1}{2}\rho V^2 = \text{const} \tag{3.2}$$

is *not applicable*. Conversely, a theoretical incompressible flow has constant density, and is useful for the study of low-speed vehicles such gliders and those used in general aviation.

Comparison of flows may be accomplished using speed of sound,

$$a = \sqrt{\frac{v}{\tau_s}} \tag{3.3}$$

where v is the volume and the subscript s on the compressibility factor indicates isentropic compressibility, i.e., the compression process is adiabatic and reversible. From this equation, it is evident that an incompressible fluid may be defined as a fluid in which the speed of sound approaches infinity, that is, in the limit as τ_s approaches zero.

For a calorically perfect gas, Eq. (3.3) may be written as

$$a = \sqrt{\frac{\gamma P}{\rho}} \tag{3.4}$$

Using the equation of state $P = \rho RT,$ the speed of sound may then be expressed as

$$a = \sqrt{\gamma RT} \tag{3.5}$$

where γ is the ratio of specific heats, R is the ideal gas constant R^* divided by the molecular weight $\bar{w}$, and T is the local temperature of the fluid in kelvin. Mach number is a measure of velocity of the flow relative to the local speed of sound:

$$M \equiv V/a \tag{3.6}$$

Anderson[49] suggests that a flow may be considered compressible at approximately Mach 0.3 or if the fractional change in density, $d\rho/\rho,$ is greater than 5%, though these demarcations are not definitions.

In addition to being compressible or incompressible, fluids in motion may be categorized into different regimes based on their velocity. Table 3.1 lists the regimes and associated Mach number ranges. Note that these ranges are approximate, and there are no well-defined boundaries or transitions between the different regimes.

Table 3.1. Approximate fluid velocity regimes

Regime	Mach range
Subsonic	$0 \le M \le 0.8$
Transonic	$0.8 < M \le 1.2$
Supersonic	$1.2 < M \le 5.0$
Hypersonic	$5.0 < M$

Vehicles in entry, descent and landing trajectories pass through all of these velocity regimes, and therefore must be able to withstand the high heat environments that characterize hypersonic flow.

3.1.1 Pressure

Pressure is the ratio of a force to the area upon which that force is exerted. For example, the force of atmospheric particles impacting a spacecraft during EDL results in a pressure distribution across the surface of the heat shield.* The laws of fluid dynamics govern the behavior and characteristics of the flow around the vehicle.

Atmospheric pressure P_∞ is the pressure of the fluid at a point far from disturbances caused by the vehicle, and is also referred to as *ambient*, *static*, or *freestream* pressure. Atmospheric pressure is the result of the "weight" of the column of particles above an infinitesimally small control volume at a specified altitude; thus, this pressure increases as altitude decreases.

Total or *stagnation* pressure P_t is the pressure at the point of a body in a flow where the fluid velocity is zero. For incompressible flow, it is the sum of the static and dynamic pressures.

Dynamic pressure q_∞ is, by definition,

$$q_\infty \equiv \tfrac{1}{2}\rho_\infty V_\infty^2 \tag{3.7}$$

For incompressible flow, this quantity is exactly the difference between the total and the static pressure, i.e., $P_t = P_\infty + q_\infty$. This is *not* true for compressible flow since density is not constant.[50] Despite this lack of physical meaning for compressible flows, dynamic pressure is still used in high-speed flow and may be rewritten in a more convenient form, assuming thermally perfect flow, as

$$q_\infty = \tfrac{1}{2}\gamma P_\infty M_\infty^2 \tag{3.8}$$

This is sometimes referred to as the hypersonic dynamic pressure, but again it does not equate to $P_t - P_\infty$.

The pressure coefficient C_P is a dimensionless quantity often used to describe the pressure at a point in the fluid. It is defined as

$$C_P \equiv \frac{P_2 - P_1}{q_1} = \begin{cases} \dfrac{P_2 - P_1}{\frac{1}{2}\rho_1 V_1^2} & \text{all flows} \\ \dfrac{2}{\gamma M_1^2}\left(\dfrac{P_2}{P_1} - 1\right) & \text{compressible flow} \end{cases} \tag{3.9}$$

Generally, point 1 is taken to be far upstream, so that P_1, ρ_1, and V_1 are ambient or atmospheric conditions. Point 2 is the location of interest, typically on the surface of the body.

3.1.2 Newtonian Flow Theory and Flush Air Data Systems

Consider a blunt body in a high-speed, calorically perfect flow, such as in Figure 3.1. Now consider a point on the surface of the body and exposed to the flow, such as a FADS pressure port. At the *i*th port, the pressure coefficient from Eq. (3.9) is

* It may be intuitive to imagine a vehicle in motion relative to an essentially stationary atmosphere or fluid, as is typically the case, but it is traditional in the study of flight to instead consider the fluid in motion around the vehicle.

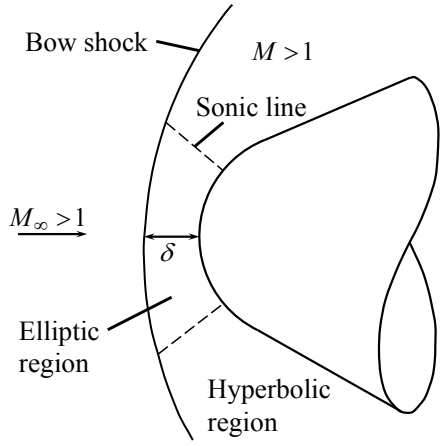

Figure 3.1. Blunt body in high-speed flow.

$$C_{P,i} \equiv \frac{P_i - P_\infty}{q_\infty} \tag{3.10}$$

Solving for P_i yields

$$P_i = q_\infty C_{P,i} + P_\infty \tag{3.11}$$

Substituting Eq. (3.8) into Eq. (3.11) yields the equation for the pressure at the *i*th FADS port:

$$P_i = \tfrac{1}{2}\gamma P_\infty M_\infty^2 C_{P,i} + P_\infty \tag{3.12}$$

It is informative to examine how this pressure may be modeled using Newtonian flow approximations, which state that the pressure coefficient at a point on a surface in a flow field is a function of the surface deflection angle θ at that point. Newton's classical sine-squared equation[50] describing this behavior was first published in his *Principia* in 1687:

$$C_P = 2\sin^2\theta \tag{3.13}$$

Newton's attempt to describe incompressible flow, though elegant, is exact only in the limits $M_\infty \to \infty$ and $\gamma \to 1$. A more general form of this equation was introduced by Lester Lees[50] in 1955:

$$C_P = C_{P,\max}\sin^2\theta \tag{3.14}$$

where $C_{P,\max}$ is the value of the pressure coefficient at the stagnation point, i.e., the total pressure coefficient.

In the context of flush air data systems, it is useful to re-define the incidence angle[*] θ as the angle between the freestream velocity vector $\mathbf{V}_\infty$ and the unit vector normal to the *i*th port $\hat{\mathbf{h}}_i$, where

[*] In Anderson's nomenclature (Ref. 50), this "re-defined" angle is ϕ.

$$\mathbf{V}_\infty = V_\infty \left[\cos\alpha\cos\beta\hat{\mathbf{i}} + \sin\beta\hat{\mathbf{j}} + \sin\alpha\cos\beta\hat{\mathbf{k}} \right] \tag{3.15}$$

$$\hat{\mathbf{h}}_i = \cos\eta_i\hat{\mathbf{i}} + \sin\eta_i\cos\zeta_i\hat{\mathbf{j}} + \sin\eta_i\sin\zeta_i\hat{\mathbf{k}} \tag{3.16}$$

and V_∞ is the magnitude of the velocity vector, α is angle attack, β is angle of sideslip, η_i is the cone angle, and ζ_i is the clock angle of the pressure port (see §3.2 for definitions of these parameters).[25] This is shown in Figure 3.2.

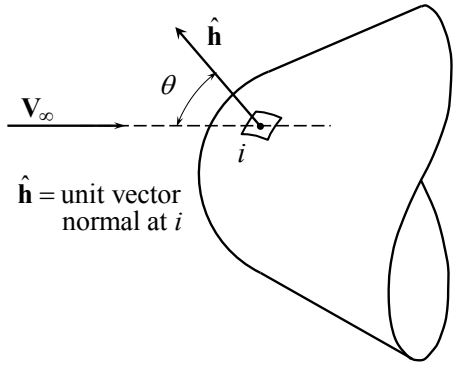

Figure 3.2. FADS pressure port vectors.

From the definition of the dot product, $\mathbf{V}_\infty \cdot \hat{\mathbf{h}}_i = V_\infty \cos\theta_i$ and

$$\cos\theta_i = \cos\alpha\cos\beta\cos\eta_i + \sin\beta\sin\eta_i\cos\zeta_i + \sin\alpha\cos\beta\sin\eta_i\sin\zeta_i \tag{3.17}$$

Thus, at the *i*th FADS port, for $M_\infty \gg 1$, the measured local pressure may be approximated as

$$C_{P,i} = C_{P,i}\cos^2\theta_i \tag{3.18}$$

$$P_i = \left(P_t - P_\infty\right)\cos^2\theta_i + P_\infty \tag{3.19}$$

where the cosine-squared term is defined by Eq. (3.17). Note the change from sine-squared to cosine-squared, which arises from re-defining the incidence angle. It is useful to rewrite Eq. (3.19) as

$$P_i = P_t\left[\left(1-R\right)\cos^2\theta_i + R\right] \tag{3.20}$$

where *R* is the ratio of static pressure to total pressure (not to be confused with the ideal gas constant). The ratio *R* is dependent on the flow regime:

$$R \equiv \frac{P_\infty}{P_t} = \begin{cases} \left[\frac{2}{(\gamma+1)M_\infty^2}\right]^{\frac{\gamma}{\gamma-1}} \left[\frac{2\gamma M_\infty^2 - (\gamma-1)}{\gamma+1}\right]^{\frac{1}{\gamma-1}} & \text{for } M_\infty > 1 \\ \left(1 + \frac{\gamma-1}{2} M_\infty^2\right)^{-\frac{\gamma}{\gamma-1}} & \text{for } M_\infty \le 1 \end{cases} \tag{3.21}$$

For Mach numbers greater than unity, R is described by the Rayleigh-Pitot equation derived from the normal shock relations and assumes the flow is adiabatic and thermally and calorically perfect. For subsonic flow, R is derived from the compressible continuous one-dimensional flow relations and assumes the flow is isentropic (i.e., adiabatic and reversible) and thermally and calorically perfect.[51] It will be shown in §4.3.3, at high Mach numbers the ratio R becomes constant.

In summary, the measured pressure at a FADS port is a function of the atmosphere, vehicle velocity, wind angles, and port location:

$$P_i = f\left(P_\infty, \rho_\infty, T_\infty, V_\infty, \alpha, \beta, \gamma : \eta_i, \zeta_i\right) \tag{3.22}$$

or, more compactly,

$$P_i = f\left(P_\infty, q_\infty, M_\infty, \alpha, \beta, \gamma : \eta_i, \zeta_i\right) \tag{3.23}$$

where the colon separates the flow variables from the geometric variables.

Pruett *et al*.[25] determined that in the case of a body in a high-speed, compressible, steady, adiabatic flow, neglecting gravitational forces, there are four independent variables:

$$P_i = f\left(q_\infty, M_\infty, \alpha, \beta : \eta_i, \zeta_i\right) \tag{3.24}$$

where again the colon separates the flow variables from the geometric variables. These four variables are not unique, however, since Mach number, dynamic pressure, total pressure, and freestream pressure are related by Eqs. (3.8) and (3.21). Thus, in addition to angle of attack α and sideslip angle β, any two variables from the set $[P_t, P_\infty, q_\infty, M_\infty]$ may be estimated simultaneously.

Although Newtonian flow approximations may give reasonable estimates of port pressures, in most cases it is preferential to use models derived from CFD or wind tunnel experiments that are more representative of the trajectory and environment.

3.2 Coordinate System and Parameter Definitions

The state of the vehicle is generally defined relative to a coordinate system, or reference frame. All reference frames used in this dissertation are right-handed and orthogonal and are categorized as either inertial or non-inertial. Inertial frames are homogeneous and isotropic systems in which Newton's laws of motion are valid, e.g., bodies move with uniform velocity or remain at rest until acted upon by external forces. Inertial frames may either be at rest or move with uniform velocity.

Non-inertial reference frames are systems that undergo acceleration, rotation, nutation, and/or precession. In either case, three elements are required to completely define the coordinate system:

1. *Origin*. The center of the coordinate system, commonly selected to be at the center of a planet or other mass.
2. *Fundamental plane*. A two-dimensional plane that passes through the origin and is normal to the +*z* axis. Common examples are a planetary equator or orbital plane.
3. *Fundamental direction*. Direction of the +*x* axis. Together with the origin and fundamental plane, the fundamental direction defines the orientation of the coordinate system. A common example is the vernal equinox, which is the ascending node or intersection of the Earth orbital plane with respect to the Earth equator.

A fourth element, the *reference time* or *epoch*, is often used in celestial mechanics where bodies are always in motion relative to each other. The epoch is used to define the orientation of the coordinate system at a point in time, often when it has some physical significance. In these cases, it is customary to say that the coordinate system is "of date" or "of epoch," where date refers to a specific time or range of time. A common epoch is J2000, which is the Julian date at 12:00:00 ET (noon) of 1 January 2000 CE, or 2451545.0.* If the reference time is selected so that it varies across some range, then the frame is non-inertial.

Reference frame notation in the present work will follow the following conventions:

- Reference frames are indicated by non-italicized acronyms. For example, the descent stage reference frame is identified by the acronym DS.
- When used as *superscripts* and paired with a vector or component of a vector, these acronyms indicate the reference frame in which that vector is expressed. For example, $\mathbf{a}^{\mathrm{DS}}$ is the spacecraft acceleration vector **a** represented in the descent stage frame DS.
- When used as *subscripts* and paired with the symbols *x*, *y*, and *z*, these acronyms indicate the axes of the reference frame. For example, x_{DS}, y_{DS}, and z_{DS} are the axes of the descent stage frame DS.
- The components of a three-dimensional vector in Euclidean space are indicated by the subscripts *x*, *y*, and *z*. For example, the vector $\mathbf{a}^{\mathrm{DS}} = [a_x^{\mathrm{DS}}, a_y^{\mathrm{DS}}, a_z^{\mathrm{DS}}]^{\mathrm{T}}$ are the vehicle accelerations **a** expressed in the descent stage frame DS which is in turn described by axes x_{DS}, y_{DS}, and z_{DS}.
- Transformations between reference frames are indicated by a matrix (typically C) with two superscripts separated by a forward slash, where the right superscript is the starting frame and the left superscript is the ending frame. For example, the equation $\mathbf{a}^{\mathrm{b}} = \mathrm{C}^{\mathrm{b/DS}}\mathbf{a}^{\mathrm{DS}}$ describes

* The Julian date is the number of days elapsed since noon of 1 January 4713 BCE.

the acceleration vector **a** represented in the descent stage frame DS, transformed to the reference frame b by the rotation matrix $C^{b/DS}$.

This notation will be used when explicit identification of the frame is required, such as when different reference frames are being used in a single equation. In situations where the reference frame is implied by context or explicitly stated, this notation will be dropped.

3.2.1 Inertial Coordinate Systems

There are three major inertial coordinate systems used in this dissertation: the Mars-centered Earth mean equator and equinox of J2000 frame, the Mars-centered Mars mean equator and prime meridian of J2000 frame, and the Mars-centered Mars mean equator and prime meridian of t_0 frame. The first two are general to Mars EDL missions and are thoroughly described in Ref. 52. The third inertial frame is specific to MSL.

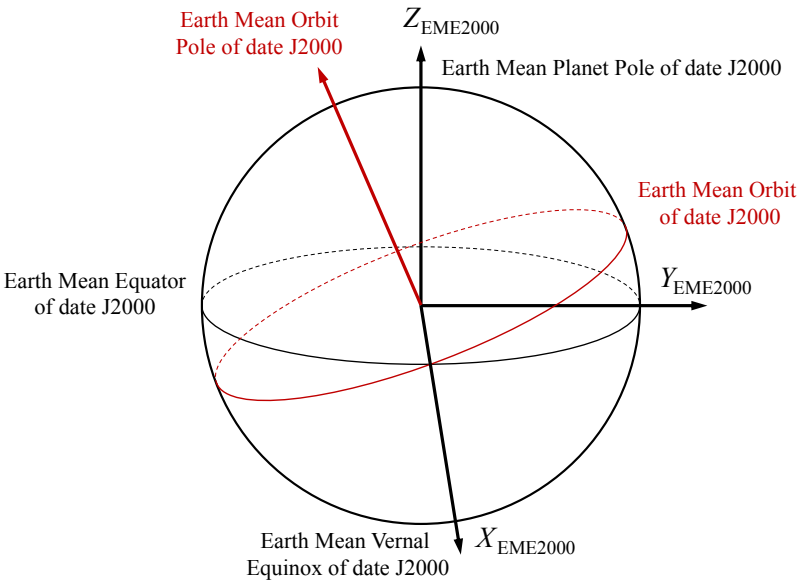

Figure 3.3. Mars-centered Earth mean equator and equinox of J2000 frame (EME2000).

The Mars-centered Earth mean equator and equinox of J2000 frame (EME2000), shown in Figure 3.3, is the frame from which all other inertial Mars frames in this work are described. It does not include any information about the orientation or orbit of Mars as it is simply the classical Earth-centered frame translated to the center of Mars. The $+z_{EME2000}$ axis is normal to the Earth mean

equator at epoch J2000, the $+x_{\text{EME2000}}$ axis is parallel to the vernal equinox of the Earth mean orbit at epoch J2000, and the $+y_{\text{EME2000}}$ axis completes the right-handed orthogonal coordinate system.

It is necessary to define elements that relate the Mars reference frames to the Earth mean equator and equinox of J2000 frame using the node Q and the IAU vector. Q is defined to be the ascending node of the Mars mean equator of date plane with respect to the Earth mean equator of J2000 plane. The IAU vector is defined to be the vector that originates at the center of Mars and points towards the node Q. Thus, the IAU vector is a function of the location of the Mars pole and not fixed in inertial space, though fundamental directions may be defined with respect to it at specified epochs. Note that the IAU vector may also be defined as the cross product between the EME2000 pole vector and the Mars pole vector of date.

From these elements, the location of the Mars prime meridian and pole may be described. By historical convention, the Mars prime meridian is defined to be the longitudinal line that passes through crater Airy-0.[53] The right ascension λ of the prime meridian is the angle between the IAU vector (of date) and intersection of the prime meridian with the Mars mean equator of date, measured positive Eastward:

$$\lambda = \lambda_0 + \Omega t_d = 176.630° + (350.89198226°)t_d \tag{3.25}$$

where λ_0 is the right ascension of the Mars prime meridian of J2000 in degrees, Ω is the angular rotation rate of Mars in degrees per day, and t_d is the number of days since the J2000 reference epoch to date. The location of the Mars pole is described by right ascension α and declination δ in the EME2000 frame:

$$\alpha = \alpha_0 - a_0 t_c = 317.68143° - 0.1061 t_c \tag{3.26}$$

$$\delta = \delta_0 - b_0 t_c = 52.8865° - 0.0609 t_c \tag{3.27}$$

where t_c is the number of Julian centuries since J2000 to date such that $t_c = \left(t_{\text{date}} - 2451545\right)/36525$ and t_{date} is the reference time.

The Mars-centered Mars mean equator and prime meridian of J2000 frame (MME2000) is shown in Figure 3.4. The origin of this frame is the center of Mars, the fundamental plane is the Mars mean equator, and the fundamental direction is the intersection of the fundamental plane with the Mars prime meridian at J2000, i.e., the IAU vector of J2000. The reference epoch for this frame is J2000, so that $t_c = t_d = 0$.

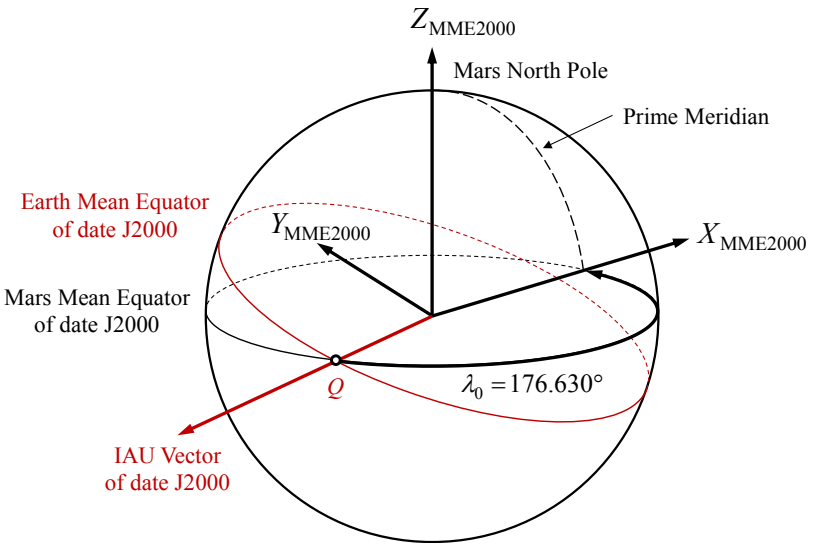

Figure 3.4. Mars-centered Mars mean equator and prime meridian of J2000 frame (MME2000).

The third inertial coordinate system is the Mars-centered Mars mean equator and prime meridian of t_0 frame (M) and is shown in Figure 3.5. The origin of this frame is the center of Mars, the fundamental plane is the Mars mean equator, and the fundamental direction is the intersection of the fundamental plane with the Mars prime meridian at epoch t_0. The reference time t_0 is defined to be 9 minutes (540 s) prior to MSL entry interface and corresponds to a Julian date of 2456145.71033450. The right ascension of the Mars prime meridian on the Mars mean equator at this epoch is $\lambda = 288.99902397°$. JPL defines the quaternion describing the transformation from EME2000 to M as

$$\boldsymbol{q}^{\text{MME2000/M}} = \begin{bmatrix} 0.16234458063 \\ 0.27379507615 \\ -0.19169632531 \\ 0.92840347494 \end{bmatrix} \tag{3.28}$$

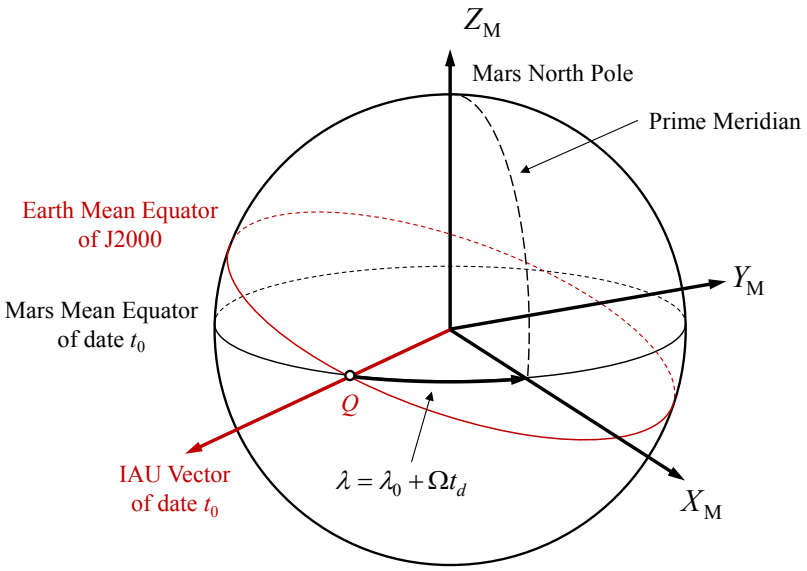

Figure 3.5. Mars-centered Mars mean equator and prime meridian of t_0 frame (M).

3.2.2 Non-Inertial Coordinate Systems

Most observations and aerodynamic parameters are defined relative to non-inertial coordinate systems fixed to the moving vehicle. The cruise frame, spacecraft frame, descent stage frame, and rover frame described in §2.2.1 are examples of non-inertial coordinate systems used for MSL.

In classical flight dynamics, it is common to use a frame in which the $+x$ axis is pointed towards the nose of the vehicle, the $+y$ axis is pointed out of the right wing, and the $+z$ is pointed down towards the ground in straight, level flight, completing the right-handed orthogonal system. This is referred to as the body frame (b), and the relationship between this frame and the MSL descent stage frame is shown in Figure 3.6.

The body frame is simply the descent stage frame rotated -90° about the $+y_{DS}$ axis, so that the body x axis is aligned with the spacecraft axis of symmetry. The transformation matrix from the descent stage frame to the body frame is therefore

$$C^{b/DS} = \begin{bmatrix} 0 & 0 & 1 \\ 0 & 1 & 0 \\ -1 & 0 & 0 \end{bmatrix} \tag{3.29}$$

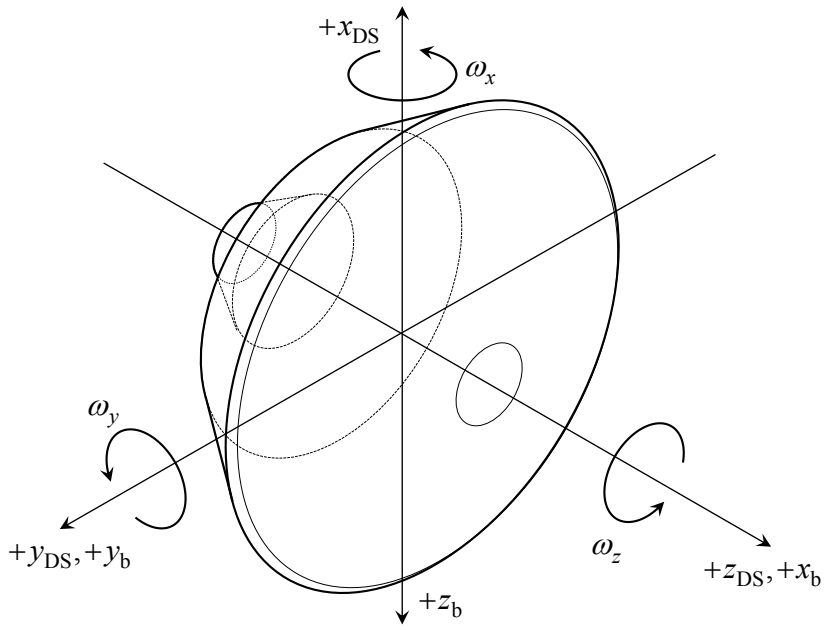

Figure 3.6. Relationship between MSL descent stage (DS) and body (b) coordinate systems.

3.2.3 Trajectory Parameters

The trajectory, which consists of the vehicle location, speed, and orientation, is typically described in an inertial frame. The position and velocity are the vectors describing the spacecraft location in the inertial frame M shown in Figure 3.5:

$$\mathbf{r} = [r_x \quad r_y \quad r_z]^{\mathrm{T}} = [X \quad Y \quad Z]^{\mathrm{T}} \tag{3.30}$$

$$\mathbf{v} = [v_x \quad v_y \quad v_z]^{\mathrm{T}} = [V_X \quad V_Y \quad V_Z]^{\mathrm{T}} \tag{3.31}$$

The first three components in Eqs. (3.30) and (3.31) are strictly consistent with the notation scheme described earlier in this section. The second three components are consistent with how position and velocity components are typically described in the literature, and will be used for the remainder of this work.

The attitude of the spacecraft is described by the quaternion

$$\boldsymbol{q} = q_1\hat{i} + q_2\hat{j} + q_3\hat{k} + q_4 \tag{3.32}$$

where q_4 denotes the scalar component and the magnitude (scalar norm) of $\boldsymbol{q}$ is 1, i.e., $\boldsymbol{q}^{\mathrm{T}}\boldsymbol{q} = 1$. The components of the quaternion are described by[22]

$$\begin{bmatrix} q_1 \\ q_2 \\ q_3 \\ q_4 \end{bmatrix} \equiv \begin{bmatrix} e_1 \sin(\theta/2) \\ e_2 \sin(\theta/2) \\ e_3 \sin(\theta/2) \\ \cos(\theta/2) \end{bmatrix} \tag{3.33}$$

where $\hat{\mathbf{e}} = [e_1, e_2, e_3]^{\mathrm{T}}$ is the Euler axis about which the angle θ completely describes the rotation of the rigid body. The quaternion may also be expressed as a direction cosine matrix:

$$\mathrm{C} = \begin{bmatrix} q_1^2 - q_2^2 - q_3^2 + q_4^2 & 2(q_1 q_2 + q_3 q_4) & 2(q_1 q_3 - q_2 q_4) \\ 2(q_1 q_2 - q_3 q_4) & -q_1^2 + q_2^2 - q_3^2 + q_4^2 & 2(q_2 q_3 + q_1 q_4) \\ 2(q_1 q_3 + q_2 q_4) & 2(q_2 q_3 - q_1 q_4) & -q_1^2 - q_2^2 + q_3^2 + q_4^2 \end{bmatrix} \tag{3.34}$$

While quaternions are commonly used in computer codes for integration purposes, it is also common to express the orientation as Euler angles. The quaternion may be converted to a 3-2-1 set of Euler angles, i.e., successive rotations of yaw angle ψ, pitch angle θ, and roll angle ϕ by

$$\begin{bmatrix} \phi \\ \theta \\ \psi \end{bmatrix} = \begin{bmatrix} \arctan \dfrac{2(q_4 q_1 + q_2 q_3)}{1 - 2(q_1^2 + q_2^2)} \\ \arcsin(2 q_4 q_2 - 2 q_3 q_1) \\ \arctan \dfrac{2(q_4 q_3 + q_1 q_2)}{1 - 2(q_2^2 + q_3^2)} \end{bmatrix} \tag{3.35}$$

The computer function "atan2" is normally used instead of the arctangent.[54] Conversely, the 3-2-1 Euler angles may be converted to quaternions by

$$\begin{bmatrix} q_1 \\ q_2 \\ q_3 \\ q_4 \end{bmatrix} = \begin{bmatrix} \sin\frac{\phi}{2}\cos\frac{\theta}{2}\cos\frac{\psi}{2} - \cos\frac{\phi}{2}\sin\frac{\theta}{2}\sin\frac{\psi}{2} \\ \cos\frac{\phi}{2}\sin\frac{\theta}{2}\cos\frac{\psi}{2} + \sin\frac{\phi}{2}\cos\frac{\theta}{2}\sin\frac{\psi}{2} \\ \cos\frac{\phi}{2}\cos\frac{\theta}{2}\sin\frac{\psi}{2} - \sin\frac{\phi}{2}\sin\frac{\theta}{2}\cos\frac{\psi}{2} \\ \cos\frac{\phi}{2}\cos\frac{\theta}{2}\cos\frac{\psi}{2} + \sin\frac{\phi}{2}\sin\frac{\theta}{2}\sin\frac{\psi}{2} \end{bmatrix} \tag{3.36}$$

The altitude is nominally the difference between the Euclidean norm of the inertial position vector and the mean equatorial radius of the planet R:

$$h = |\mathbf{r}| - R = \sqrt{X^2 + Y^2 + Z^2} - R \tag{3.37}$$

3.2.4 Aerodynamic Parameters

Aerodynamic forces, moment coefficients, and wind-relative angles α and β are shown in Figure 3.7. In the present work, Mach number M_∞ and dynamic pressure q_∞ are considered aerodynamic parameters because of their dependence on vehicle velocity. Definitions for Mach

number and dynamic pressure are listed in Eqs. (3.6) and (3.8), respectively. Refer to §3.1 for further discussion of these parameters in the context of compressible flow.

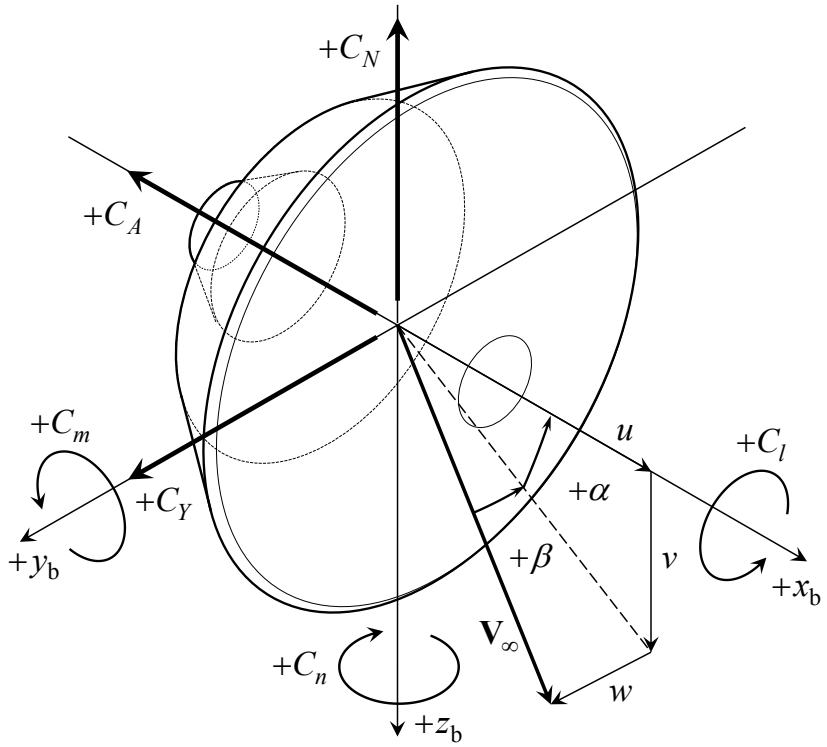

Figure 3.7. MSL body coordinate system with wind angles and aerodynamic forces and moments.

The atmosphere-relative vehicle velocity in the inertial frame M is

$$\mathbf{V}_\infty = \mathbf{v} - \boldsymbol{\Omega} \times \mathbf{r} + \mathbf{W} \tag{3.38}$$

where $\mathbf{V}_\infty = [u, v, w]^{\mathrm{T}}$, $\mathbf{r}$ and $\mathbf{v}$ are the position and velocity vectors from Eqs. (3.30) and (3.31), respectively, and $\boldsymbol{\Omega} = [0, 0, \Omega]^{\mathrm{T}}$ where $\Omega = 7.088212079 \times 10^{-5}$ rad/s is the Mars rotation rate. If it is assumed that there are no winds, $\mathbf{W} = [0, 0, 0]^{\mathrm{T}}$ and Eq. (3.38) becomes the velocity relative to the stationary atmosphere, $\mathbf{V}_\infty = \mathbf{V}_{rel} = \mathbf{v} - \boldsymbol{\Omega} \times \mathbf{r}$, and may be obtained directly from the inertial navigation solution.

Angle of attack α and sideslip angle β are often referred to as wind angles and describe the orientation of the atmosphere-relative velocity:

$$\tan\alpha = \frac{w}{u} \quad -\pi \le \alpha \le \pi \tag{3.39}$$

$$\sin\beta = \frac{v}{V_\infty} \quad -\frac{\pi}{2} \le \beta \le \frac{\pi}{2} \tag{3.40}$$

where $V_\infty = \left|\mathbf{V}_\infty\right|$ and $u > 0$.

The velocity components in the body frame may be written in terms of the wind angles:

$$\begin{aligned} u &= V_\infty \cos\alpha \cos\beta \\ v &= V_\infty \sin\beta \\ w &= V_\infty \sin\alpha \cos\beta \end{aligned} \tag{3.41}$$

The total angle of attack α_T may be written as a function of the wind angles:

$$\cos\alpha_T = \cos\alpha \cos\beta \tag{3.42}$$

The forces and moments shown in Figure 3.7 are induced by the vehicle aerodynamics. They are the components of the total aerodynamic forces and moments:

$$\begin{aligned} \mathbf{F} &= A\hat{\mathbf{i}} + N\hat{\mathbf{j}} + Y\hat{\mathbf{k}} \\ \mathbf{M} &= l\hat{\mathbf{i}} + m\hat{\mathbf{j}} + n\hat{\mathbf{k}} \end{aligned} \tag{3.43}$$

where $A = -ma_x$ is the aftward axial force, $N = -ma_z$ is the upward normal force, $Y = ma_y$ is the rightward side force, l is the rolling moment (positive right-hand side down), m is the pitching moment (positive nose up), and n is the yawing moment (positive nose right). The vectors $\hat{\mathbf{i}}$, $\hat{\mathbf{j}}$, and $\hat{\mathbf{k}}$ are the unit vectors along the x_b, y_b, and z_b axes, respectively.

It is convenient to express the forces and moments as non-dimensional coefficients:

$$C_A \equiv \frac{A}{\frac{1}{2}\rho_\infty V_\infty^2 S} \quad C_N \equiv \frac{N}{\frac{1}{2}\rho_\infty V_\infty^2 S} \quad C_Y \equiv \frac{Y}{\frac{1}{2}\rho_\infty V_\infty^2 S} \tag{3.44}$$

$$C_l \equiv \frac{l}{\frac{1}{2}\rho_\infty V_\infty^2 Sc} \quad C_m \equiv \frac{m}{\frac{1}{2}\rho_\infty V_\infty^2 Sc} \quad C_n \equiv \frac{n}{\frac{1}{2}\rho_\infty V_\infty^2 Sc} \tag{3.45}$$

where ρ_∞ is the freestream density, V_∞ is the freestream velocity, S is the reference area, and c is the reference length.

3.3 Concepts in Probability and Statistics

Many of the estimation techniques used in this dissertation are formulated on concepts in probability that are briefly summarized in this section. Thorough treatments of probability as it pertains to estimation theory are presented in Refs. 20 and 21, as well as many other textbooks.

3.3.1 Functions of Random Variables

Let x be the real-number value of the result of an experiment. If the experiment is run many times and different results are obtained for each run, then x may be said to be a *random variable*. The *probability distribution function* (also referred to as the cumulative distribution function or CDF) defines the probability Pr of every possible value of x occurring, so that for the jth event that has a finite number of possible values,

$$F\left(x_j\right) = \Pr\left(x \le x_j\right) \tag{3.46}$$

where $F(-\infty) = 0$ and $F(\infty) = 1$. For example, if an unweighted six-sided die were rolled, the probability of rolling a particular value would be one in six, i.e., $\Pr(x; x = 1,2,3,4,5,6) = 1/6$. The derivative of the probability distribution function is the *probability density function*

$$p(x) = \frac{dF(x)}{dx} \tag{3.47}$$

and only exists if the distribution function is differentiable; therefore, the condition

$$F(x) = \int_{-\infty}^{x} p(x)dx \tag{3.48}$$

must be satisfied. The term $p(x)dx$ may be thought of as the probability that x is in the infinitesimal interval between x and $x + dx$. The probability density function, or PDF, is positive real everywhere and the area under the curve is equal to one:

$$\begin{aligned} 0 \le p\left(x_j\right) \le 1 \\ F(\infty) = \int_{-\infty}^{\infty} p(u)du = 1 \end{aligned} \tag{3.49}$$

It is common to describe the random variable in terms of its *moments*. Consider the univariate case where the random variable x has a probability density function $p(x)$. The first absolute moment or *expectation* of the random variable is

$$\mu \equiv E(x) = \int_{-\infty}^{\infty} xp(x)dx \tag{3.50}$$

This is also referred to as the *expected value* or *mean*[*] of x. The first central moment, $E(x - \mu)$, is zero, and not typically of interest. Thus, an absolute moment is taken about zero and a central moment is taken about the mean.

In examining second moments, consider first a function of the random variable x, $g(x)$, where the value of $g(x)$ is itself a random variable. In this case, the expectation is

$$E\left[g(x)\right] = \int_{-\infty}^{\infty} g(x)p(x)dx \tag{3.51}$$

---

[*] The expectation of the random variable is the sample mean according to the *strong law of large numbers*, which states that as the sample size increases, the sample mean *almost surely* converges to the expectation, or $\Pr\left(\lim_{n\to\infty} x_n = \mu\right) = 1$.

The second absolute moment or *mean squared value* then arises as

$$E(x^2) = \int_{-\infty}^{\infty} x^2 p(x) dx \tag{3.52}$$

The second central moment or *variance* of a random variable is the squared deviation from the mean:

$$\sigma^2 \equiv E\left[\left(x - \mu \right)^2 \right] = \int_{-\infty}^{\infty} \left(x - \mu \right)^2 p(x) dx \tag{3.53}$$

which may also be written as

$$\sigma^2 = E\left(x^2 \right) - \left[E\left(\mu \right) \right]^2 = E\left(x^2 \right) - \mu^2 \tag{3.54}$$

Two common quantities used in statistics are the *standard deviation* and the *root-mean-square*. The standard deviation σ is simply the square root of the variance and is a measure of the uncertainty of the random variable. It is a particularly useful statistic because it has the same units as the variable *x*. The root-mean-square or RMS is defined as the square root of the mean squared value $E(x^2)$, so that $\text{RMS}^2 = \mu^2 + \sigma^2$. Thus, if the random variable *x* has a mean of zero, then the standard deviation and root-mean-square are equal.

3.3.2 Functions of Random Vectors

Consider the multivariate case of random variables $x_1, x_2, ..., x_n$. The *joint probability distribution function* is

$$F\left(x_{1,j}, x_{2,j}, ..., x_{n,j} \right) = \Pr\left(x_1 \le x_{1,j}, x_2 \le x_{2,j}, ..., x_n \le x_{n,j} \right) \tag{3.55}$$

The *joint probability density function* is

$$p(x) = \frac{\partial^n}{\partial x_1 \partial x_2 ... \partial x_n} F\left(x_1, x_2, ..., x_n \right) \Big|_x \tag{3.56}$$

And again only exists if the joint distribution function is differentiable; therefore, the condition

$$F\left(x_1, x_2, ..., x_n \right) = \int_{-\infty}^{x} p\left(x_1, x_2, ..., x_n \right) dx_1 dx_2 ... dx_n \tag{3.57}$$

must be satisfied. As with the univariate case, the probability density function is positive real everywhere and the area under the hypersurface is equal to one.

Consider now the random vector $\mathbf{x}$ containing *n* elements x_i that are jointly distributed random variables, such that $\mathbf{x} = [x_1, x_2, ..., x_n]^{\mathrm{T}}$. Generally, only the first absolute and second central moments are of interest. The first absolute moment is the vector of the expected values of each element in $\mathbf{x}$, or

$$\boldsymbol{\mu} \equiv E(\mathbf{x}) = \int_{-\infty}^{\infty} \mathbf{x} p(\mathbf{x}) d\mathbf{x} \tag{3.58}$$

such that the *i*th element of $\boldsymbol{\mu}$ is

$$\mu_i \equiv E(x_i) = \int_{-\infty}^{\infty}\int_{-\infty}^{\infty}\ldots\int_{-\infty}^{\infty} x_i p(x_1, x_2, \ldots, x_n) dx_1 dx_2 \ldots dx_n \tag{3.59}$$

The second central moment or *covariance* is defined as

$$\begin{aligned}\operatorname{cov}(\mathbf{x}) = \Gamma_{\mathrm{x}} &\equiv E\left[(\mathbf{x}-\boldsymbol{\mu})(\mathbf{x}-\boldsymbol{\mu})^{\mathrm{T}}\right] \\ &= \begin{bmatrix} E\left[(x_1-\mu_1)^2\right] & E\left[(x_1-\mu_1)(x_2-\mu_2)\right] & \cdots & E\left[(x_1-\mu_1)(x_n-\mu_n)\right] \\ E\left[(x_2-\mu_2)(x_1-\mu_1)\right] & E\left[(x_2-\mu_2)^2\right] & \cdots & E\left[(x_2-\mu_2)(x_n-\mu_n)\right] \\ \vdots & \vdots & \ddots & \vdots \\ E\left[(x_n-\mu_n)(x_1-\mu_1)\right] & E\left[(x_n-\mu_n)(x_2-\mu_2)\right] & \cdots & E\left[(x_n-\mu_n)^2\right] \end{bmatrix}\end{aligned} \tag{3.60}$$

The covariance may be compactly written as

$$\Gamma_{\mathrm{x}} = \begin{bmatrix} \sigma_1^2 & \sigma_{12} & \cdots & \sigma_{1n} \\ \sigma_{21} & \sigma_2^2 & \cdots & \sigma_{2n} \\ \vdots & \vdots & \ddots & \vdots \\ \sigma_{n1} & \sigma_{n2} & \cdots & \sigma_n^2 \end{bmatrix} = \begin{bmatrix} \sigma_1^2 & \rho_{12}\sigma_1\sigma_2 & \cdots & \rho_{1n}\sigma_1\sigma_n \\ \rho_{21}\sigma_2\sigma_1 & \sigma_2^2 & \cdots & \rho_{2n}\sigma_2\sigma_n \\ \vdots & \vdots & \ddots & \vdots \\ \rho_{n1}\sigma_n\sigma_1 & \rho_{n2}\sigma_n\sigma_2 & \cdots & \sigma_n^2 \end{bmatrix} \tag{3.61}$$

where

$$\begin{aligned} \sigma_i^2 &\equiv E\left[(x_i-\mu_i)^2\right] = \text{variance of } x_i \\ \sigma_{ij} &\equiv E\left[(x_i-\mu_i)(x_j-\mu_j)\right] = \text{covariance of } x_i \text{ and } x_j \\ \rho_{ij} &\equiv \frac{\sigma_{ij}}{\sigma_i\sigma_j} = \text{correlation of } x_i \text{ and } x_j \end{aligned} \tag{3.62}$$

and the subscripts i and j refer to the ith row and jth column of the matrix, respectively. The correlation coefficient ρ_{ij} describes the linear dependence between x_i and x_j and has values between ± 1. If $\rho_{ij} = 0$, then x_i and x_j are *linearly independent*. If the joint density function may be written as

$$p(x_1, \ldots, x_n) = p_1(x_1)\ldots p_n(x_n) \tag{3.63}$$

then x_i and x_j are *statistically independent*. Like the variance in the univariate case, the covariance describes the uncertainty in **x** in a statistical sense. Note that the covariance matrix is symmetric.

A particularly useful identity of the covariance matrix arises from the linearity assumption. If A is a matrix that operates on **x**, then the covariance of A**x** is

$$\operatorname{cov}(\mathrm{A}\mathbf{x}) = \mathrm{A}\Gamma_{\mathrm{x}}\mathrm{A}^{\mathrm{T}} \tag{3.64}$$

This identity will be used in §3.4.

To summarize the relevant moments, for a random variable, the expected values of x and $(x-\mu)^2$ are the mean and variance, respectively. For a random vector, the expected values of $\mathbf{x}$ and $(\mathbf{x}-\boldsymbol{\mu})(\mathbf{x}-\boldsymbol{\mu})^{\mathrm{T}}$ are the mean and covariance, respectively.

3.3.3 Probability Distributions

Two very common probability distributions with convenient properties are *uniform* and *normal* distributions. A uniform distribution function, as its name implies, assigns the same probability to every variable in its interval. If a and b are the minimum and maximum values of the interval, then the uniform distribution function is defined by the density function

$$p(x)=\begin{cases}\dfrac{1}{b-a} & \text{for } a\le x\le b\\ 0 & \text{for } x<a \text{ or } x>b\end{cases} \tag{3.65}$$

with mean $\frac{1}{2}(a+b)$ and variance $\frac{1}{12}(b-a)^2$. The cumulative uniform distribution function is

$$F(x)=\begin{cases}0 & \text{for } x<a\\ \dfrac{x-a}{b-a} & \text{for } a\le x<b\\ 1 & \text{for } x\ge a\end{cases} \tag{3.66}$$

The probability density and cumulative distribution functions for the uniform distribution are shown in Figure 3.8.

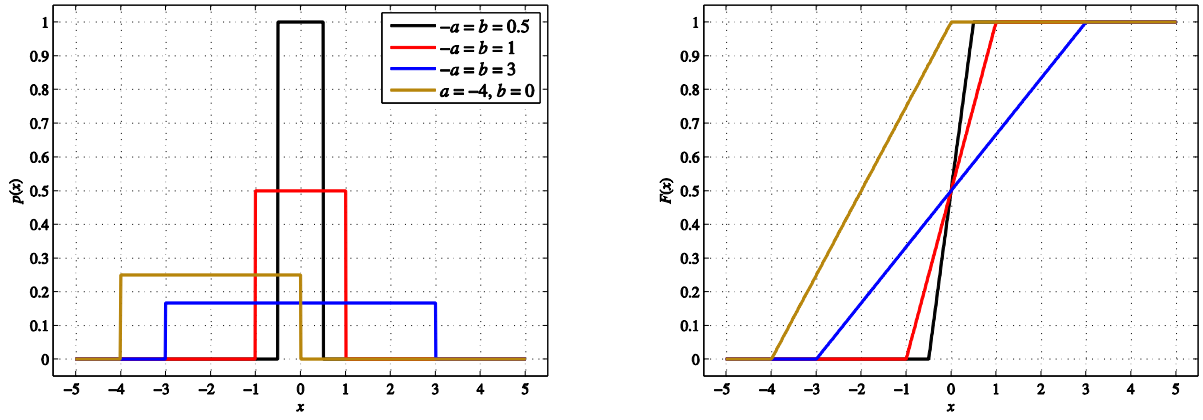

Figure 3.8. Uniform probability density and cumulative distribution functions.

The normal or Gaussian distribution function for a random variable x is defined by the density function

$$p(x) = \phi(x) = \frac{1}{\sigma\sqrt{2\pi}} \exp\left[-\frac{(x-\mu)^2}{2\sigma^2} \right] \tag{3.67}$$

with mean μ and variance σ^2. The normal cumulative distribution function is

$$F(x) = \Phi(x) = \frac{1}{\sqrt{2\pi}} \int_{-\infty}^{x} e^{-t^2/2} dt \tag{3.68}$$

The probability density and cumulative distribution functions for the univariate normal distribution are shown in Figure 3.9.

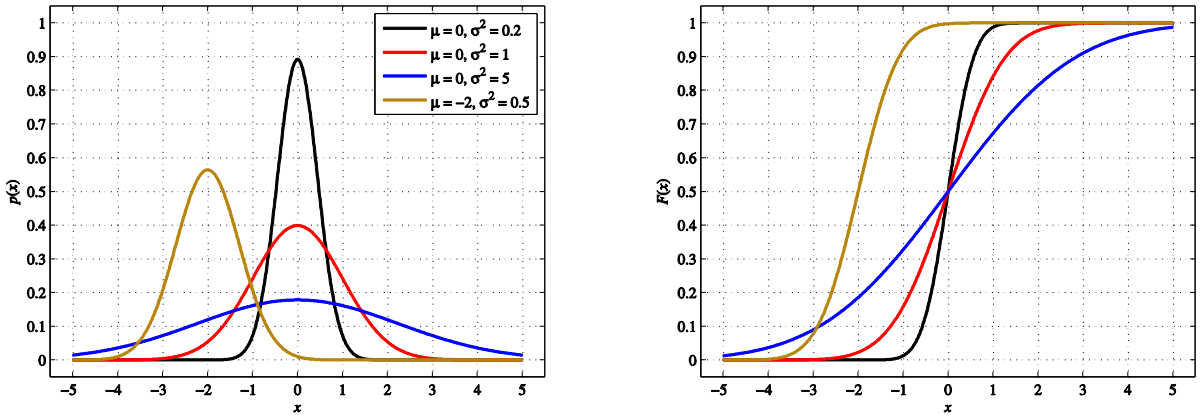

Figure 3.9. Univariate normal probability density and cumulative distribution functions.

For the multivariate case of the random vector $\mathbf{x}$, the normal density function takes the form

$$p(\mathbf{x}) = \frac{1}{\sqrt{\det(\Gamma_x)(2\pi)^n}} \exp\left[-\frac{1}{2}(\mathbf{x}-\boldsymbol{\mu})^{\mathrm{T}} \Gamma_x^{-1} (\mathbf{x}-\boldsymbol{\mu}) \right] \tag{3.69}$$

with mean $\boldsymbol{\mu}$ and covariance Γ_x. No closed-form solution exists for the multivariate normal cumulative distribution.

It is common to describe the probability of an event as being within a certain number of standard deviations from the mean, such as 1σ, 2σ, or 3σ. Given a distribution, being within $k\sigma$ is defined to be

$$F(\mu + k\sigma) - F(\mu - k\sigma) = \int_{\mu-k\sigma}^{\mu+k\sigma} p(x) dx \tag{3.70}$$

To illustrate this, consider the normal distribution. Substituting Eq. (3.68) into the left-hand side of Eq. (3.70) and assuming a mean of zero and standard deviation of one yields

$$\Pr(\mu - 2\sigma \le x \le \mu + 2\sigma) = F(2) - F(-2) = 0.9772 - (1 - 0.9772) \approx 0.9545 \tag{3.71}$$

Thus, for a univariate normal distribution, the probability of a variable being within two standard deviations of the mean is approximately 95%. Table 3.2 lists the probabilities of being within $k\sigma$ for 1-, 2-, 3-, and 4-dimensional spaces.

Table 3.2. Probability values for multiple variables with normal distributions.

Number of Variables	$k=1$	$k=2$	$k=3$
1	0.6827	0.9545	0.9973
2	0.3935	0.8647	0.9889
3	0.1987	0.7385	0.9707
4	0.0902	0.5940	0.9389

The table indicates that the probability of being within $k\sigma$ decreases dramatically as the number of variables increases. For example, for a univariate problem, there is slightly more than a 95% probability that the random variable will be inside the 2σ ellipse. When the number of variables increases to three, the probability of all three variables being inside the 2σ hypersphere reduces to just over 59%.

3.4 Statistics and Estimation Theory

This section is intended to provide the background to the statistical techniques used in some trajectory reconstruction methods. This overview is by no means exhaustive, and a thorough treatment of estimation theory, state and parameter estimation techniques, and statistics is provided in Refs. 20, 21, and many other textbooks.

Estimation theory is the field of study in which estimates of a set of state variables are determined from measurements containing random components (i.e., a noisy signal). The quality of the estimates are dependent on the amount of noise in the measurements, the accuracy of the models that represent the physical processes present in the measurements, and the optimality of the estimation technique. For the purposes of this dissertation, the terms parameter estimation, state estimation, and filtering are synonymous and will be used interchangeably.

Systems may be described as *deterministic* or *stochastic*. A deterministic or non-probabilistic system behaves in a predictable manner and contains no random elements. Given a set of inputs, analysis of a deterministic system, or use of a deterministic process, will always result in the same

outcome. A stochastic or probabilistic system behaves in a manner dependent on both predictable and random processes. In general, the behavior of stochastic systems must be estimated using mathematical models of their predicted behavior, while also taking into account the uncertainties associated with the random elements. A stochastic process may also be referred to as probabilistic.

One of the most widely-used methods of estimation is *least squares*, which will be the focus of the following two sections.

3.4.1 Least Squares Estimation

The method of least squares is a statistical regression technique of finding solutions to an over-determined system.[20,21] Legendre and Adrain published independent formulations for least squares in 1805 and 1808, respectively, though credit is typically given to Gauss who developed it as early as 1795 but did not publish until 1809.[55]

The method of least squares assumes that the measurements take the form

$$\tilde{\mathbf{y}} = \mathrm{A}\hat{\mathbf{x}} + \boldsymbol{\varepsilon} \tag{3.72}$$

where A is the sensitivity matrix relating the estimated state parameters $\hat{\mathbf{x}}$ to the observations $\tilde{\mathbf{y}}$ and $\boldsymbol{\varepsilon}$ is the vector containing the random measurement errors (or noise) with $\mu_\varepsilon = 0$ and $\Gamma_\varepsilon = E(\boldsymbol{\varepsilon}\boldsymbol{\varepsilon}^{\mathrm{T}})$. These are referred to as the *observation equations*.

Statistical estimators attempt to select an estimate that minimizes some cost function. In the case of least squares, this cost function is

$$J_{\mathrm{LS}} \equiv \frac{1}{2}\boldsymbol{\varepsilon}^{\mathrm{T}}\boldsymbol{\varepsilon} \tag{3.73}$$

Solving Eq. (3.72) for $\boldsymbol{\varepsilon}$ and substituting into Eq. (3.73), the cost function (dropping the "LS" notation) becomes

$$J = \frac{1}{2}\left(\tilde{\mathbf{y}} - \mathrm{A}\hat{\mathbf{x}}\right)^{\mathrm{T}}\left(\tilde{\mathbf{y}} - \mathrm{A}\hat{\mathbf{x}}\right) = \frac{1}{2}\left(\tilde{\mathbf{y}}^{\mathrm{T}}\tilde{\mathbf{y}} - 2\tilde{\mathbf{y}}^{\mathrm{T}}\mathrm{A}\hat{\mathbf{x}} + \hat{\mathbf{x}}^{\mathrm{T}}\mathrm{A}^{\mathrm{T}}\mathrm{A}\hat{\mathbf{x}}\right) \tag{3.74}$$

Thus, the goal is find the estimates $\hat{\mathbf{x}}$ that minimize J using the observations $\tilde{\mathbf{y}}$. To find the global minimum, two conditions must be met. From matrix calculus, the Jacobian provides the necessary condition:

$$\nabla_{\hat{\mathbf{x}}} J \equiv \begin{bmatrix} \dfrac{\partial J}{\partial \hat{\mathbf{x}}_1} \\ \vdots \\ \dfrac{\partial J}{\partial \hat{\mathbf{x}}_n} \end{bmatrix} = \mathrm{A}^{\mathrm{T}}\mathrm{A}\hat{\mathbf{x}} - \mathrm{A}^{\mathrm{T}}\tilde{\mathbf{y}} = 0 \tag{3.75}$$

The Hessian provides the sufficient condition:

$$\nabla^2_{\hat{\mathbf{x}}} J \equiv \frac{\partial^2 J}{\partial \hat{\mathbf{x}} \partial \hat{\mathbf{x}}^{\mathrm{T}}} = \mathrm{A}^{\mathrm{T}}\mathrm{A} \text{ must be positive definite} \tag{3.76}$$

Solving Eq. (3.75) yields

$$\mathrm{A}^{\mathrm{T}}\mathrm{A}\hat{\mathbf{x}} = \mathrm{A}^{\mathrm{T}}\tilde{\mathbf{y}} \tag{3.77}$$

which are commonly referred to as the *normal equations*. From matrix calculus it may be shown that $\mathrm{A}^{\mathrm{T}}\mathrm{A}$ is always positive semi-definite. If A is of full rank then $\mathrm{A}^{\mathrm{T}}\mathrm{A}$ is positive definite and therefore invertible, which yields the classical least squares estimator

$$\hat{\mathbf{x}} = \left(\mathrm{A}^{\mathrm{T}}\mathrm{A}\right)^{-1}\mathrm{A}^{\mathrm{T}}\tilde{\mathbf{y}} \tag{3.78}$$

with covariance

$$\Gamma_{\hat{\mathrm{x}}} = \left(\mathrm{A}^{\mathrm{T}}\mathrm{A}\right)^{-1} \tag{3.79}$$

In the special case where the errors are uncorrelated, have zero mean, and have equal variances (i.e., are homoscedastic), the least squares estimator provides the best linear unbiased estimates, meaning that the estimates have lower variances than any other linear estimator. This is known as the Gauss-Markov theorem.[20]

When information regarding the confidence in the parameters is known, a weighting matrix W may be introduced. W must be positive definite. In this case, the cost function becomes

$$J = \frac{1}{2}\left(\tilde{\mathbf{y}} - \mathrm{A}\hat{\mathbf{x}}\right)^{\mathrm{T}}\mathrm{W}^{-1}\left(\tilde{\mathbf{y}} - \mathrm{A}\hat{\mathbf{x}}\right) \tag{3.80}$$

leading to the weighted least squares estimator

$$\hat{\mathbf{x}} = \left(\mathrm{A}^{\mathrm{T}}\mathrm{W}\mathrm{A}\right)^{-1}\mathrm{A}^{\mathrm{T}}\mathrm{W}\tilde{\mathbf{y}} \tag{3.81}$$

with covariance

$$\Gamma_{\hat{\mathrm{x}}} = \left(\mathrm{A}^{\mathrm{T}}\mathrm{W}\mathrm{A}\right)^{-1} \tag{3.82}$$

3.4.2 Minimum Variance Estimation

Minimum variance estimation is a rigorous, statistical extension of the least squares estimator that has a variance less than or equal to any other unbiased estimate.[20] It differs from least squares in that information regarding the measurement uncertainty is introduced into the estimator, and does not assume diagonal weighting. The batch linear, unbiased minimum variance estimator is

$$\hat{\mathbf{x}} = \left(\mathrm{A}^{\mathrm{T}}\Gamma_{\varepsilon}^{-1}\mathrm{A}\right)^{-1}\mathrm{A}^{\mathrm{T}}\Gamma_{\varepsilon}^{-1}\tilde{\mathbf{y}} \tag{3.83}$$

where $\tilde{\mathbf{y}}$ is the vector of observations, A is the sensitivity or information matrix, and Γ_{ε} is the measurement covariance. The covariance of the estimate is

$$\Gamma_{\hat{\mathrm{x}}} = \left(\mathrm{A}^{\mathrm{T}}\Gamma_{\varepsilon}^{-1}\mathrm{A}\right)^{-1} \tag{3.84}$$

Note that the minimum variance estimator is identical to the batch weighted linear least squares estimator, Eq. (3.81), if the weighting matrix W is defined as the inverse of the measurement covariance Γ_ε.

The minimum variance estimator may take into account prior or *a priori* knowledge of the parameters and prevent the solution from diverging from the expected values. The minimum variance estimator with *a priori* is

$$\hat{\mathbf{x}} = \left(\mathrm{A}^{\mathrm{T}} \Gamma_\varepsilon^{-1} \mathrm{A} + \Gamma_\mu^{-1} \right)^{-1} \left(\mathrm{A}^{\mathrm{T}} \Gamma_\varepsilon^{-1} \tilde{\mathbf{y}} + \Gamma_\mu^{-1} \boldsymbol{\mu} \right) \tag{3.85}$$

where Γ_μ is the covariance associated with the *a priori* state estimates $\boldsymbol{\mu}$. Note the limiting cases: (1) if the *a priori* knowledge is poor, then $\Gamma_\mu^{-1} \to 0$ and the solution reduces to the weighted least squares estimate ($\mathrm{W} = \Gamma_\varepsilon^{-1}$), and (2) if the measurement knowledge is poor, then $\Gamma_\varepsilon^{-1} \to 0$ and the solution reduces to $\hat{\mathbf{x}}_k = \boldsymbol{\mu}$. The covariance of the final estimate is

$$\Gamma_{\hat{\mathrm{x}}} = \left(\mathrm{A}^{\mathrm{T}} \Gamma_\varepsilon^{-1} \mathrm{A} + \Gamma_\mu^{-1} \right)^{-1} \tag{3.86}$$

Compare this covariance with that of Eq. (3.84), which does not include *a priori* information. The inclusion of Γ_μ^{-1} in Eq. (3.86) ensures that the minimum variance with *a priori* covariance is always smaller than without *a priori*.

With non-linear problems, it is advantageous to use differential correction to incrementally update the solution by using prior estimates $\boldsymbol{\mu}$. The minimum variance estimator, when combined with *a priori* and differential correction, is

$$\Delta\hat{\mathbf{x}}_k = \left(\mathrm{A}^{\mathrm{T}} \Gamma_\varepsilon^{-1} \mathrm{A} + \Gamma_\mu^{-1} \right)^{-1} \left(\mathrm{A}^{\mathrm{T}} \Gamma_\varepsilon^{-1} \Delta\tilde{\mathbf{y}} + \Gamma_\mu^{-1} \left(\boldsymbol{\mu} - \hat{\mathbf{x}}_k \right) \right) \tag{3.87}$$

where $\Delta\tilde{\mathbf{y}}$ is the vector of the differences between observed and computed data, and $\hat{\mathbf{x}}_{k+1} = \hat{\mathbf{x}}_k + \Delta\hat{\mathbf{x}}_k$ provides the state estimation update. The covariance of the final estimate is the same as in the case of minimum variance with *a priori*, Eq. (3.86).

Chapter 4: Reconstruction Techniques

In this chapter various trajectory and atmosphere reconstruction techniques are presented. These techniques are the foundation of the methods developed in Chapter 5 that address the Principal Issues outlined in Chapter 1.

4.1 Classical Reconstruction Techniques

There exist some reconstruction techniques that require only observations from an inertial measurement unit to produce solutions for some trajectory and atmosphere parameters. These techniques are deterministic and have been applied to almost all missions that require post-flight trajectory reconstruction.

4.1.1 Inertial Navigation

Inertial navigation is a deterministic trajectory reconstruction technique that uses data from the inertial measurement unit to determine the vehicle position and velocity in an inertial frame. For this type of reconstruction, the only required data are the sensed accelerations $\tilde{\mathbf{a}}$ and angular rotation rates $\tilde{\boldsymbol{\omega}}$ from onboard accelerometers and gyroscopes, respectively, as well as estimates of the initial state conditions.[4]

The inertial navigation process requires that accelerations of the center of mass be integrated in the state equations, rather than the sensed accelerations. A transformation must therefore be made to account for accelerations due to angular motion of the vehicle by first computing the vector from the center of mass to the IMU:

$$\Delta\mathbf{r}_c = \mathbf{r}_{\mathrm{CM}}^{\mathrm{b}} - \mathbf{r}_{\mathrm{IMU}}^{\mathrm{b}} \tag{4.1}$$

The computed center of mass body accelerations are then

$$\mathbf{a}_{\mathrm{CM}}^{\mathrm{b}} = \tilde{\mathbf{a}}^{\mathrm{b}} - \left[\dot{\tilde{\boldsymbol{\omega}}} \times \Delta\mathbf{r}_c + \tilde{\boldsymbol{\omega}} \times \left(\tilde{\boldsymbol{\omega}} \times \Delta\mathbf{r}_c \right) \right] \tag{4.2}$$

where $\tilde{\mathbf{a}}^{\mathrm{b}}$ and $\tilde{\boldsymbol{\omega}}$ are the sensed body acceleration and angular rate vectors, respectively, and $\Delta\dot{\mathbf{r}}_c$ is assumed to be zero.

At a given time the vehicle state $\mathbf{x}$ may be expressed in an inertial frame as a function of nine parameters:

$$\mathbf{x} = \left[X, Y, Z, V_x, V_y, V_z, \theta_x, \theta_y, \theta_z \right]^{\mathrm{T}} \tag{4.3}$$

where the Euler angles represent a 3-2-1 rotation. It is convenient in inertial navigation to represent the Euler angles as quaternions for integration purposes, as in Eq. (3.32). The rate of change of the quaternion is integrated, given an initial attitude, to obtain the quaternion history using the differential equations

$$\begin{bmatrix} \dot{q}_1 \\ \dot{q}_2 \\ \dot{q}_3 \\ \dot{q}_4 \end{bmatrix} = \frac{1}{2} \begin{bmatrix} q_4 & -q_3 & q_2 \\ q_3 & q_4 & -q_1 \\ -q_2 & q_1 & q_4 \\ -q_1 & -q_2 & -q_3 \end{bmatrix} \begin{bmatrix} \tilde{\omega}_1 \\ \tilde{\omega}_2 \\ \tilde{\omega}_3 \end{bmatrix} \tag{4.4}$$

where q_4 denotes the scalar component. The vehicle orientation history, often expressed as 3-2-1 Euler angles, may then be obtained from the quaternions. The quaternions are converted to direction cosine matrices $\mathrm{C}^{\mathrm{M/b}}$ using Eq. (3.34), which is in turn used to transform the body frame accelerations to the inertial frame M:

$$\mathbf{a}^{\mathrm{M}} = \mathrm{C}^{\mathrm{M/b}} \mathbf{a}_{\mathrm{CM}}^{\mathrm{b}} \tag{4.5}$$

The position and velocity equations of motion are obtained by utilizing Newton's second law in an inertial frame:

$$\begin{aligned} \dot{\mathbf{r}} &= \mathbf{v} \\ \dot{\mathbf{v}} &= \mathbf{a} - \mathbf{g} \end{aligned} \tag{4.6}$$

where the accelerations $\mathbf{a}$ are the inertial accelerations $\mathbf{a}^{\mathrm{M}}$ from Eq. (4.5). It is necessary to compute the acceleration due to gravity $\mathbf{g}$ because accelerometers do not measure gravitational acceleration; that is, if an accelerometer were in free-fall on Earth, it would measure zero, not 9.81 m/s^2. The acceleration due to gravity is modeled up to the second spherical harmonic in the inertial frame M as

$$\mathbf{g} = \begin{bmatrix} g_X \\ g_Y \\ g_Z \end{bmatrix} = \frac{\mu}{\rho^3} \begin{bmatrix} X\left(\frac{3J_2R^2}{2\rho^2} \left\{ 5\frac{Z^2}{\rho^2} - 1 \right\} - 1 \right) \\ Y\left(\frac{3J_2R^2}{2\rho^2} \left\{ 5\frac{Z^2}{\rho^2} - 1 \right\} - 1 \right) \\ Z\left(\frac{3J_2R^2}{2\rho^2} \left\{ \left[5\frac{Z^2}{\rho^2} - 1 \right] - 2 \right\} - 1 \right) \end{bmatrix} \tag{4.7}$$

where R is the Mars mean equatorial radius and $\rho = |\mathbf{r}| = \sqrt{X^2 + Y^2 + Z^2}$.

4.1.2 Atmosphere Reconstruction

Atmosphere reconstruction is the recovery of atmospheric density, pressure, and temperature along the trajectory of the entry vehicle from the vehicle trajectory and sensed acceleration. The classical approach[14] assumes that the atmosphere behaves as an ideal gas and is in hydrostatic equilibrium.

From the axial force equation in Eq. (3.44), atmospheric density along the flight path is proportional to the axial acceleration (recall from Figure 3.7 that a positive axial force is by convention opposite in sign of a positive axial acceleration in the body frame):

$$C_A = -\frac{ma_x}{\frac{1}{2}\rho_\infty V_\infty^2 S} \tag{4.8}$$

where m is the vehicle mass, C_A is the axial force coefficient known from pre-flight CFD, and S is the vehicle aerodynamic reference area, all of which are known *a priori*. The variable V_∞ is the velocity of the entry vehicle relative to the atmosphere assuming no winds and is obtained from trajectory reconstruction. The variable a_x is the vehicle acceleration along the body x-axis expressed in the body frame, obtained from onboard accelerometers.

Eq. (4.8) may be rearranged to solve for density:

$$\rho_\infty = -\frac{2ma_x}{V_\infty^2 C_A S_{ref}} \tag{4.9}$$

Recall from §2.3 that C_A from CFD is usually obtained using Mach number as a table look-up parameter. As will be shown in the following equations, Mach number may be updated using the ratio of freestream pressure to density (or freestream temperature). This updated Mach number is then used to re-compute density, and the entire process is iterated until convergence.

Freestream atmospheric pressure is computed by assuming that the atmosphere is in hydrostatic equilibrium, meaning that the fluid is stationary and the pressure at any given altitude is due to the weight of the fluid above that altitude. The hydrostatic equation $dP_\infty = -g\rho_\infty dh$ is integrated to obtain the freestream pressure along the flight path:

$$P_\infty = P_0 - \int_h^{h_0} g\rho_\infty dh \tag{4.10}$$

where P_0 is the freestream pressure at initial altitude h_0, h is the altitude $h = r - r_0$, and ρ_∞ is the density computed from Eq. (4.9). Eq. (4.10) is written as an Euler discretization scheme of the form

$$P_{\infty,k} = P_{\infty,k-1} - g_k \rho_{\infty,k}(h_k - h_{k-1}) \tag{4.11}$$

to compute freestream pressure, where k is the current time step.[35] The acceleration due to gravity in the direction normal to the surface, g, is approximated by $g = \mu / r^2$. The initial freestream pressure P_0 is obtained from a mesoscale model and has an assumed error of 10% in a 1σ normal sense.

Atmospheric temperature is obtained from the gas equation of state under the ideal gas law assumption:

$$T_\infty = \frac{\mathcal{M} P_\infty}{\mathcal{R}\rho_\infty} \tag{4.12}$$

where $\mathcal{M}$ is the molar mass of the Mars atmosphere, 0.04401 kg/mol (assuming mixed conditions), and $\mathcal{R}$ is the universal gas constant, 8.3144624 J/mol-K.

Two parameters of interest in this analysis that are derived from the atmosphere and IMU are Mach number and dynamic pressure. Mach number is computed using the freestream atmosphere-relative velocity and the ratio of freestream pressure to density (which is essentially normalized freestream temperature):

$$M_\infty = \frac{V_\infty}{\sqrt{\gamma P_\infty / \rho_\infty}} \tag{4.13}$$

where the ratio of specific heats γ is 1.335. As discussed, this Mach number is then used to recover an updated CFD axial force coefficient, and Eqs. (4.9) to (4.13) are re-computed and iterated until Mach number has converged.

Dynamic pressure is computed from the freestream density and velocity, as in Eq. (3.7).

$$q_\infty = \tfrac{1}{2}\rho_\infty V_\infty^2 \tag{4.14}$$

In summary, reconstruction of atmospheric parameters depends on axial accelerations and planet-relative velocity and altitude from the inertial navigation reconstruction. This dependence and the flow of data are illustrated in Figure 4.1.

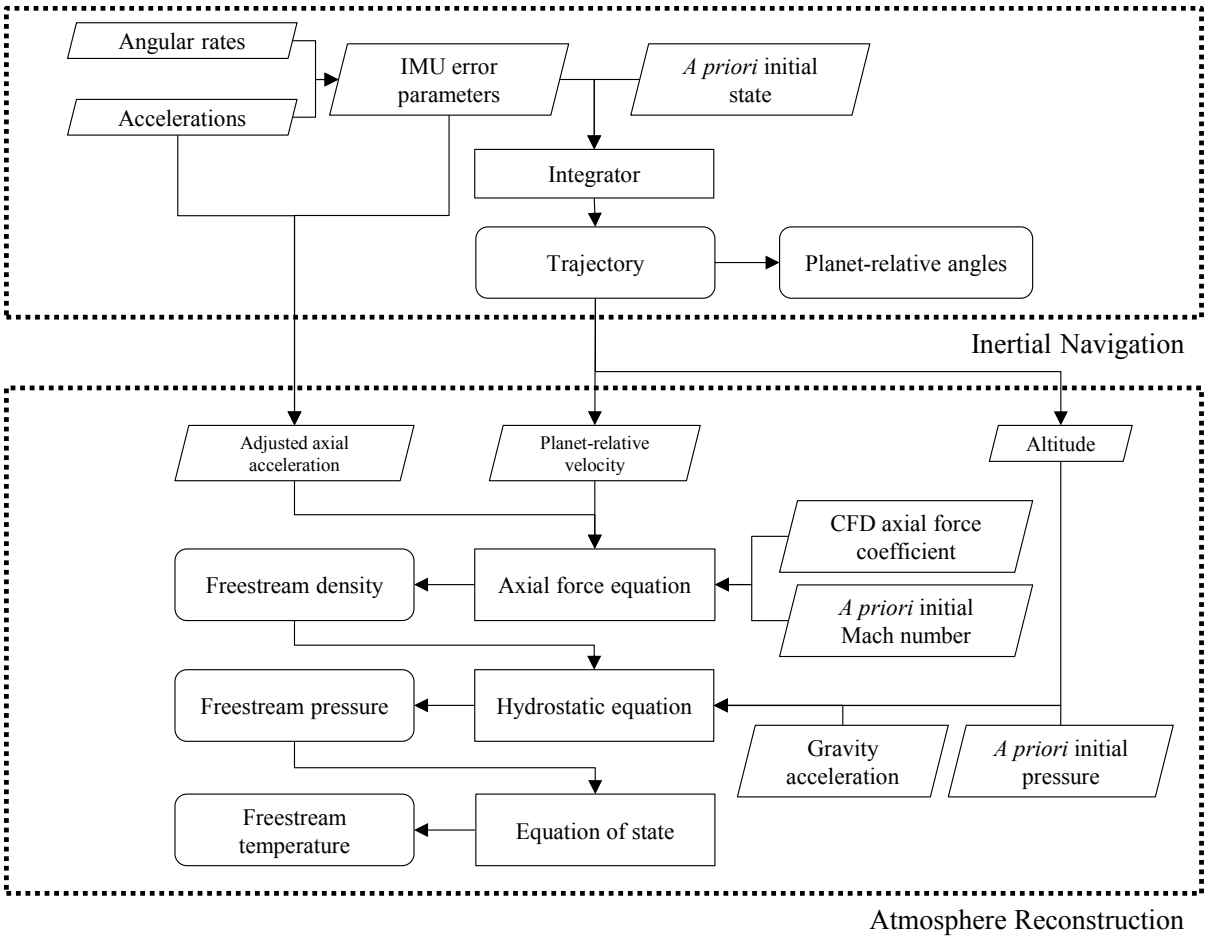

Figure 4.1. Diagram of inertial navigation and atmosphere reconstruction process. Rounded blocks are outputs.

4.1.3 Trajectory Integration Scheme

A numerical three-point predictor-corrector integration scheme by Hamming[56] was implemented by Huh[23] to integrate the IMU data and obtain the vehicle state history. The predictor is described by the equation

$$y_{k+1} = A_0 y_k + A_1 y_{k-1} + A_2 y_{k-2} + \Delta t\left(B_0 \dot{y}_k + B_1 \dot{y}_{k-1} + B_2 \dot{y}_{k-2}\right) \tag{4.15}$$

where k is the current time step, Δt is the change in time between steps, $\dot{y}$ is the time derivative of the function y, and

$$
\begin{aligned}
B_0 &= \tfrac{1}{12}\left(23 + 5A_1 + 4A_2\right) \\
B_1 &= \tfrac{1}{12}\left(-16 + 8A_1 + 16A_2\right) \\
B_2 &= \tfrac{1}{12}\left(5 - A_1 + 4A_2\right)
\end{aligned}
\tag{4.16}
$$

and A_1 and A_2 are arbitrary constants where $A_0 = 1 - A_1 - A_2$. For the present work, $A_1 = -0.5$ and $A_2 = 0.5$.

Each integration step is then updated by the corrector, which is described by the equation

$$
y_{k+1} = a_0 y_k + a_1 y_{k-1} + a_2 y_{k-2} + \tfrac{1}{24}\Delta t\left(b_{-1}\dot{y}_{k+1} + b_0\dot{y}_k + b_1\dot{y}_{k-1} + b_2\dot{y}_{k-2}\right) \tag{4.17}
$$

where

$$
\begin{aligned}
b_{-1} &= 9 - a_1 \\
b_0 &= 19 + 13a_1 + 8a_2 \\
b_1 &= -5 + 13a_1 + 32a_2 \\
b_2 &= 1 - a_1 + 8a_2
\end{aligned}
\tag{4.18}
$$

and a_1 and a_2 are arbitrary constants where $a_0 = 1 - a_1 - a_2$. In the present work, $a_1 = -0.5$ and $a_2 = 0.5$.

4.1.4 MSL Initial Conditions

Integration of the IMU data requires initial conditions for each of the nine state parameters in Eq. (4.3). For EDL operations, the initial position and velocity are obtained from radio tracking and the initial orientation is typically obtained from star tracker mapping. Initial states are generally updated as late as possible before entry. The INSTAR process also requires the corresponding covariance, which supplies the uncertainties associated with the initial conditions and any correlations that may exist between the state variables.

For MSL, the best estimates of the position and velocity components are at $t_0 - 10$ s.[*] The orientation at this time is determined separately by integrating the body rates backwards from t_0, starting with the orientation estimate at t_0 used by the onboard navigation computer. An uncorrelated error of 0.1° in a normal 3σ sense is assumed for each initial Euler angle since flight values are unavailable.[†]

Table 4.1 and Table 4.2 list the initial conditions and the corresponding radio tracking navigation orientation covariance matrix (including the standard deviations from the covariance diagonals) in the Mars-centered Mars mean equator of date t_0 (M) coordinate system. The timing uncertainty is assumed to be negligible, i.e., it is assumed that this state occurs at precisely $t_0 - 10$ s.

---

[*] Martin-Mur, Tomas (2012), personal correspondence of October 8th, MSL Navigation Team Chief, Jet Propulsion Laboratory, Pasadena, CA.

[†] Way, David (2012), personal correspondence of October 18th, Aerospace Engineer, NASA Langley Research Center, Hampton, VA.

Table 4.1. MSL initial state conditions in M frame

Parameter	Units	Value	1σ
t_i	s	-10	---
X_i	m	-8.969338E+04	6.05
Y_i	m	5.080899E+06	6.59
Z_i	m	-9.912496E+04	18.01
$V_{X,i}$	m/s	-3.983226E+03	0.01
$V_{Y,i}$	m/s	-3.685550E+03	0.01
$V_{Z,i}$	m/s	-2.792490E+02	0.01
$\theta_{X,i}$	deg	-156.131612	0.03
$\theta_{Y,i}$	deg	-65.942677	0.03
$\theta_{Z,i}$	deg	-157.699118	0.03

Table 4.2. MSL initial state condition covariance in M frame (position in meters, velocity in meters per second, and orientation in radians).

	X_i	Y_i	Z_i	$V_{X,i}$	$V_{Y,i}$	$V_{Z,i}$	$\theta_{X,i}$	$\theta_{Y,i}$	$\theta_{Z,i}$
X_i	36.63667	-12.9565	65.17529	0.003463	0.00153	-0.01582	0	0	0
Y_i	-12.9567	43.39473	56.56523	0.007566	0.02034	-0.01220	0	0	0
Z_i	65.17529	56.56523	324.3399	-0.00030	0.02778	-0.06416	0	0	0
$V_{X,i}$	0.003463	0.007566	-0.00030	4.62E-05	1.36e-06	2.81E-07	0	0	0
$V_{Y,i}$	0.001549	0.020342	0.027783	1.36E-06	4.97E-05	-6.3E-06	0	0	0
$V_{Z,i}$	-0.01582	-0.01220	-0.06416	2.81E-07	-6.3E-06	6.13E-05	0	0	0
$\theta_{X,i}$	0	0	0	0	0	0	3.38E-7	0	0
$\theta_{Y,i}$	0	0	0	0	0	0	0	3.38E-7	0
$\theta_{Z,i}$	0	0	0	0	0	0	0	0	3.38E-7

The initial conditions and covariance shown in Table 4.1 and Table 4.2 have been transformed from the Earth mean equator and equinox of J2000 frame (EME2000) to the M frame as described in §3.2:

$$\begin{bmatrix} \mathbf{r}_i \\ \mathbf{v}_i \end{bmatrix}^{\mathrm{M}} = \mathrm{C}^{\mathrm{M/EME2000}} \begin{bmatrix} \mathbf{r}_i \\ \mathbf{v}_i \end{bmatrix}^{\mathrm{EME2000}} \tag{4.19}$$

$$\Gamma_{\mathrm{rv}}\left(\mathbf{r}_i^{\mathrm{M}}, \mathbf{v}_i^{\mathrm{M}}\right) = \mathrm{C}^{\mathrm{M/EME2000}} \Gamma_{\mathrm{rv}}\left(\mathbf{r}_i^{\mathrm{EME2000}}, \mathbf{v}_i^{\mathrm{EME2000}}\right) \left[\mathrm{C}^{\mathrm{M/EME2000}}\right]^{\mathrm{T}} \tag{4.20}$$

The quaternions from the MSL navigation computer give the transformation from EME2000 to the descent stage frame. The transformation from the M frame to the descent stage frame is obtained from

$$\mathrm{C}^{\mathrm{DS/M}} = \mathrm{C}^{\mathrm{DS/EME2000}} \left[\mathrm{C}^{\mathrm{M/EME2000}}\right]^{\mathrm{T}} \tag{4.21}$$

where $\mathrm{C}^{\mathrm{DS/EME2000}}$ is the quaternion from the navigation computer transformed to a direction cosine matrix.

The vehicle mass was 3152.5 kg at entry (540 s) and 3144.5 kg at the "straighten up and fly right" maneuver (780 s), or SUFR, when the vehicle ejected ballast masses to shift the center of gravity back to the centerline, making the vehicle ballistic in preparation for chute deploy. The mass is linearly interpolated between these two times. The vehicle mass is assumed to have an error of 16 kg in a 3σ normal sense. The entry vehicle reference area is modeled as a circle of diameter 4.519 m.

4.1.5 MSL Nominal Trajectory and Atmosphere

The method of inertial navigation and atmosphere reconstruction outlined in Figure 4.1 is applied to the as-delivered MSL IMU observations from Figure 2.12 and Figure 2.13 and initial conditions from Table 4.1 to obtain the "nominal" trajectory and atmosphere. As will be discussed in the following section, it is this nominal case that will be randomly dispersed in the INSTAR process using the *a priori* uncertainties provided by JPL in Table 4.2.

The nominal trajectory is shown in the next series of figures. Figure 4.2 shows the position history, Figure 4.3 shows the velocity history, Figure 4.4 shows the quaternion history, Figure 4.5 shows the planet-relative wind angle history, and Figure 4.6 shows the atmosphere profile.

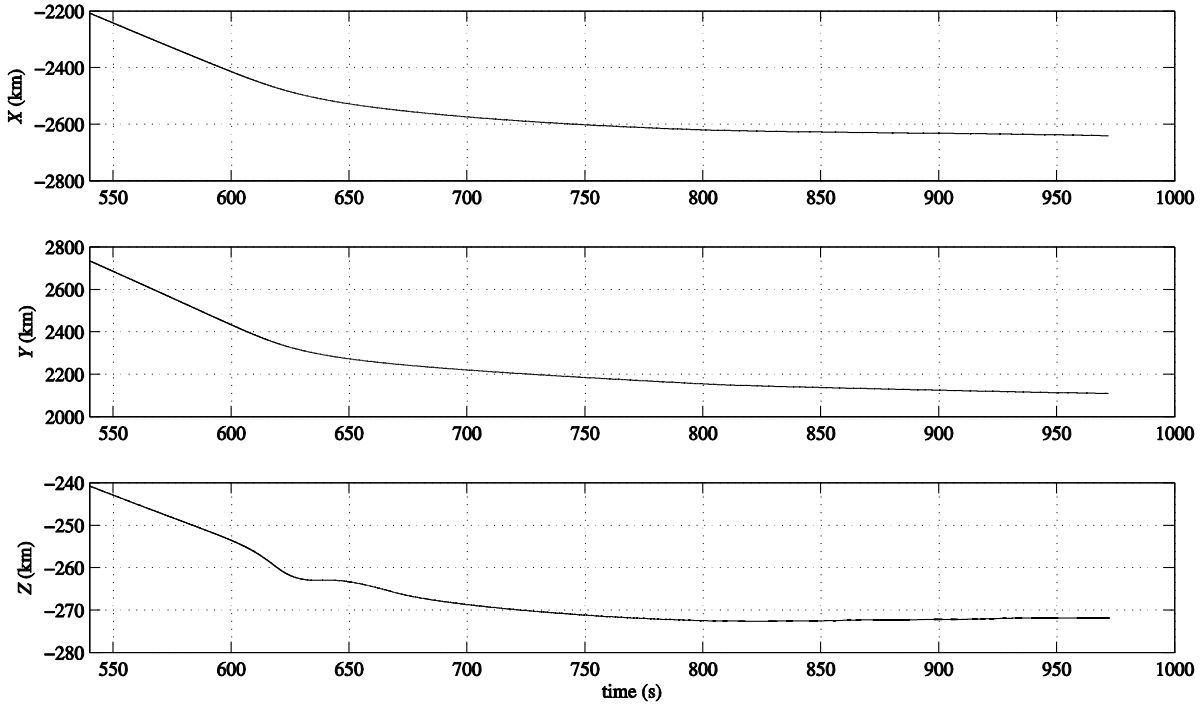

Figure 4.2. Nominal position in M frame from JPL initial conditions.

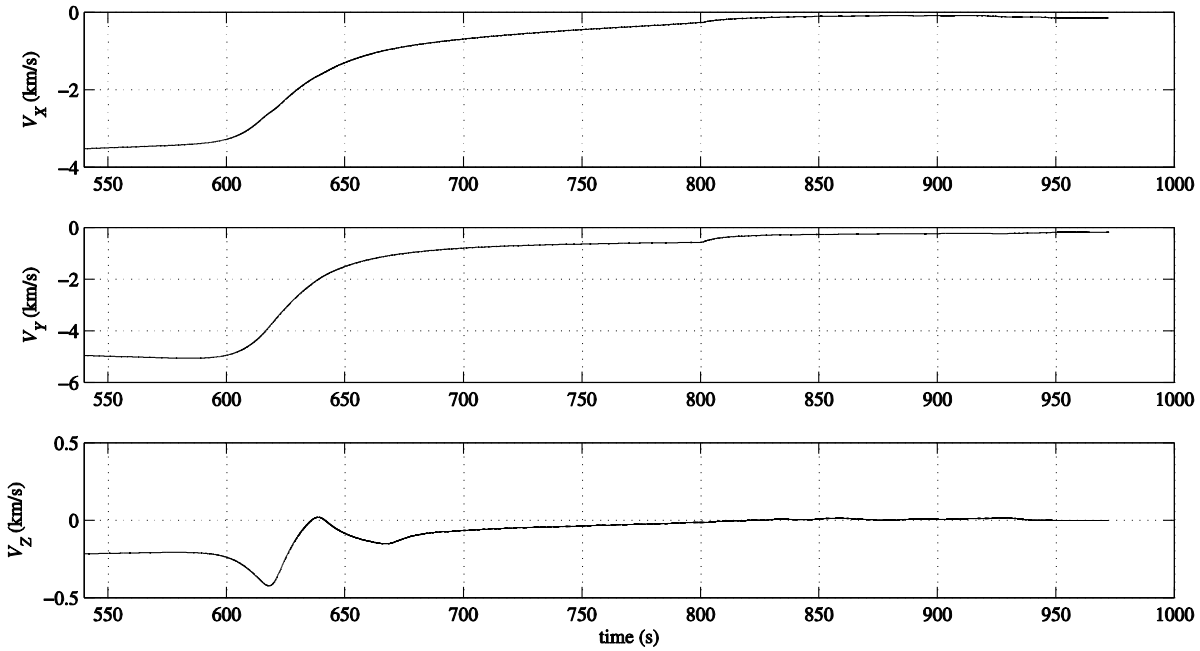

Figure 4.3. Nominal velocity in M frame from JPL initial conditions.

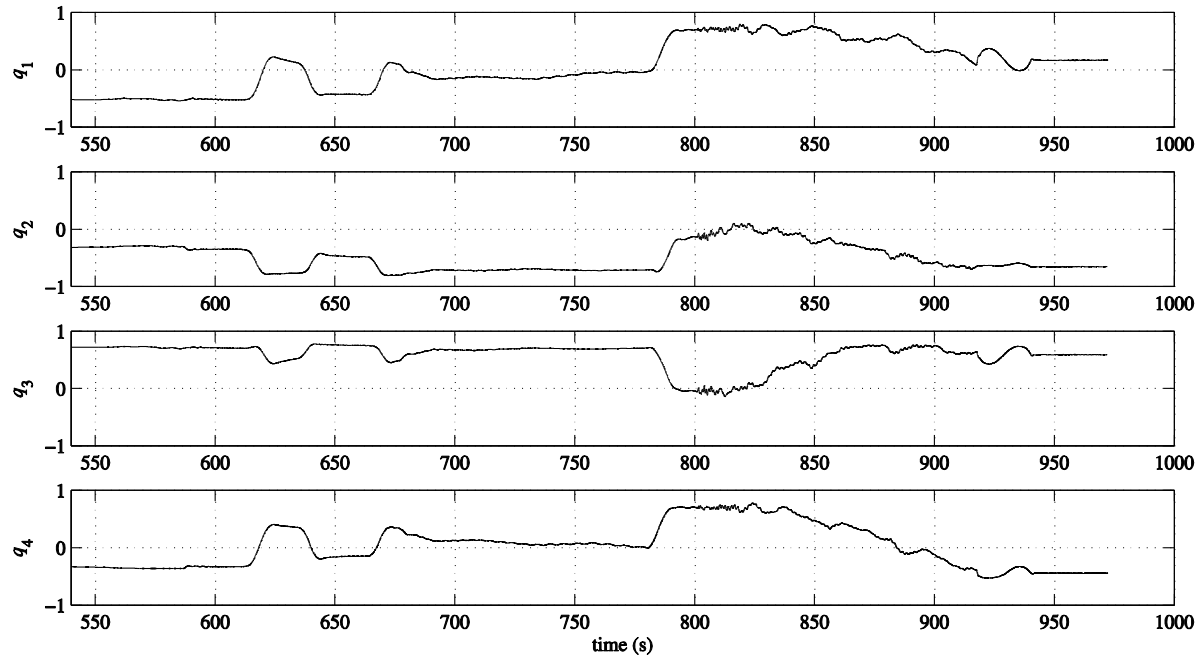

Figure 4.4. Nominal quaternions in M frame from JPL initial conditions.

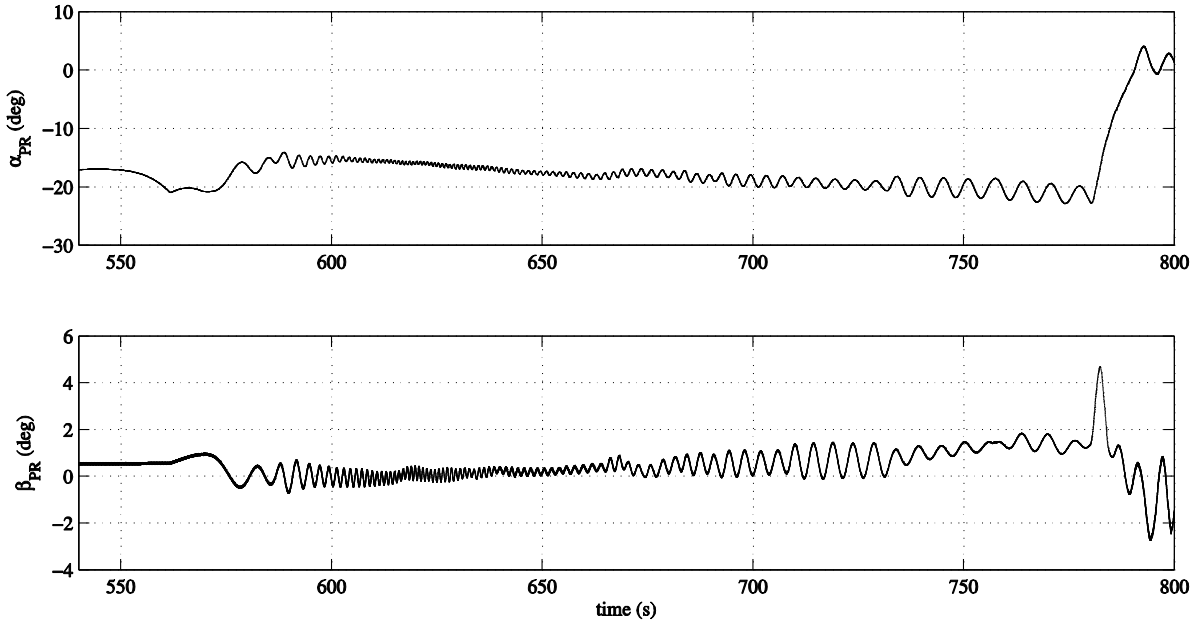

Figure 4.5. Nominal planet-relative wind angles in M frame from JPL initial conditions.

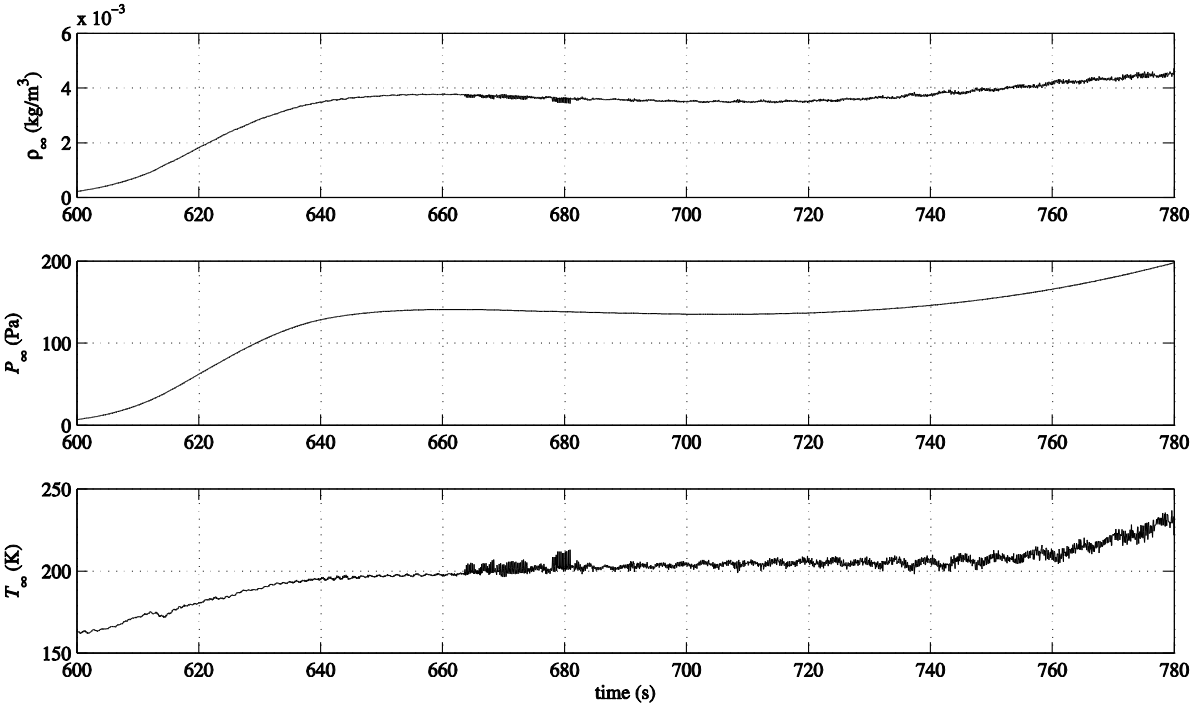

Figure 4.6. Nominal atmosphere from JPL initial conditions.

Table 4.3 lists the differences in the components and vector magnitude between the nominal landing site (i.e., the final computed position) and the reference landing site from Table 2.4. Immediately it may be seen that the computed landing site is nearly a kilometer away from the observed landing site.*

Table 4.3. Comparison of nominal trajectory landing site to reference landing site.

Component	Difference from reference landing site (m)
X	-522.614
Y	502.595
Z	572.713
Magnitude	923.974

It will be shown in the following section that using the INSTAR process with landing site location substantially improves this difference.

4.2 Inertial Navigation Statistical Trajectory and Atmosphere Reconstruction

As previously stated, inertial navigation lacks the advantages of statistical techniques such as Kalman filters in that it cannot utilize redundant data types (pressure, altimetry, etc.), and solution uncertainties cannot be directly computed. To address this issue, a method has been developed[24] that utilizes the inertial navigation approach to trajectory reconstruction as a framework to consider of available redundant observations and generate statistics. The process, called Inertial Navigation Statistical Trajectory and Atmosphere Reconstruction (INSTAR), does not use aerodynamic, control, or noise models, though models such as the hydrostatic equation are used in the classical approach to atmosphere reconstruction. It also requires no assumptions regarding the linearity of the problem. Statistics such as standard deviations and distribution functions are obtained using Monte Carlo dispersion techniques, which are a class of computational algorithms in which simulation parameters are randomized (or dispersed), resulting in a large number of different solutions.[57]

A particular advantage of the INSTAR approach is that it permits arbitrary probability distributions on parameters to be specified or estimated throughout the process. The implications of this flexibility and an analysis of the solutions in the probability space will be discussed in Chapter 5.

* Although this algorithm is nearly identical to that used aboard the MSL entry vehicle, the position during terminal descent and landing was updated in real-time using radar data beginning at 837 s.

It is important to note that Monte Carlo techniques do not provide the "best estimate" per se, but rather provide the probability that a solution may occur. To quote Metropolis and Ulam, "…the estimate will never be confined within given limits of certainty, but only—if the number of trials is great—with great probability."[57]

There are three "types" of trajectories used in the INSTAR process:

- *Reference trajectory*. The trajectory generated using the best estimates of the initial conditions prior to introducing redundant data. In the context of INSTAR, this corresponds to the trajectory generated using the initial conditions provided by the Jet Propulsion Laboratory. The reference trajectory does not change between iterations.
- *Nominal trajectory*. The trajectory and initial conditions that are dispersed using the statistics. For the first iteration, the nominal trajectory is the reference trajectory. For subsequent iterations, this trajectory is updated using mean initial conditions of the valid trajectories from the previous iteration.
- *Dispersed trajectory*. The dispersed trajectories and initial conditions that are generated from the nominal trajectory. The dispersed trajectories that do not satisfy the redundant data are discarded. The remaining trajectories that satisfy the redundant data are then used to generate statistics and the new nominal trajectory for the next iteration.

In the INSTAR process the initial state conditions (position, velocity, and orientation) and IMU error parameters (scale factors, biases, and misalignments) are dispersed in a Monte Carlo sense using uncertainties provided by the mission radio tracking team and the IMU manufacturer. From these dispersed initial conditions, the observed IMU accelerations and angular rates are integrated using inertial navigation to obtain a set of dispersed reconstructed trajectories. Dispersed atmosphere profiles are obtained from the trajectory and an initial atmospheric state. Redundant data are introduced to constrain or "downselect" the dispersed trajectories to those that satisfy the observation uncertainties. For example, the landing site observation may be used to constrain the final position, and any trajectory that terminates outside of the landing site uncertainty sphere is discarded. Updated trajectory and atmosphere statistics are then obtained from this subset of trajectories and atmospheres by computing the standard deviations of the dispersions, and used to begin the next iteration. The process is considered converged when at least 98.5% of the dispersed trajectories are "valid."

A flowchart of the INSTAR process is shown in Figure 4.7. Here, the bolded blocks represent Monte Carlo random dispersions, or solutions resulting from the random dispersions. Note that the dashed box is exactly the classical inertial navigation and atmosphere reconstruction process in Figure 4.1, except for the Monte Carlo random dispersions. The dispersions of the IMU error parameters, initial state, and the CFD axial force coefficients result in dispersed solutions for the state and atmosphere. Statistics are obtained from the solution dispersions in the form of standard deviations and distribution functions. Thus, the INSTAR method enables the inclusion of redundant data types

as well as a statistical approach to estimating parameter uncertainties, but still uses the framework of inertial navigation.

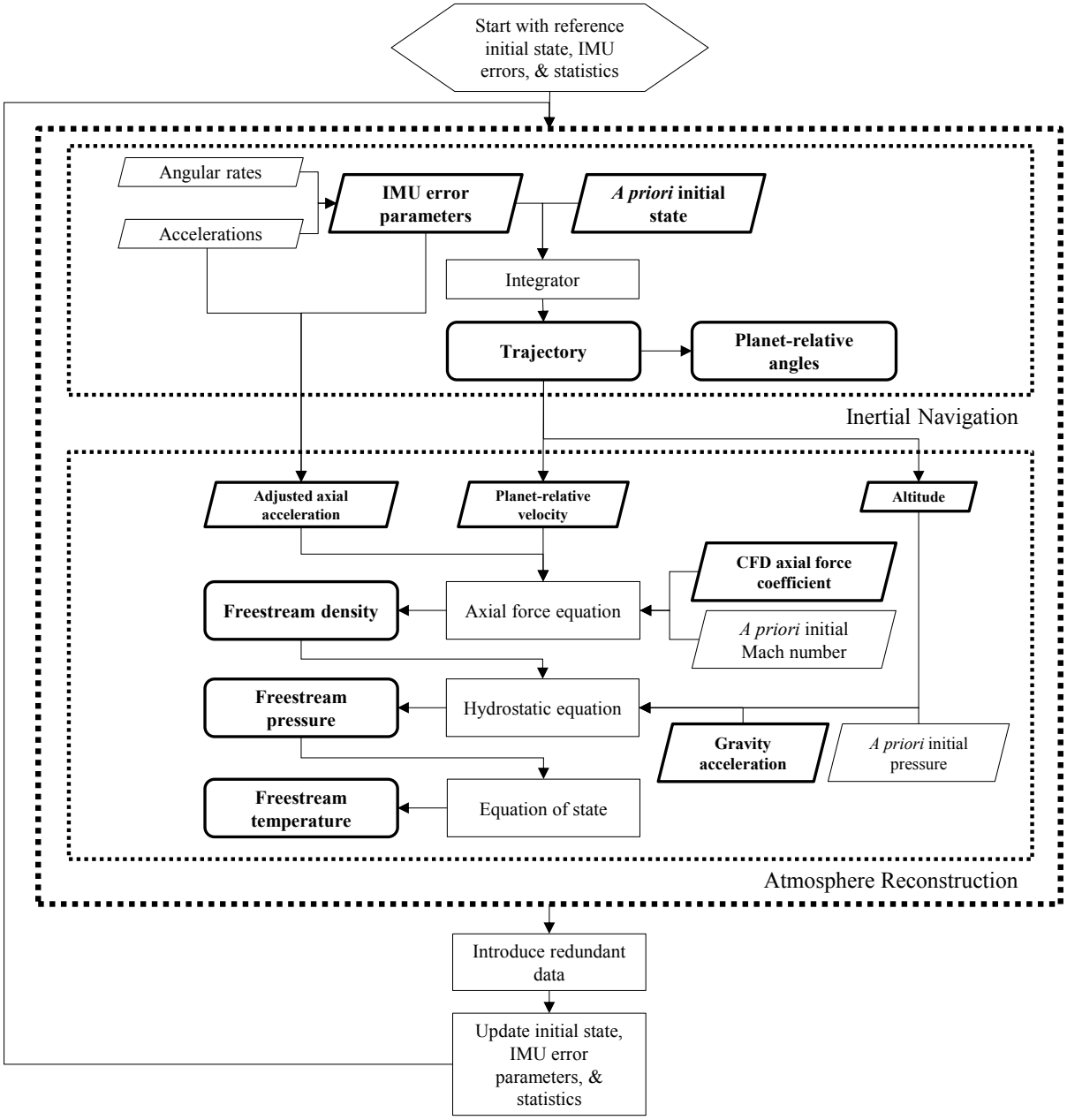

Figure 4.7. Diagram of INSTAR process. Bolded blocks represent Monte Carlo dispersions, rounded blocks are outputs.

The INSTAR process may be summarized in the following steps:

1. Disperse the initial state conditions and IMU error parameters (accelerations and angular rate biases, scale factors, and misalignments) with *a priori* statistics.
2. Integrate IMU data using these initial conditions to obtain a dispersed set of trajectories.
3. Update initial conditions, IMU error parameters, and statistics using the subset of solutions that satisfy the redundant data.
4. Reconstruct atmosphere profiles and statistics from the valid set of trajectories.
5. Iterate steps 1-4 with the updated sets of initial conditions, IMU errors, and statistics until convergence criteria are met.

4.2.1 Trajectory Dispersion and Recovery of Statistics

Dispersion of the nominal trajectory is achieved by utilizing the initial condition covariance. The *a priori* covariance provided by JPL and listed in Table 4.2 is used for the first iteration. For subsequent iterations, this covariance is updated using the valid trajectories, i.e., the trajectories that satisfy the redundant data. This section will describe how trajectories are dispersed using statistics, and how the statistics are recovered from the dispersions.

Let $\mathbf{x}$ be a state vector of length m with mean $\boldsymbol{\mu}_x$ and covariance Γ_x and N be the number of dispersions. If the eigenvectors of Γ_x are arranged in an $[m \times m]$ array V and the eigenvalues are $\mathbf{d}$, then $\boldsymbol{\sigma} = \sqrt{\mathbf{d}}$. Let $\mathbf{y}$ be an $[m \times N]$ array of normally distributed random numbers with mean $\boldsymbol{\mu}_x$ and variance $\boldsymbol{\sigma}^2$, i.e.,

$$\mathbf{y} \sim \mathcal{N}\left(\boldsymbol{\mu}_x, \boldsymbol{\sigma}^2\right) \tag{4.22}$$

The dispersed random state vectors are then

$$\breve{\mathbf{x}} = \mathrm{V}\mathbf{y} \tag{4.23}$$

where the arc embellishment indicates a dispersion and $\breve{\mathbf{x}}$ is an $[m \times N]$ array. Thus, correlations between parameters are considered in the dispersions.

The process of recovering statistics from the dispersed trajectories is more straightforward. The mean set of initial conditions and IMU error parameters $\boldsymbol{\mu}_x$ are computed from the pool of valid trajectories. The differences between the dispersed states and the mean is then computed

$$\mathrm{D} = \breve{\mathbf{x}} - \boldsymbol{\mu}_x \tag{4.24}$$

where $\breve{\mathbf{x}}$ is an $[m \times N]$ array of the random states arranged into N columns, and $\boldsymbol{\mu}_x$ is the mean vector repeated into N columns. The covariance Γ_x is then

$$\Gamma_x = \frac{1}{N}\mathrm{D}^{\mathrm{T}}\mathrm{D} \tag{4.25}$$

Statistics in the form of standard deviations may then be obtained from this covariance (see §3.3).

4.2.2 Hardware and Software Considerations

Using Monte Carlo techniques necessitates careful design of the trajectory generation process so that the time required to generate solutions does not become unmanageable. For example, saving one second per trajectory integration may save over 16 minutes in processing time when integrating 1,000 trajectories, depending on the computer. To achieve a compromise between integration speed and accuracy, the fixed-step three-point predictor-corrector integration method was programmed[23] in Fortran90 and run using a MATLAB® wrapper. Multi-core processing was implemented with OpenMP®, an open-source programming library that interfaces with multiple programming languages, including Fortran.[58]

The primary computer used to compile and execute the INSTAR software for this dissertation was an HP® Z400 Workstation running Microsoft Windows® 7 Service Pack 1 with an Intel® Xeon® W3680 hexa-core CPU clocked at 3.33 GHz. Though integration times vary due to many factors such as operating system loads, 1,000 trajectories may be integrated in approximately two minutes.* Reconstruction of the atmosphere is significantly more time-consuming because the atmosphere reconstruction program does not take advantage of multi-core processing. Table 4.4 lists the approximate times required to run reconstructions with various numbers of Monte Carlo dispersion.

Table 4.4. Approximate times to run various reconstructions.

Number of trajectories	Trajectory reconstruction	Atmosphere reconstruction	MEADS statistical solver
1	0.59 s	10 s	40 s
1,000	2 min (120 s)	45 min (2616 s)	8 hrs
5,000	9 min (533 s)	--	--
10,000	17 min (1042 s)	--	--
50,000	84 min (5016 s)	--	--

With the exception of the inertial navigation integrator, all of the scripts and functions used to implement the techniques and methods in this dissertation were programmed in MathWorks® MATLAB® version 7.5.0.342 (R2007b).

* Writing results to the hard disk is a significant bottleneck when dealing with thousands of trajectories, each with solution profiles that must be saved in ASCII plain text. Improvements in write times may be improved by using a solid state drive, but for this application, only the first and final values (initial time and time at landing) were saved.

4.2.3 Landing Site in INSTAR

The INSTAR process outlined in the preceding sections is applied to the MSL EDL sequence using the observed landing site as the redundant data type. For this analysis, the nine initial conditions and fifteen IMU errors are dispersed in a Monte Carlo sense for a total of 50,000 dispersed trajectories. For this analysis a normal distribution is assumed for the initial condition dispersions and a uniform distribution is assumed for the landing site, although the flexibility of INSTAR permits any form of distribution function.

The landing site dispersions relative to the reference landing site are shown in Figure 4.8 in the landing site measurement space (East longitude, areocentric latitude, and radius) but are computed in the non-inertial Mars-centered Mars-fixed (MCMF) frame. The final computed position (denoted by the subscript *f*), which is described in the Mars-centered Mars mean equator and prime meridian of t_0 frame, is converted to the MCMF frame by

$$\mathbf{r}_f^{\mathrm{MCMF}} = \mathrm{C}^{\mathrm{MCMF/M}}\mathbf{r}_f^{\mathrm{M}} \tag{4.26}$$

where the direction cosine matrix $\mathrm{C}^{\mathrm{MCMF/M}}$ describes a positive rotation about the planetary spin axis[59]

$$\mathrm{C}^{\mathrm{MCMF/M}} = \begin{bmatrix} \cos\theta & \sin\theta & 0 \\ -\sin\theta & \cos\theta & 0 \\ 0 & 0 & 1 \end{bmatrix} \tag{4.27}$$

and the angle θ is the amount the planet has rotated during the time that has elapsed between t_0 and the landing time (972 s), or $\theta = \Omega t$. Thus, both precession and nutation is neglected for this transformation. Though not used to constrain the solutions, the vehicle velocity in the MCMF frame may be computed as[59]

$$\mathbf{v}^{\mathrm{MCMF}} = \mathbf{v}^{\mathrm{M}} - \boldsymbol{\Omega} \times \mathbf{r}^{\mathrm{M}} \tag{4.28}$$

where $\boldsymbol{\Omega} = [0, 0, \Omega]^{\mathrm{T}}$ and $\Omega = 7.088212079 \times 10^{-5}$ rad/s is the Mars rotation rate.

The landing site measurement is converted to the same MCMF frame by

$$\begin{aligned} X_{f,\mathrm{ref}} &= r_{f,\mathrm{ref}} \cos\delta_{f,\mathrm{ref}} \cos\lambda_{f,\mathrm{ref}} \\ Y_{f,\mathrm{ref}} &= r_{f,\mathrm{ref}} \cos\delta_{f,\mathrm{ref}} \sin\lambda_{f,\mathrm{ref}} \\ Z_{f,\mathrm{ref}} &= r_{f,\mathrm{ref}} \sin\delta_{f,\mathrm{ref}} \end{aligned} \tag{4.29}$$

where the declination δ and the longitude λ are from Table 2.4. The differences are then

$$\begin{aligned} \Delta X &= X - X_{f,\mathrm{ref}} \\ \Delta Y &= Y - Y_{f,\mathrm{ref}} \\ \Delta Z &= Z - Z_{f,\mathrm{ref}} \end{aligned} \tag{4.30}$$

Note that the landing site location differences use the convention computed–reference (where the reference site is from Table 2.4), so that the reference landing site location is subtracted from the

dispersed locations. Thus, a negative radius difference means that a dispersed landing site is physically below the reference landing site.

The computed landing site is converted to the MCMF measurement space in polar coordinates by first computing the longitude

$$\lambda = \alpha - \Omega t \tag{4.31}$$

where the right ascension α is $\alpha = \tan^{-1} Y^{\mathrm{M}} / X^{\mathrm{M}}$ and Ωt describes the location of the prime meridian. The radius is unchanged. The latitude is then

$$\delta = \tan^{-1} \frac{Z^{\mathrm{M}}}{\sqrt{\left[X^{\mathrm{M}}\right]^2 \left[Y^{\mathrm{M}}\right]^2}} \tag{4.32}$$

In Figure 4.8, the nominal landing site is from the trajectory with no dispersed initial conditions or IMU errors, that is, the landing site corresponding to the trajectory obtained from the initial conditions in Table 4.1. In subsequent INSTAR iterations, this "nominal" trajectory is updated by replacing these initial conditions with the mean initial conditions and IMU errors obtained from the valid trajectories.

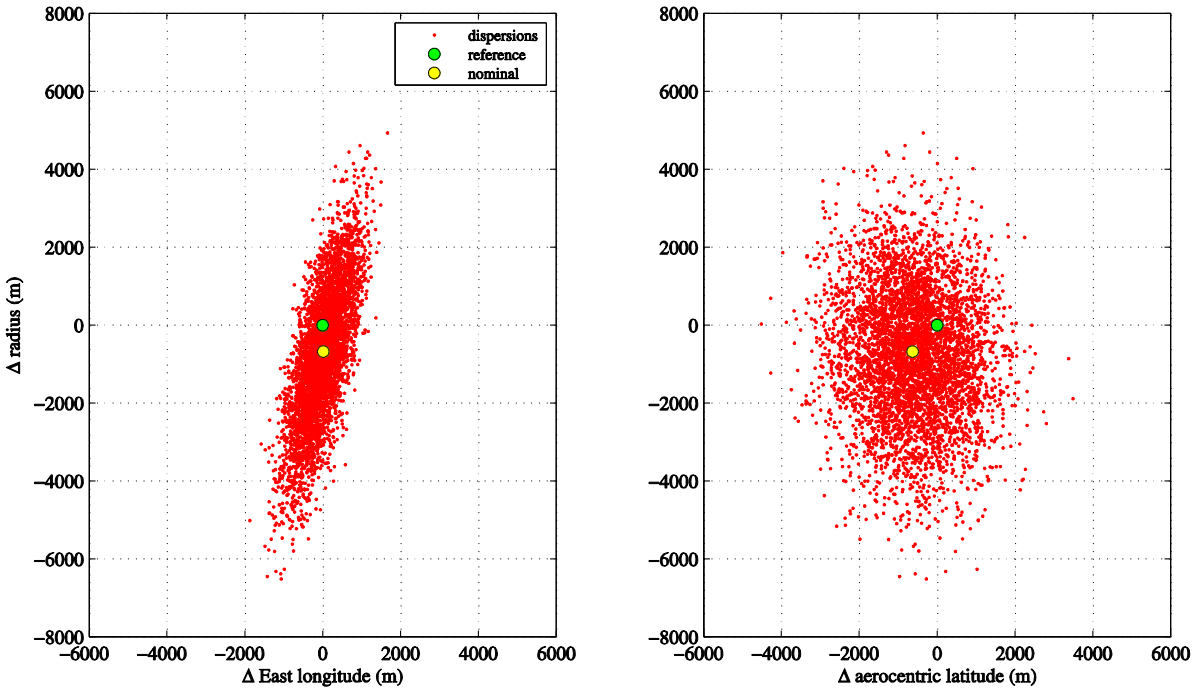

Figure 4.8. Dispersed landing sites, first iteration, 50,000 cases, MCMF of landing time frame.

The process described here is nearly identical to that in Ref. 24, but all IMU errors are dispersed, rather than just acceleration biases as in that study. The result is that the dispersions for this first iteration are much more "spread out" across the landing site space. The spread in radius is between -7,000 m and +5,000 m, the spread in East longitude is approximately ±2,000 m, and the spread in areocentric latitude is between -7,000 m and +5,000 m. The high correlation between radius and longitude is governed primarily by the entry flight path angle. The distance from the nominal landing site to the reference landing site is approximately 924 m (see Table 4.3). The difference computed by the MSL navigation computer was smaller in radius because altimetry data was used to update the position and velocity in real-time during terminal descent.

The INSTAR process is continued by selecting those trajectories that satisfy the observation of the reference landing site uncertainty of 150 m. Assuming a uniform distribution in the landing site space, any trajectories that lie within a sphere centered at the landing site with radius 150 m are candidates.

There are 38 trajectories that fall within this sphere of uncertainty. Therefore, of the 50,000 trajectory cases, 38 are used for the calculation of the statistics. Increasing the initial sample size would aid in populating the candidate samples and provide a better estimation of the statistics, but the current sample is sufficient. The mean of the initial conditions and IMU errors of those trajectories that fall within the sphere become the initial conditions (or "new" nominal) for the next iteration, and the computed standard deviations from these dispersions result in a new covariance with which to disperse the new initial conditions and IMU errors. These updated initial conditions and covariance associated with the new updated initial conditions are used to repeat the INSTAR process until convergence of the percentage of valid cases (selected to be 98.5%). Subsequent iterations use 1,000 trajectories to save processing time in atmosphere and MEADS reconstructions. Convergence was achieved in six iterations.

Figure 4.9 shows the 1,000 new dispersed trajectories for this final INSTAR iteration. Immediately, the significantly smaller distribution space is evident. The landing sites are now spread across only 200 meters in any direction from the reference landing site. From the valid trajectories, initial conditions have been determined such that integrating the acceleration and rate measurements provide a close hit (within ten meters) with the reference landing site. In addition, the covariance is available at any time along the trajectory.

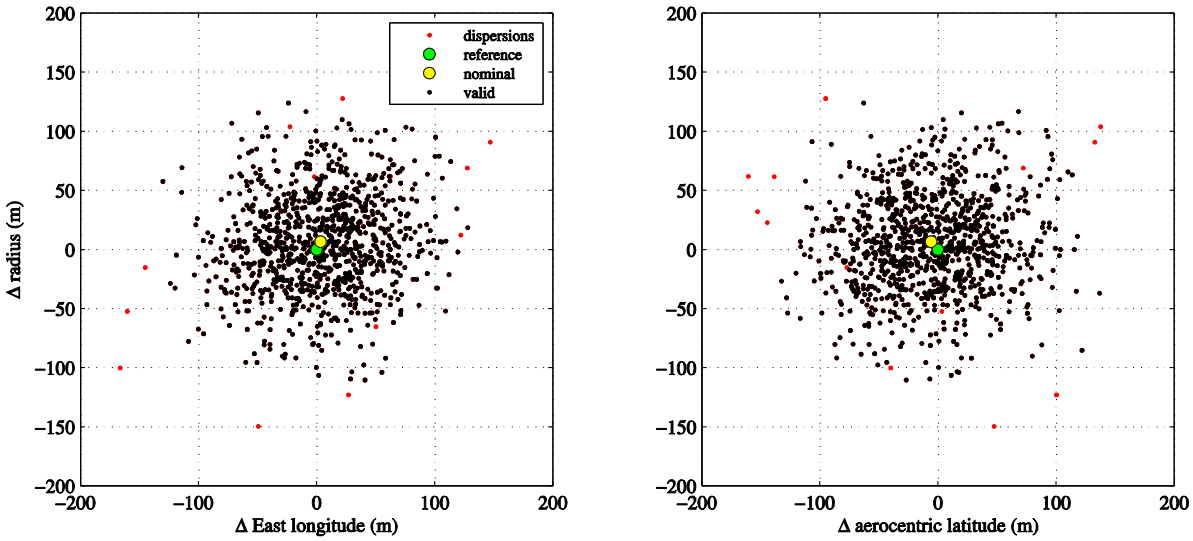

Figure 4.9. Landing site dispersions, end of final iteration, MCMF of landing time frame.

Atmosphere reconstructions as described in §4.1.2 are carried out using the valid trajectories from the final iteration. Uncertainties are obtained from the standard deviations of the dispersions along the trajectories.

Table 4.5. Convergence history of INSTAR process.

Iteration	No. of Trajectories	No. of valid trajectories	Percentage of valid trajectories	Mean distance to reference landing site (m)
0	50,000	38	0.08%	923.974
1	1,000	822	82.20%	18.156
2	1,000	935	93.50%	13.230
3	1,000	948	94.80%	11.609
4	1,000	971	97.10%	10.409
5	1,000	978	97.80%	10.213
6	1,000	985	98.50%	9.371

Finally, it is informative to examine the convergence history of the INSTAR process. Table 4.5 lists the numerical values for the number of valid trajectories, as well as the mean distance to the landing site for each INSTAR iteration. The marked improvement between the zeroth and first iterations is apparent, as the landing site difference has decreased from 924 m to 18 m.

4.3 Flush Air Data System Parameter Estimation

FADS-based reconstruction methods utilize pressure measurements combined with CFD pressures, wind tunnel data, and/or Newtonian flow approximations to estimate aerodynamic and atmospheric parameters and associated uncertainties. As discussed in §3.1, the measured pressure at a FADS port is a function of the flow field relative to the vehicle and the port location (defined by cone angle η_i and clock angle ζ_i):

$$P_i = f\left(P_\infty, q_\infty, M_\infty, \alpha, \beta, \gamma : \eta_i, \zeta_i\right) \tag{4.33}$$

and any two variables from the set $[P_t, P_\infty, q_\infty, M_\infty]$ in addition to α and β may be determined simultaneously.* In the present work, the estimated parameters will be angle of attack, angle of sideslip, dynamic pressure, and freestream pressure. The estimates of these parameters are obtained by converging on the values that minimize the residuals between the observed and model pressures in a sequential manner, which may be thought of as attempting to fit a point in the parameter space to the observed pressures at a given time. The most common methods of minimizing these residuals use formulations of the least squares techniques described in §3.4.[25,26,31]

The four variables to be estimated, being functions of pressure, change at every time step and are described as *local parameters*. Local parameters are sequentially estimated in the "inner" loop. Pressure transducer biases, scale factors, and nonlinear terms apply to the entire dataset and are described as *global parameters*. Global parameters are batch-estimated using the same minimum variance estimator by processing all of the observations simultaneously in an "outer" loop, after the local parameters have been estimated. This process, illustrated in Figure 4.10, is repeated until convergence.

The global parameters are described by the pressure model for the *i*th transducer:

$$\bar{P}_i = a_i + b_i P_{i,\mathrm{CFD}} + c_i P_{i,\mathrm{CFD}}^2 \tag{4.34}$$

where P_{CFD} is the pressure recovered from the CFD database, *a* is the bias, *b* is the scale factor, and *c* is the nonlinear term.

Note that the only CFD models used in the MEADS algorithm are those for surface pressure coefficients. The dynamic pressure estimate is determined primarily by the pressure at the port nearest to the stagnation point (port 2, see Figure 2.9), a region that is well-characterized by CFD. Thus, the MEADS dynamic pressure estimate is essentially independent of the surface pressure coefficient distribution and associated uncertainty (wind angle estimates are more dependent on the distribution as they are determined by the destruction of the pressures across several different ports). As will be discussed in Chapter 5, the independence of the MEADS dynamic pressure estimates from the surface

* Recall from §3.1.2 the assumptions made in this formulation: the flow is high-speed, compressible, steady, and adiabatic, and gravitational forces are neglected.[25]

pressure distribution will be leveraged to obtain atmospheric parameter estimates that do not rely on the CFD axial force coefficients.

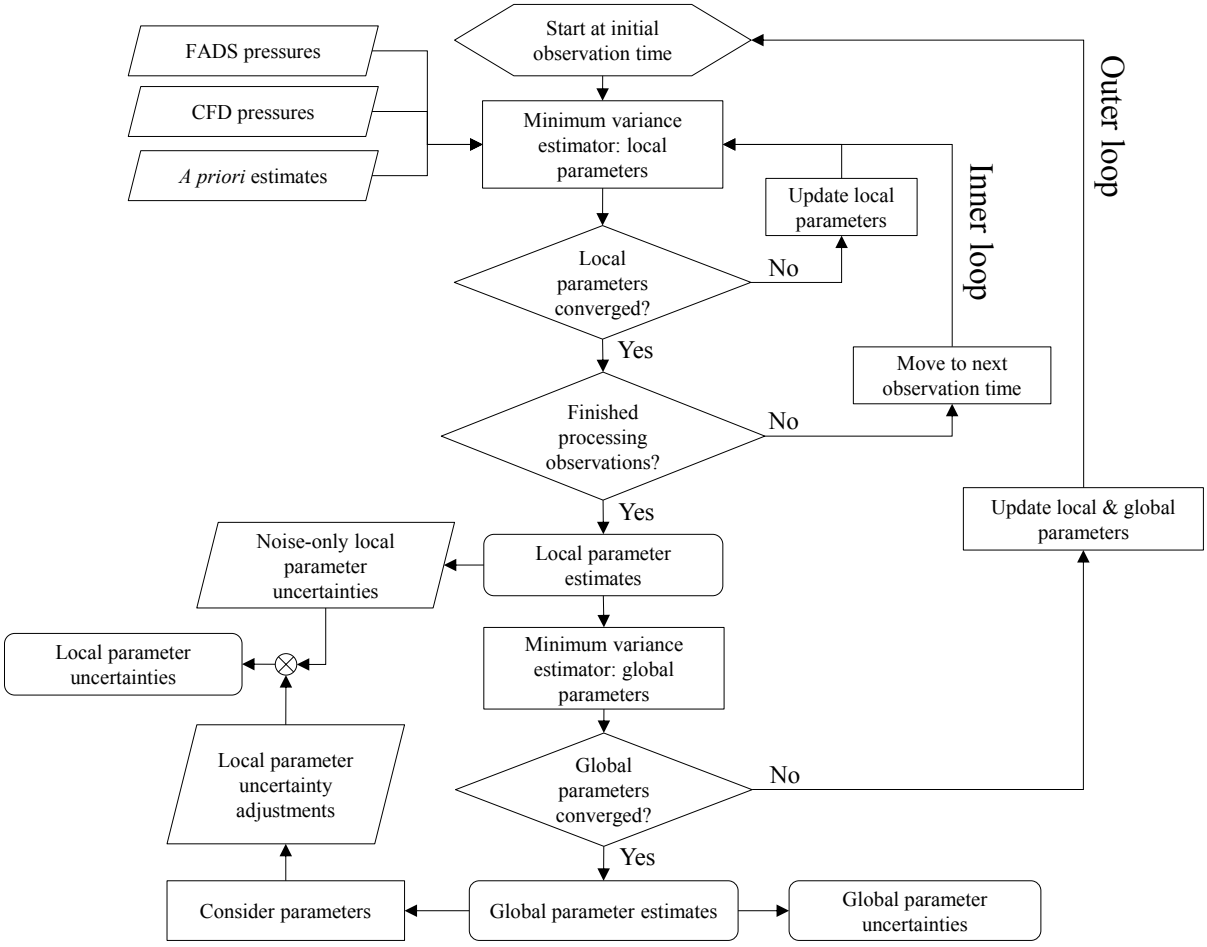

Figure 4.10. Diagram of FADS-based parameter estimation process. Rounded blocks are outputs.

4.3.1 MEADS Minimum Variance Estimation Algorithm

The selected estimation technique in the present analysis is minimum variance with *a priori* and differential correction,[20] which has been demonstrated to be an effective method for obtaining state estimates and statistics from FADS observations.[28] Let **x** be the state vector of local parameters, **y** be the measurement vector, **z** be the unknown state vector of global parameters (transducer errors), and $\boldsymbol{\varepsilon}$ be the measurement noise, such that

$$\mathbf{x} = [\alpha, \beta, q_\infty, P_\infty]^{\mathrm{T}} \tag{4.35}$$

$$\mathbf{z} = [a_1, ..., a_7, b_1, ..., b_7, c_1, ..., c_7]^{\mathrm{T}} \tag{4.36}$$

where $[a_1, ..., a_7]^{\mathrm{T}}$ are the biases, $[b_1, ..., b_7]^{\mathrm{T}}$ are the scale factors, and $[c_1, ..., c_7]^{\mathrm{T}}$ are the nonlinear terms for each of the seven transducers, for a total of 21 global parameters. The linearized equations relating the observations to the parameters are therefore

$$\mathbf{y} = \mathrm{A}\mathbf{x} + \mathrm{B}\mathbf{z} + \boldsymbol{\varepsilon} \tag{4.37}$$

where A is the matrix of sensitivities of the local parameters to the measurements and B is the matrix of sensitivities of the global parameters to the measurements. It is assumed that $\mathbf{z}$ is a random vector with $E(\mathbf{z}) = 0$ (i.e., mean zero) and covariance $\mathrm{cov}(\mathbf{z}) = \Gamma_z$. It is also assumed that $E(\boldsymbol{\varepsilon}) = 0$, $\mathrm{cov}(\boldsymbol{\varepsilon}) = \Gamma_\varepsilon$, and $E(\mathbf{z}\boldsymbol{\varepsilon}^{\mathrm{T}}) = 0$. The unbiased minimum variance estimator with differential correction and *a priori* for the local parameters is then simply Eq. (3.87), or

$$\Delta\hat{\mathbf{x}}_k = \left(\mathrm{A}^{\mathrm{T}}\Gamma_\varepsilon^{-1}\mathrm{A} + \Gamma_\mu^{-1}\right)^{-1}\left(\mathrm{A}^{\mathrm{T}}\Gamma_\varepsilon^{-1}\Delta\tilde{\mathbf{y}} + \Gamma_\mu^{-1}\left(\boldsymbol{\mu} - \hat{\mathbf{x}}_k\right)\right) \tag{4.38}$$

where Γ_ε is the measurement covariance, Γ_μ is the covariance associated with the *a priori* state estimates $\boldsymbol{\mu}$, $\Delta\mathbf{y}$ is the vector of the differences between observed and computed data, and $\hat{\mathbf{x}}_{k+1} = \hat{\mathbf{x}}_k + \Delta\hat{\mathbf{x}}_k$ provides the state estimation update.

Consider now the covariance matrix for Eq. (4.37),

$$\Gamma_{\hat{\mathrm{x}}} = \left(\mathrm{A}^{\mathrm{T}}\Gamma_\varepsilon^{-1}\mathrm{A} + \Gamma_\mu^{-1}\right)^{-1} + \left(\mathrm{A}^{\mathrm{T}}\Gamma_\varepsilon^{-1}\mathrm{A} + \Gamma_\mu^{-1}\right)^{-1}\mathrm{A}^{\mathrm{T}}\Gamma_\varepsilon^{-1}\mathrm{B}\Gamma_{\mu_{\hat{z}}}\mathrm{B}^{\mathrm{T}}\Gamma_\varepsilon^{-1}\mathrm{A}\left(\mathrm{A}^{\mathrm{T}}\Gamma_\varepsilon^{-1}\mathrm{A} + \Gamma_\mu^{-1}\right)^{-1} \tag{4.39}$$

where the matrix B is the sensitivity of the global parameters to the pressure measurements and $\Gamma_{\mu_{\hat{z}}}$ is the *a priori* global parameter covariance. A close examination of Eq. (4.39) shows that the first term is simply the covariance matrix for the standard $\mathbf{y} = \mathrm{A}\mathbf{x} + \boldsymbol{\varepsilon}$ model, i.e., Eq. (3.84). This covariance provides a statistical measure of how well the local parameter estimates fit the data but does not take into account the accuracy of the global parameter estimates. The second term in Eq. (4.39) adjusts this covariance by considering the effects of the transducer errors $\mathbf{z}$ and including them as random biases. This adjustment to the covariance is referred to as the "consider parameters" approach.[60]

The minimum variance estimator for the global parameters is

$$\Delta\hat{\mathbf{z}}_k = \left(\mathrm{B}^{\mathrm{T}}\Gamma_\varepsilon^{-1}\mathrm{B} + \Gamma_{\mu_{\hat{z}}}^{-1}\right)^{-1}\left(\mathrm{B}^{\mathrm{T}}\Gamma_\varepsilon^{-1}\Delta\tilde{\mathbf{y}} + \Gamma_{\mu_{\hat{z}}}^{-1}\left(\boldsymbol{\mu}_{\hat{z}} - \hat{\mathbf{z}}_k\right)\right) \tag{4.40}$$

and the global parameter covariance is simply the inverse term of Eq. (4.40),

$$\Gamma_{\hat{z}} = \left(\mathrm{B}^{\mathrm{T}}\Gamma_\varepsilon^{-1}\mathrm{B} + \Gamma_{\mu_{\hat{z}}}^{-1}\right)^{-1} \tag{4.41}$$

4.3.2 Dimensional Analysis

If there are n discrete pressure observations per transducer, a dimensional analysis of the local parameter estimator defined by Eq. (4.38) yields

$$\overset{[4\times1]}{\Delta\hat{\mathbf{x}}_k} = \left(\overset{[4\times7][7\times7][7\times4]}{\mathrm{A}^{\mathrm{T}}\ \Gamma_{\varepsilon}^{-1}\ \mathrm{A}} \overset{[4\times4]}{+\Gamma_{\mu}^{-1}} \right)^{-1} \left(\overset{[4\times7][7\times7]\ [7\times1]}{\mathrm{A}^{\mathrm{T}}\ \Gamma_{\varepsilon}^{-1}\ \Delta\tilde{\mathbf{y}}} \overset{[4\times4]}{+\Gamma_{\mu}^{-1}} \left(\overset{[4\times1]\quad[4\times1]}{\boldsymbol{\mu} - \hat{\mathbf{x}}_k} \right) \right) \tag{4.42}$$

where $k = 1..n$ and the sensitivity matrix is

$$\mathrm{A} = \begin{bmatrix} \dfrac{\partial P_{1,k}}{\partial \alpha} & \dfrac{\partial P_{1,k}}{\partial \beta} & \dfrac{\partial P_{1,k}}{\partial q_{\infty}} & \dfrac{\partial P_{1,k}}{\partial P_{\infty}} \\ \vdots & \vdots & \vdots & \vdots \\ \dfrac{\partial P_{7,k}}{\partial \alpha} & \dfrac{\partial P_{7,k}}{\partial \beta} & \dfrac{\partial P_{7,k}}{\partial q} & \dfrac{\partial P_{7,k}}{\partial P_{\infty}} \end{bmatrix} \tag{4.43}$$

the measurement noise and *a priori* local parameter covariances are

$$\mathrm{diag}\left(\Gamma_{\varepsilon}\right) = \left[\sigma_{\tilde{P}_{1,k}}^2, ..., \sigma_{\tilde{P}_{7,k}}^2 \right]^{\mathrm{T}} \tag{4.44}$$

$$\mathrm{diag}\left(\Gamma_{\mu}\right) = \left[\sigma_{\mu_{\alpha}}^2, \sigma_{\mu_{\beta}}^2, \sigma_{\mu_{q_{\infty}}}^2, \sigma_{\mu_{P_{\infty}}}^2 \right]^{\mathrm{T}} \tag{4.45}$$

and the observation vector contains the differences between the observed and model pressures,

$$\Delta\tilde{\mathbf{y}} = \begin{bmatrix} \tilde{P}_{1,k} - \bar{P}_{1,k} \\ \vdots \\ \tilde{P}_{7,k} - \bar{P}_{7,k} \end{bmatrix} \tag{4.46}$$

The off-diagonal terms for the measurement noise and *a priori* local parameter covariances are zero, i.e., they are assumed to be uncorrelated.

A dimensional analysis of the global parameter estimator defined by Eq. (4.40) yields

$$\overset{[21\times1]}{\Delta\hat{\mathbf{z}}_j} = \left(\overset{[21\times7n][7n\times7n][7n\times21]}{\mathrm{B}^{\mathrm{T}}\ \ \Gamma_{\varepsilon}^{-1}\ \ \mathrm{B}} \overset{[21\times21]}{+\Gamma_{\mu_{\hat{z}}}^{-1}} \right)^{-1} \left(\overset{[21\times7n][7n\times7n]\ [7n\times1]}{\mathrm{B}^{\mathrm{T}}\ \ \Gamma_{\varepsilon}^{-1}\ \ \Delta\tilde{\mathbf{y}}} \overset{[21\times1]}{+\Gamma_{\mu_{\hat{z}}}^{-1}} \left(\overset{[21\times1]\quad[21\times1]}{\boldsymbol{\mu}_{\hat{z}} - \hat{\mathbf{z}}_j} \right) \right) \tag{4.47}$$

where $j = 1..m$ global iterations. The sensitivity matrix B is composed of n $[7\times21]$ matrices arranged into a $[7n\times21]$ matrix:

$$\mathrm{B}=\left[\begin{array}{ccc|ccc|ccc}
\frac{\partial P_{1,1}}{\partial a_1} & \cdots & \frac{\partial P_{1,1}}{\partial a_7} & \frac{\partial P_{1,1}}{\partial b_1} & \cdots & \frac{\partial P_{1,1}}{\partial b_1} & \frac{\partial P_{1,1}}{\partial c_1} & \cdots & \frac{\partial P_{1,1}}{\partial c_7} \\
\vdots & \ddots & \vdots & \vdots & \ddots & \vdots & \vdots & \ddots & \vdots \\
\frac{\partial P_{7,1}}{\partial a_1} & \cdots & \frac{\partial P_{7,1}}{\partial a_7} & \frac{\partial P_{7,1}}{\partial b_1} & \cdots & \frac{\partial P_{7,1}}{\partial b_7} & \frac{\partial P_{7,1}}{\partial c_1} & \cdots & \frac{\partial P_{7,1}}{\partial c_7} \\
\hline
 & \vdots & & & \vdots & & & \vdots & \\
\hline
\frac{\partial P_{1,n}}{\partial a_1} & \cdots & \frac{\partial P_{1,n}}{\partial a_7} & \frac{\partial P_{1,n}}{\partial b_1} & \cdots & \frac{\partial P_{1,n}}{\partial b_1} & \frac{\partial P_{1,n}}{\partial c_1} & \cdots & \frac{\partial P_{1,n}}{\partial c_7} \\
\vdots & \ddots & \vdots & \vdots & \ddots & \vdots & \vdots & \ddots & \vdots \\
\frac{\partial P_{7,n}}{\partial a_1} & \cdots & \frac{\partial P_{7,n}}{\partial a_7} & \frac{\partial P_{7,n}}{\partial b_1} & \cdots & \frac{\partial P_{7,n}}{\partial b_7} & \frac{\partial P_{7,n}}{\partial c_1} & \cdots & \frac{\partial P_{7,n}}{\partial c_7}
\end{array}\right] \tag{4.48}$$

The partials in B may be written explicitly from the pressure model in Eq. (4.34) :

$$\frac{\partial P}{\partial a}=1 \quad \frac{\partial P}{\partial b}=P \quad \frac{\partial P}{\partial c}=P^2 \tag{4.49}$$

The *a priori* global parameter covariance is diagonal (i.e., uncorrelated):

$$\mathrm{diag}\left(\Gamma_{\mu_{\hat{z}}}\right)=\left[\sigma_{a_1}^2,...,\sigma_{a_7}^2,\sigma_{b_1}^2,...,\sigma_{b_7}^2,\sigma_{c_1}^2,...,\sigma_{c_7}^2\right]^{\mathrm{T}} \tag{4.50}$$

The observation vector $\Delta\tilde{\mathbf{y}}$ is the $[n\times 1]$ observation vector from Eq. (4.46) replicated into a $[7n\times 1]$ vector, and the measurement covariance Γ_ε is the diagonal of each of the kth covariances from Eq. (4.44) arranged into the diagonals of a $[7n\times 7n]$ array. Thus, solving for the global parameters is a batch process since all of the observations are processed simultaneously.

4.3.3 Initial Conditions and Parameter Observability

Table 4.6 lists the *a priori* initial conditions and statistics assumed for the local parameters **x** and global parameters **z**. The local parameter initial conditions are obtained from the inertial navigation and atmosphere reconstruction solutions at 600 s.

Of particular note in Table 4.6 is the static pressure *a priori* uncertainty, 1.0E-6 Pa. This very tight restriction effectively prevents the static pressure estimate from diverging from its *a priori* estimate that is obtained from integration of the hydrostatic equation, that is, $P_{\infty,\mathrm{MEADS}}=P_{\infty,\mathrm{IMU}}$.* In contrast, the *a priori* uncertainties of the other parameters are relatively loose and permit these estimates to "float" as necessary to minimize the pressure residuals.

* This convenient assumption is indirectly supported by the MEADS-derived solution presented in Ref. 32, which shows that the freestream pressure from the MEADS algorithm is within 0.02% of the hydrostatic freestream pressure from the inertial navigation reconstruction.

Table 4.6. MEADS algorithm a priori initial conditions, statistics, and convergence tolerances.

Parameter	Initial condition	Standard deviation	Convergence tolerance
Angle of attack (deg)	-15.8780	6.0	0.005
Angle of sideslip (deg)	-0.2679	4.0	0.005
Dynamic pressure (Pa)	3518.3	1000	10.0
Static pressure (Pa)	6.9463	1.0E-6	1.0
Transducer bias (Pa)	0.0	100	1.0
Transducer scale factor	1.0	0.1	1.0E-4
Transducer nonlinearity (1/Pa)	0.0	0.001	1.0E-8

To understand the reason for the restriction on the static pressure estimate, recall the pressure ratio $R = P_\infty / P_t$ defined by Eq. (3.21). At high Mach numbers, the quantity RM^2 is nearly constant, as shown in Figure 4.11. This invariance means that even small deviations in static pressure drastically affect Mach number, which is required to call the CFD pressure database.[25,26,31,32] In practice, loosening the static pressure *a priori* uncertainty to larger than 1.0 Pa results in Mach number divergence, indicating that this parameter demonstrates low observability.

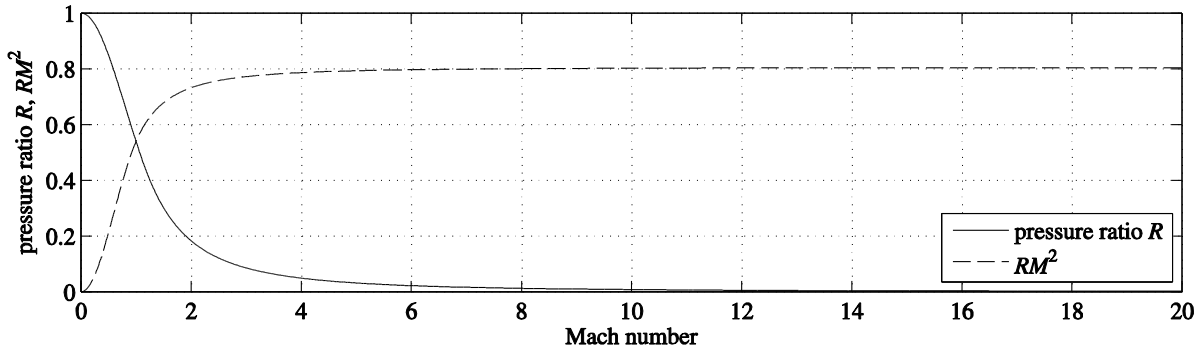

Figure 4.11. Variation of pressure ratio across Mach number, γ = 1.335.

Thus, although the estimators described here are formulated with static pressure as a parameter, to prevent divergence due to poor observability the *a priori* uncertainty on it is set so that the estimated static pressure is the hydrostatic pressure obtained from the IMU-derived atmosphere reconstruction. Because of the reliance of the algorithm on IMU-derived planet-relative velocity and freestream pressure, the MEADS solution is referred to as the IMU-aided MEADS solution.

Chapter 5: Statistical Reconstruction with Inertial Navigation and Monte Carlo Techniques

It has been shown that using the observed landing site in INSTAR restricts the range of possible initial state conditions by reducing the initial state condition uncertainties.[24] In that analysis it was concluded that for MSL, simply using landing site location as the redundant data in INSTAR results in the best estimate of the trajectory and corresponding statistics, and cannot be substantially improved with MEADS data. Thus, it will be useful to examine how FADS-based statistical reconstruction algorithms improve the estimates of the atmosphere and aerodynamics in concert with INSTAR.

In this chapter the methods of addressing the principal issues identified in Chapter 1 are developed. These methods are extensions of the reconstruction techniques in Chapter 4 that are in turn based on the fundamental concepts in Chapter 3, and are applied to the MSL EDL sequence described in Chapter 2.

5.1 Sources of Error and Uncertainty

As trajectory reconstruction involves a variety of sources of data, there are a variety of sources of error and uncertainty. Statistical reconstruction methods attempt to account for these uncertainties and provide solutions coupled with a range of uncertainty. Other methods may provide a solution that has the highest probability of occurring. In any case, any solution based on imperfect data is meaningless

without an associated uncertainty. In the context of trajectory reconstruction, uncertainties may be due to:

- *Sensor errors*. Sensors are imperfect devices and may exhibit behavior that alters the output, preventing the sensed measurements from being representative of the true and unknowable values. Types of sensor errors include biases, scale factors, and misalignments, noise, and quantization.
- *Initial condition errors*. Initial state conditions (position, velocity, orientation) are not known perfectly, and are typically provided with a measurement covariance that specifies the uncertainty of each initial state parameter.
- *Landing site measurement errors*. Like the initial conditions, measurements of the final position (i.e., landing site) are imperfect. Uncertainties associated with the landing site are typically provided by the mission radio tracking team.
- *CFD database/modeling errors*. Pre-flight planning involves modeling the dynamics of the vehicle in the flow along the predicted trajectory. Computational fluid dynamics (CFD) models are not perfectly representative of either the dynamics or the atmosphere, and errors in CFD solutions will affect reconstructions that use these solutions.

Other sources of uncertainty are specific to flush air data systems and include port location error, timing error, pneumatic lag, thermal transpiration, and system calibration and temperature uncertainty. The uncertainty contributions due to these sources are small and for the purposes of this study will be neglected (see §5.4.1 for a discussion of pressure measurement uncertainty).[31]

5.2 Probabilistic Analysis using INSTAR

One of the major advantages of the INSTAR approach is that it permits arbitrary parameter probability distributions to be specified or estimated throughout the process, permitting analysis of the solutions in a probabilistic sense. In this section, a probabilistic approach to implementing INSTAR and interpreting the results will be discussed.

It is of interest to examine the probability density function p of a set of samples because it provides the probability of those samples occurring (see §3.3). Common density functions include Gaussian and uniform functions, but these rarely occur in nature and are often used out of convenience. It is therefore useful at times to estimate the true density function.

By far the most common density function estimator is the histogram. A histogram approximates the density function by dividing the array of observations into intervals or "bins" then counting the number of observations that fall into each bin. Thus, the bin width, together with the number of observations in each bin, defines the histogram.

Consider a set of n observations $X_1 \ldots X_n$ where X_i is the ith observation of the set. The histogram is then

$$\hat{p}(x) = \frac{1}{nh}\left(\text{number of } X_i \text{ in same bin as } x\right) \tag{5.1}$$

where h is the bin width (or bandwidth). An example of a histogram is shown in the upper chart of Figure 5.1. A set of 1,000 normally-distributed random numbers with mean 15 and variance 8 is divided into 10 bins to generate the histogram. A Gaussian distribution with the same mean and variance is also plotted to show how the histogram estimate compares to the underlying density.

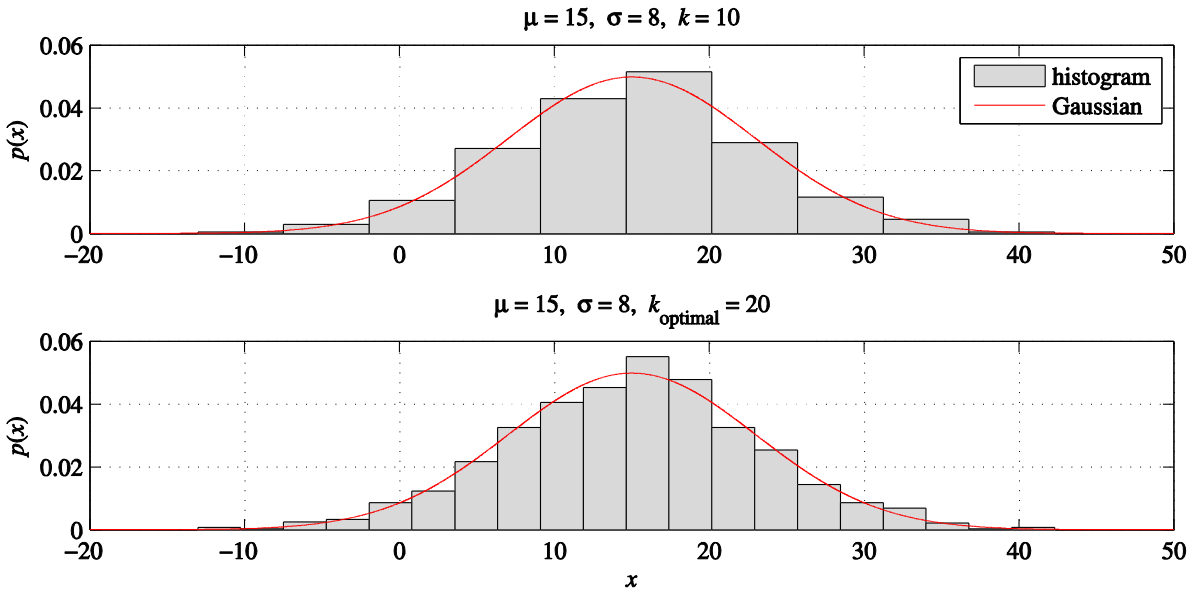

Figure 5.1. Histograms of normally distributed data with mean 15 and variance 8. The upper chart has 10 bins and the lower bin has an optimized bin number of 20.

Selecting the number of bins k is of great importance when constructing a histogram, as it is necessary to choose the number of bins that best approximate the underlying density function. There are many methods of optimizing k.[61,62,63] In the present work, Scott's method is used.[63,64] Scott determined that an optimal bin width may be approximated by

$$h^* = 3.5\sigma_x n^{-1/3} \tag{5.2}$$

where σ_x is the standard deviation of the observations and n is the number of observations. The optimal number of bins is therefore

$$k = \frac{X_{\max} - X_{\min}}{h^*} \tag{5.3}$$

where $X_{\max}$ is the observation maxima and $X_{\min}$ is the observation minima. The value computed in Eq. (5.3) is rounded up to the nearest integer. In Figure 5.1, the lower chart shows that the optimized number of bins for the same set of 1,000 normally distributed random numbers is 18. The new histogram is shown to compare to the histogram with the non-optimized bins in the upper chart.

It also useful to verify how well a set of observations matches a specified probability density model using the chi-squared (χ^2) goodness-of-fit test, also known as Pearson's chi-squared test.[65] The chi-squared goodness of fit test compares the frequency of the observations (number of observations in each bin) to the frequencies expected from the model distribution. The test statistic is

$$\chi^2 = \sum_{i=1}^{k} \frac{\left(O_i - E_i\right)^2}{E_i} \tag{5.4}$$

where O_i is the number of observations X_i in the *i*th of *k* bins and E_i is the expected number of observations. If E_i is sufficiently large, the statistic will approximately follow a chi-squared distribution, and may be compared to the critical value from the corresponding chi-squared distribution. The critical value is obtained from the chi-squared distribution curve with a specified significance level (usually 5%) and computed degrees of freedom (usually the number of bins minus one minus the number of parameters). If the computed chi-squared value *exceeds* the critical value, the observation distribution *does not* follow the expected distribution. Otherwise, the observation may follow the expected distribution.

In summary, the observations may be checked for Gaussian behavior by using the chi-squared goodness-of-fit test, with the optimal number of bins provided by Scott's method. These techniques will be used to examine the validity of the Gaussian assumption for the initial conditions and the uniform assumption for the landing site dispersions, and discussed in Chapter 6.

5.3 CFD Aerodynamic Database Dispersion

It is necessary to examine how the CFD database may be dispersed in INSTAR. As discussed in §2.3, computational fluid dynamics is used to generate tables of force, moment, and pressure coefficients for the MSL entry vehicle. Together, these tables make up the MSL aerodynamic database.[45] Since CFD solutions are not perfectly representative of the true and unknowable flow, it is necessary to account for the uncertainties in CFD and examine how they affect the atmosphere and aerodynamics. In the context of INSTAR, this means randomly perturbing the coefficient profiles obtained from the tables for each Monte Carlo run.

Traditional CFD dispersion methods consist of shifting the response curve by a fraction of the uncertainty magnitude. For a generic function *f*, this type of dispersion takes the form

$$\breve{f}(x) = f(x) + \varepsilon_i U(x) \tag{5.5}$$

where the arc embellishment indicates a dispersed function, f is the nominal function, U defines the magnitude of the uncertainty, and ε_i is a random value that satisfies $-1 \le \varepsilon_i \le 1$. While this method is useful in that the probability distribution of $\breve{f}$ will essentially be that of ε_i, it does not permit "tilts" of the response curve or phase shifting.[66] Thus, in the current analysis, a method proposed by Pinier[66] is used to perturb the axial force coefficient. For the ith Monte Carlo run, the dispersion function takes the form

$$\breve{C}_{A,i}(t) = C_{A,\mathrm{CFD}}(t) + \varepsilon_i L U(t) + \left(1 - |\varepsilon_i L|\right) G_i(t) U(t) \tag{5.6}$$

where ε_i is a randomly generated number uniformly distributed between -1 and 1, and L is a bias limit that is selected to be 1. The function $G_i(t)$ is a randomly generated dispersed function of a form that is dependent on the curve that is being perturbed. Possibilities include simple polynomial or trigonometric functions, Fourier expansions, and Hermite polynomials. For this analysis, the chosen form is

$$G_i = A \sin\left(2\pi f t + \phi\right) \tag{5.7}$$

where A is a randomly generated amplitude uniformly distributed between 0 and 1, f is a randomly generated frequency with a uniformly distributed period between 200 s and 400 s, and ϕ is a randomly generated phase angle uniformly distributed between 0 and 2π rad. The period is selected so that the dispersion functions provide "long-term" shifts in the axial force coefficient, corresponding to biases and tilts of the C_A surface in Mach-α_T space. Note that although uniform distributions are assumed for ε_i, A, f, and ϕ, this method does not require such an assumption and any distribution function or mix of functions may be used.

The function $U(t)$ is defined by the axial force coefficient uncertainty:

$$U(t) = \sigma_{C_{A,\mathrm{CFD}}} C_{A,\mathrm{CFD}}(t) \tag{5.8}$$

where $\sigma_{C_{A,\mathrm{CFD}}}$ is the axial force coefficient uncertainty and is a function of Mach number, and $C_{A,\mathrm{CFD}}$ is the nominal axial force coefficient obtained from the CFD tables. The CFD axial force coefficient uncertainty is ±5% above a Knudsen number of 0.1, ±3% above Mach 10 (hypersonic), and ±10% below Mach 5 (supersonic), normally distributed in a 3σ sense (see Table 5.1).[46] The uncertainty is linearly interpolated between these two Mach numbers. For comparison, the LaRC model used to disperse the CFD axial force coefficient was $\bar{C}_{A,i}(t) = C_{A,\mathrm{CFD}}(t)(1 + \sigma_{C_{A,\mathrm{CFD}}})$.

Table 5.1. MSL CFD aerodynamic force and moment uncertainties.

	C_A	C_N, C_Y	C_m	C_n	C_l
Knudsen > 0.1	±5%	±0.1, ±10%	±0.005, ±20%	±0.005, ±20%	0.0005
Mach > 10	±3%	±0.1, ±10%	±0.006, ±20%	±0.003, ±20%	0.00022
Mach < 5	±10%	±0.1, ±10%	±0.005, ±20%	±0.005, ±20%	0.00023

Pre-flight uncertainties for the CFD aerodynamic database were generated from heritage values from previous Mars missions.[46] Table 5.1, adapted from Ref. 46, lists the MSL CFD aerodynamic force and moment uncertainties for various regimes. Uncertainties are linearly blended between regimes.

An example of the dispersed axial force coefficients is shown in Figure 5.2. Shown are the dispersed curves along with the nominal (non-dispersed) axial force coefficient, and the uncertainty bands from dispersions. The "long-term" shifts can be seen, as well as dispersions that are mostly bias. Note that the selection of uniform distributions forces the limits of the dispersion to be bound by $\sigma_{C_{A,\mathrm{CFD}}}$, that is, the random number generator will never provide a value of the dispersed axial force coefficient that exceeds $\sigma_{C_{A,\mathrm{CFD}}}$.

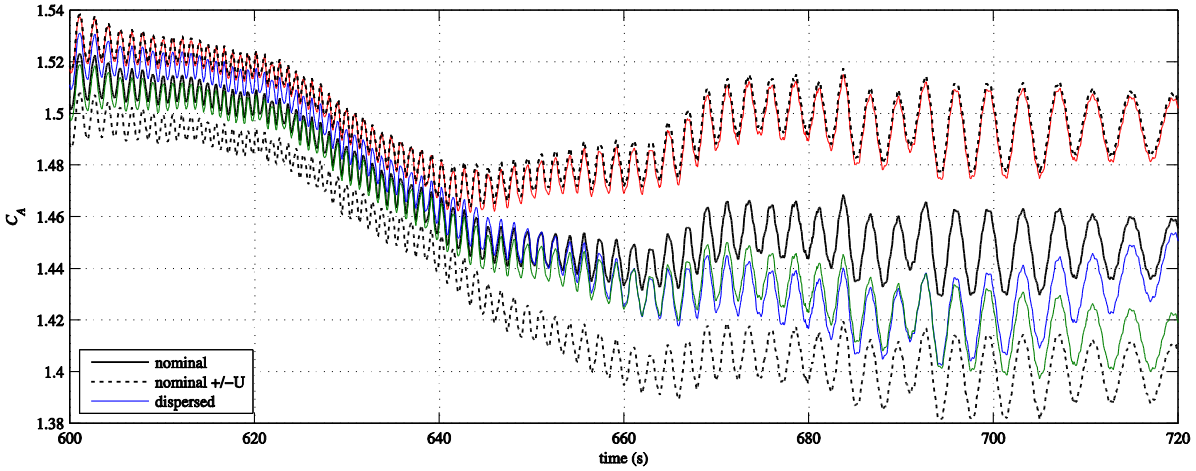

Figure 5.2. Nominal axial force coefficient (solid black line) with dispersions (blue, red, and green lines) bounded by uncertainties (dotted black lines).

CFD pressure coefficients are also provided in a database (one table for each of the seven taps), and are also dispersed to examine how pressure CFD uncertainties affect the solution uncertainties. For the present analysis, however, instead of using polynomial-based dispersion method of the axial force coefficient, the CFD table values themselves are perturbed rather than the pressure curve obtained through table lookups. This more direct approach is taken to demonstrate the flexibility of the INSTAR method.

To perturb the CFD pressure coefficients, it is assumed that the pressure at any grid point in the table is known to within 2%, normally distributed in a 3σ sense. Random numbers are generated using these criteria and added to the nominal grid point values. This perturbed database is then used

for a single Monte Carlo run. For the next run, new random dispersions are generated and a new table is used. CFD correlations are therefore introduced and accounted for by perturbing the grid points simultaneously and using the dispersed table to interpolate and obtain the pressure coefficient.

According to Eq. (2.8), any adjustment to the surface pressure distribution will affect the axial force coefficient, and vice versa. One method of accurately tracking the effects of dispersing the surface pressures coefficients on the axial force coefficients (or vice versa) would be to re-run the CFD solution for every dispersion, which is impractical. Taking this relationship into account is beyond the scope of the present work, but may be of interest in future INSTAR applications.

5.4 Flush Air Data System Observations in INSTAR

Now that the methods of inertial navigation, atmosphere reconstruction, INSTAR, FADS-based reconstruction, and CFD database dispersion have been discussed, they may be combined into a framework that enables the inclusion of MEADS observations in INSTAR.

The method of utilizing pressure data in INSTAR is shown in Figure 5.3. This method assumes that the trajectory solutions from INSTAR and the landing site may not be appreciably improved with MEADS observations, and it introduces the minimum variance statistical estimation algorithm to the INSTAR process. In essence, Monte Carlo dispersions from INSTAR are introduced into the MEADS minimum variance algorithm. The upper half of the flowchart is essentially the same as the INSTAR process used to update the trajectory initial conditions and uncertainties with the landing site location. The box labeled “Inertial Navigation & Atmosphere Reconstruction” consists of the entirety of the flowchart in Figure 4.1, and the box labeled “Minimum Variance” consists of the entirety of the flowchart in Figure 4.10. The bolded blocks indicate Monte Carlo dispersions and the rounded rectangles indicate solution estimates and uncertainties obtained from the dispersions.

Of particular note in Figure 5.3 is the relationship between the inertial navigation component and the minimum variance component. Parameters derived from the dispersed state and atmosphere (namely, inertial velocity and freestream pressure, respectively) that have been constrained by the landing site are passed through the minimum variance algorithm, which is run for each of these IMU-derived trajectory profiles. Thus, the minimum variance solutions are also dispersed using Monte Carlo techniques, and therefore statistics may be obtained along the trajectory. Note that the minimum variance aerodynamic and atmosphere solutions are not passed back into the INSTAR portion of the process, and thus the IMU-derived parameters are not updated using the MEADS pressures.

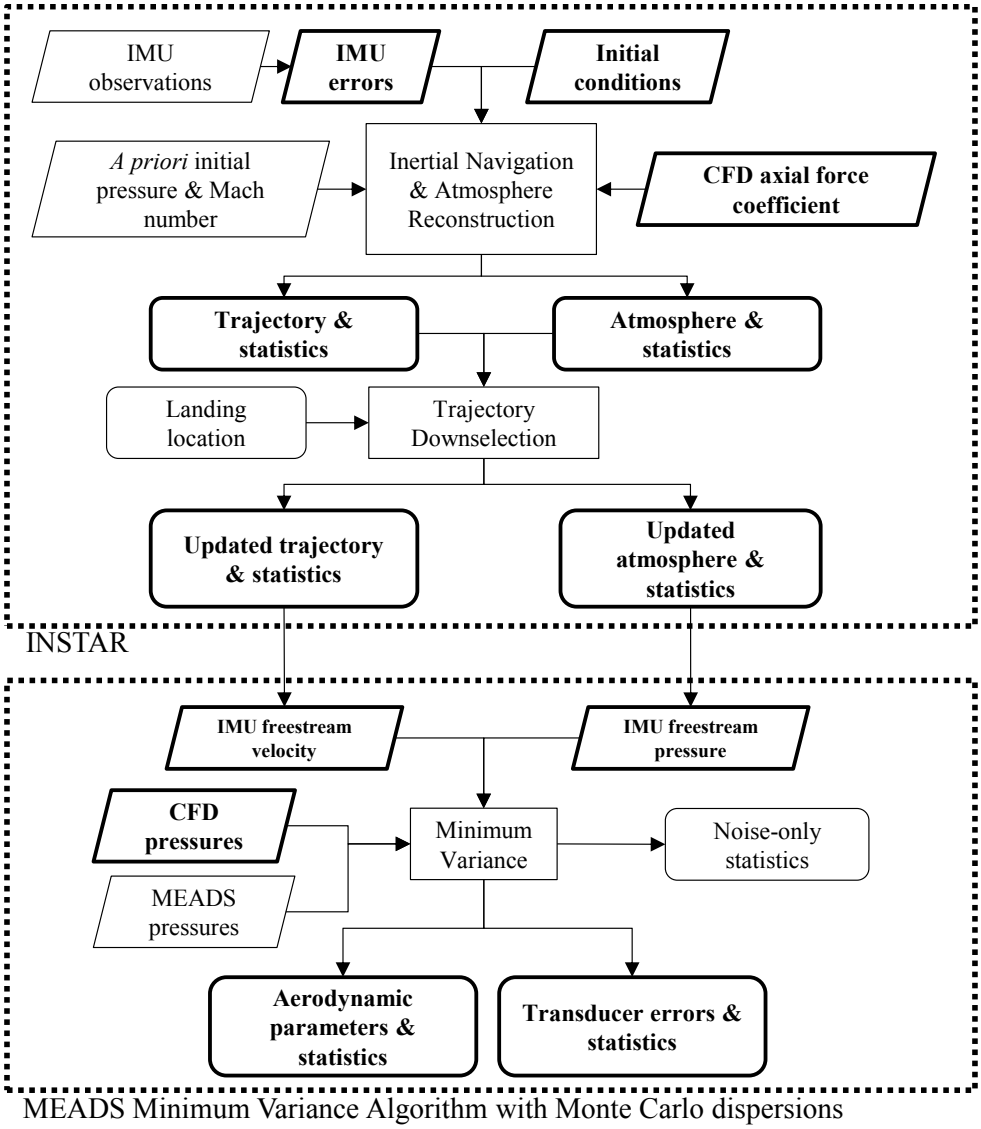

Figure 5.3. Method of considering FADS pressures using INSTAR and minimum variance. Bolded blocks represent Monte Carlo dispersions, rounded blocks are outputs.

5.4.1 MEADS-Derived Parameters

Because the CFD pressure database is provided partially as a function of Mach number, a Mach number estimate is required for each inner loop iteration of the MEADS minimum variance algorithm (see Figure 4.10). To obtain this estimate, an approach similar to that by Karlgaard *et al*. in Ref. 32 is taken, in which the planet-relative velocity from the INSTAR solution is passed into the MEADS algorithm. The computed Mach number is then

$$M_{\infty,\mathrm{MEADS}} = \frac{V_{\infty,\mathrm{INSTAR}}}{\sqrt{\gamma P_{\infty,\mathrm{MEADS}} / \rho_{\infty,\mathrm{MEADS}}}} \tag{5.9}$$

where

$$\rho_{\infty,\mathrm{MEADS}} = \frac{2q_{\infty,\mathrm{MEADS}}}{V^2_{\infty,\mathrm{INSTAR}}} \tag{5.10}$$

and the dynamic and static pressures are from the minimum variance state estimate in Eq. (4.35). Recall that the static pressure estimate is simply the pressure obtained from the integration of the hydrostatic equation from the IMU observations. Also, note that the only difference between the MEADS-derived Mach number and the IMU/INSTAR-derived Mach number is the way density is computed.

A MEADS-derived ambient temperature may also be computed using the equation of state:

$$T_{\infty,\mathrm{MEADS}} = \frac{\mathcal{M} P_{\infty,\mathrm{MEADS}}}{\mathcal{R} \rho_{\infty,\mathrm{MEADS}}} \tag{5.11}$$

The axial force coefficient may be computed directly from the MEADS/INSTAR solution using the minimum variance dynamic pressure estimate without the use of the aerodynamic database:

$$C_{A,\mathrm{MEADS}} = -\frac{ma_x}{S_{ref} q_{\infty,\mathrm{MEADS}}} \tag{5.12}$$

Recall from §2.3 and §4.3 that the CFD surface pressure coefficients are well-characterized near the stagnation region and that the MEADS dynamic pressure estimates are determined primarily by the pressure port nearest stagnation. Thus, these MEADS dynamic pressure estimates enable derivation of axial force coefficient and freestream density estimates that are essentially independent of the CFD axial force coefficient, which has higher uncertainty due to larger variances in CFD solutions near the edges of the heat shield. The MEADS-derived freestream temperature and Mach number also rely on MEADS freestream pressure estimates, which recall are simply the hydrostatic pressures and therefore contain CFD axial force coefficient information. In any case, these derived estimates and uncertainties may be compared to corresponding estimates and uncertainties from INSTAR, which again are dependent on CFD axial force coefficient.

The axial force coefficient may also be obtained from the CFD aerodynamic force database, which recall is a lookup table that is a function of Mach number and total angle of attack. Mach number and angle of attack may be obtained, in turn, from either the inertial navigation or atmosphere reconstructions to compute the INSTAR-derived axial force coefficient:

$$C_{A,\mathrm{ADB/IMU}} = C_{A,\mathrm{INSTAR}} = C_{A,\mathrm{CFD}}\left(M_{\infty,\mathrm{INSTAR}}, \alpha_{T,\mathrm{INSTAR}}\right) \tag{5.13}$$

where $M_{\infty,\mathrm{INSTAR}}$ is from Eq. (4.13) and $\alpha_{\mathrm{T,INSTAR}}$ is from Eq. (3.42) using the planet-relative wind angles from Eqs. (3.39) and (3.40).

The axial force coefficient may also be computed using the CFD aerodatabase tables and the MEADS-derived Mach number and total angle of attack:

$$C_{A,\text{ADB/MEADS}} = C_{A,\text{CFD}}\left(M_{\infty,\text{MEADS}}, \alpha_{\text{T,MEADS}}\right) \tag{5.14}$$

where $M_{\infty,\text{MEADS}}$ is from Eq. (5.9) and $\alpha_{\text{T,MEADS}}$ is from Eq. (3.42) using the wind-relative state estimates from Eq. (4.35). Analysis of the differences between the axial force coefficient computed from these three methods will be useful in understanding the dynamics of the entry vehicle.

5.4.2 Pressure Measurement Uncertainty

The *a priori* MEADS measurement uncertainties shown in Figure 2.14 include errors due to uncertainties in transducer and SSE temperature, calibration, quantization, port location, pressure leakage, lag uncertainty, thermal transpiration, and time tagging.[48] However, the minimum variance equations in §4.3.1 assume the errors $\boldsymbol{\varepsilon}$ are random and $E(\boldsymbol{\varepsilon}) = 0$ to maintain the unbiased characteristic of the estimator. Thus, for this analysis, only random measurement noise is included in the measurement covariance Γ_ε. Systematic errors may be modeled and dispersed using the "consider parameters" approach or in a Monte Carlo sense, but will not be considered in this analysis since the available error models do not include sufficient information to use more sophisticated modeling.

The measurement noise uncertainty is generated directly from the pressure observations by applying a running cubic polynomial fit with a width of 15 data points (approximately two seconds) to the unsmoothed pressure data. The standard deviations of the residuals between the unsmoothed and smoothed data are the new, data-derived noise uncertainty used in Γ_ε.

The new measurement uncertainties for ports 2, 4, 6, and 7 (stagnation, nose, and off the vertical axis) are shown in Figure 5.4. Results for other taps are comparable, with ports 1-4 having the highest reduction relative to the *a priori* uncertainties. The data-derived noise measurement uncertainties are generally lower in magnitude than the *a priori* uncertainties that contain full instrumentation errors, with some minor excursions at approximately 605 s for port 7. The implication here is that if the *a priori* uncertainties were realistic estimates of the random errors, then ports 2 and 4 are dominated by the systematic errors while the point-to-point random component dominates the port 6 and 7 measurement uncertainties. Implementing these smaller measurement uncertainties in Γ_ε has the net effect of reducing the uncertainties of the aerodynamic parameters obtained from the solution covariance in Eq. (4.39). These uncertainties may then be compared to those obtained from the Monte Carlo dispersions.

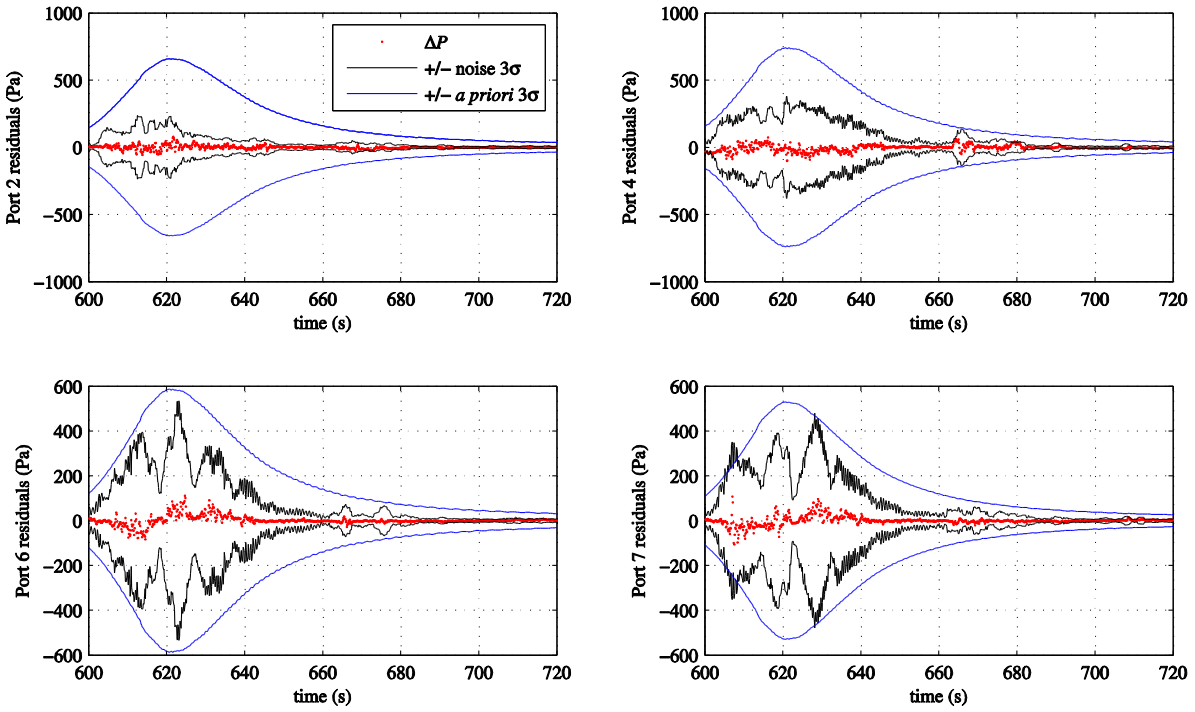

Figure 5.4. *A priori* and data-derived MEADS pressure measurement uncertainties.

The pressure residuals for the converged minimum variance solution for ports 2, 4, 6, and 7 are also shown in Figure 5.4. The residuals are generally smaller than the data-derived random component of the uncertainty, indicating that possibly 15 data points is too long an arc or that a higher order polynomial should be used. The solution is absorbing much of the signal, but there is some small amount of signal still remaining in the residuals that has not been captured by the biases, scale factors, or nonlinear terms. Virtually all of the residuals are bounded by the 3σ data-derived measurement uncertainties, with one or two exceptions occurring after 660 s. The region here, characterized by an increase in the measurement noise uncertainty, corresponds to the third bank maneuver and an apparent crosswind.

5.4.3 Summary of Parameters Derived from INSTAR and MEADS

Eqs. (5.15)-(5.22) summarize the aerodynamic and atmospheric parameters that may be recovered from both INSTAR and MEADS solutions. In general, the INSTAR solutions are computed from outputs of the INSTAR algorithm, and MEADS solutions are computed from outputs of both the MEADS and INSTAR algorithms. Uncertainties are computed from the standard deviations of the Monte Carlo dispersions.

$$C_A = \begin{cases} C_{A,\mathrm{CFD}}\left(M_{\infty,\mathrm{INSTAR}}, \alpha_{T,\mathrm{INSTAR}}\right) & \text{INSTAR} \quad \text{(a)} \\ -\dfrac{ma_x}{S_{ref} q_{\infty,\mathrm{MEADS}}} & \text{MEADS} \quad \text{(b)} \end{cases} \tag{5.15}$$

$$\rho_\infty = \begin{cases} -\dfrac{2ma_x}{V^2_{\infty,\mathrm{INSTAR}} C_{A,\mathrm{INSTAR}} S_{ref}} & \text{INSTAR} \quad \text{(a)} \\ \dfrac{2q_{\infty,\mathrm{MEADS}}}{V^2_{\infty,\mathrm{INSTAR}}} & \text{MEADS} \quad \text{(b)} \end{cases} \tag{5.16}$$

$$P_\infty = \begin{cases} P_0 - \int_h^{h_0} g \rho_{\infty,\mathrm{INSTAR}} dh & \text{INSTAR} \quad \text{(a)} \\ P_{\infty,\mathrm{INSTAR}} & \text{MEADS} \quad \text{(b)} \end{cases} \tag{5.17}$$

$$T_\infty = \begin{cases} \dfrac{\mathcal{M} P_{\infty,\mathrm{INSTAR}}}{\mathcal{R} \rho_{\infty,\mathrm{INSTAR}}} & \text{INSTAR} \quad \text{(a)} \\ \dfrac{\mathcal{M} P_{\infty,\mathrm{MEADS}}}{\mathcal{R} \rho_{\infty,\mathrm{MEADS}}} & \text{MEADS} \quad \text{(b)} \end{cases} \tag{5.18}$$

$$q_\infty = \begin{cases} \frac{1}{2} \rho_{\infty,\mathrm{INSTAR}} V^2_{\infty,\mathrm{INSTAR}} & \text{INSTAR} \quad \text{(a)} \\ \hat{q}_\infty & \text{MEADS} \quad \text{(b)} \end{cases} \tag{5.19}$$

$$\alpha = \begin{cases} \tan^{-1} w_{\mathrm{INSTAR}} / u_{\mathrm{INSTAR}} & \text{INSTAR} \quad \text{(a)} \\ \hat{\alpha} & \text{MEADS} \quad \text{(b)} \end{cases} \tag{5.20}$$

$$\beta = \begin{cases} \sin^{-1} v_{\mathrm{INSTAR}} / V_{\infty,\mathrm{INSTAR}} & \text{INSTAR} \quad \text{(a)} \\ \hat{\beta} & \text{MEADS} \quad \text{(b)} \end{cases} \tag{5.21}$$

$$M_\infty = \begin{cases} \dfrac{V_{\infty,\mathrm{INSTAR}}}{\sqrt{\gamma P_{\infty,\mathrm{INSTAR}} / \rho_{\infty,\mathrm{INSTAR}}}} & \text{INSTAR} \quad \text{(a)} \\ \dfrac{V_{\infty\mathrm{INSTAR}}}{\sqrt{\gamma P_{\infty,\mathrm{MEADS}} / \rho_{\infty,\mathrm{MEADS}}}} & \text{MEADS} \quad \text{(b)} \end{cases} \tag{5.22}$$

Chapter 6: Results and Analysis

The results obtained from INSTAR and the combined INSTAR and MEADS algorithm are now demonstrated using MSL flight data. Estimates and uncertainties are obtained for trajectory, atmosphere, and aerodynamic parameters. Comparisons are made to the preliminary solutions obtained by the reconstruction effort at Langley Research Center.[35,36] The LaRC extended Kalman filter solutions are labeled "NewSTEP" and the LaRC IMU-aided MEADS solutions are labeled "MEADS/IMU (LaRC)."

6.1 Trajectory

The vehicle trajectory consists of the position, velocity, and orientation through EDL. Table 6.1 and Table 6.2 lists the final initial conditions, IMU errors, and corresponding uncertainties obtained from INSTAR. Also shown are differences between the initial conditions and uncertainties obtained from INSTAR and the *a priori* initial conditions and uncertainties from Table 2.3, Table 4.1, and Table 4.2. Note that the listed axes are those of the descent stage frame.

In general, the changes in the initial conditions and IMU errors from *a priori* values are quite small relative to the values of the updated uncertainties (this is shown in the final column). The differences from the *a priori* initial conditions and IMU errors are almost all uniformly well under the 1σ uncertainties. The only parameters that have changed appreciably relative to the standard deviations are the *X*- and *Y*-axis Euler angles, the *z*-component of the acceleration scale factor (which recall is in the direction of the axial acceleration of the body frame), and the *y*-axis misalignment.

The relatively large change in the *z*-component of the acceleration scale factor and the small uncertainty indicates that the landing site information tightly constrains this value. A slightly different

solution would likely have been obtained had the *a priori* uncertainty been loosened, but 17 of the 21 uncertainties have decreased and the overall differences are satisfactory.

Table 6.1. Converged descent stage frame initial conditions, differences from *a priori* initial conditions, and standard deviations.

Parameter	Unit	Initial Conditions		Standard Deviations		ΔIC as σ
		Value	Δ	Value	Δ	
X_i	m	-8.969352E+04	0.1400	5.600	-0.4527	0.02
Y_i	m	5.080899E+06	0.1490	5.522	-1.0650	0.03
Z_i	m	-9.912516E+04	0.1971	12.540	-5.4694	0.02
$V_{X,i}$	m/s	-3.983227E+03	0.0009	0.007	0.0006	0.12
$V_{Y,i}$	m/s	-3.685549E+03	0.0006	0.009	0.0017	0.06
$V_{Z,i}$	m/s	-2.792502E+02	0.0011	0.008	0.0002	0.14
$\theta_{X,i}$	deg	-156.1162	0.0154	0.025	-0.0088	0.63
$\theta_{Y,i}$	deg	-65.9259	0.0168	0.018	-0.0150	0.92
$\theta_{Z,i}$	deg	-157.6956	0.0035	0.025	-0.0083	0.14

Table 6.2. Converged descent stage frame IMU errors, differences from *a priori* IMU errors, and standard deviations.

Parameter	Unit	IMU Errors		Standard Deviations		ΔIMU as σ
		Value	Δ	Value	Δ	
$SF_{a,x}$	--	2.5450E-05	2.5450E-05	1.4918E-04	-8.2349E-07	0.17
$SF_{a,y}$	--	2.2670E-05	2.2670E-05	1.6694E-04	1.6943E-05	0.14
$SF_{a,z}$	--	8.7736E-05	8.7736E-05	6.2743E-05	-8.7257E-05	1.40
$B_{a,x}$	μg	6.5375	6.5375	38.9727	5.6394	0.17
$B_{a,y}$	μg	-4.9229	4.9229	25.0605	-8.2728	0.20
$B_{a,z}$	μg	-2.6492	2.6492	27.0719	-6.2614	0.10
$SF_{\omega,x}$	--	-6.3704E-06	6.3704E-06	2.9852E-05	-3.4813E-06	0.21
$SF_{\omega,y}$	--	-1.0748E-06	1.0748E-06	3.1545E-05	-1.7882E-06	0.03
$SF_{\omega,z}$	--	-6.7717E-08	6.7717E-08	3.5922E-05	2.5887E-06	0.00
$B_{\omega,x}$	deg/s	-2.1619E-07	2.1619E-07	2.7303E-06	-4.7508E-08	0.08
$B_{\omega,y}$	deg/s	2.4971E-07	2.4971E-07	2.5629E-06	-2.1491E-07	0.10
$B_{\omega,z}$	deg/s	2.5001E-07	2.5001E-07	2.2212E-06	-5.5654E-07	0.11
ϕ_x	deg	-0.0007	0.0007	0.0168	0.0002	0.04
ϕ_y	deg	-0.0058	0.0058	0.0131	-0.0035	0.44
ϕ_z	deg	-0.0005	0.0005	0.0184	0.0017	0.03

The inertial position profiles in the M frame are shown in Figure 6.1, inertial velocities are shown in Figure 6.2, and quaternions are shown in Figure 6.3. The trajectory profiles are shown with the corresponding uncertainties, from both the first and final INSTAR iterations. Recall that the first

iteration corresponds to the trajectory computed from the JPL reference initial conditions and covariance.

In all cases, the change in the standard deviations from the first to final iterations is quite significant. The uncertainty of the *X* position component, for example, has decreased by almost 1.5 km by landing. Although there are some increases in velocity *Z* component uncertainty prior to maximum dynamic pressure at approximately 620 s, and some increases in quaternion uncertainty near chute deploy at approximately 800 s, these increases are small relative to the improvement in the remaining regions of the trajectory. Thus, using landing site location to constrain the range of possible trajectories provides a significant improvement to the trajectory uncertainties.

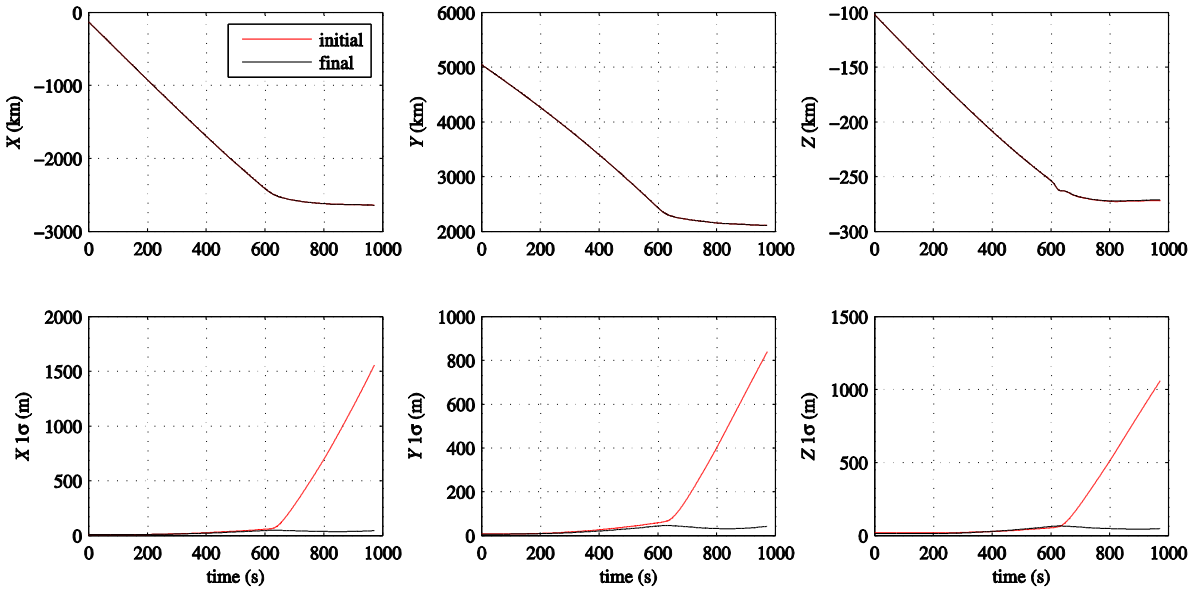

Figure 6.1. Reference and final position profiles and uncertainties, first and final INSTAR iterations.

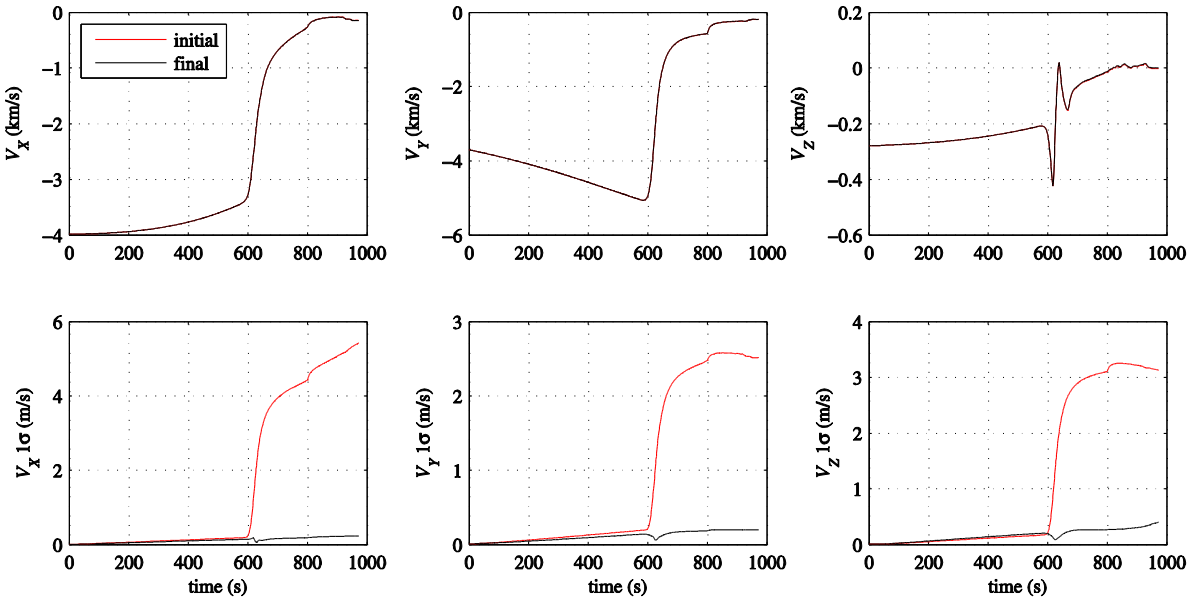

Figure 6.2. Reference and final velocity profiles and uncertainties, first and final INSTAR iterations.

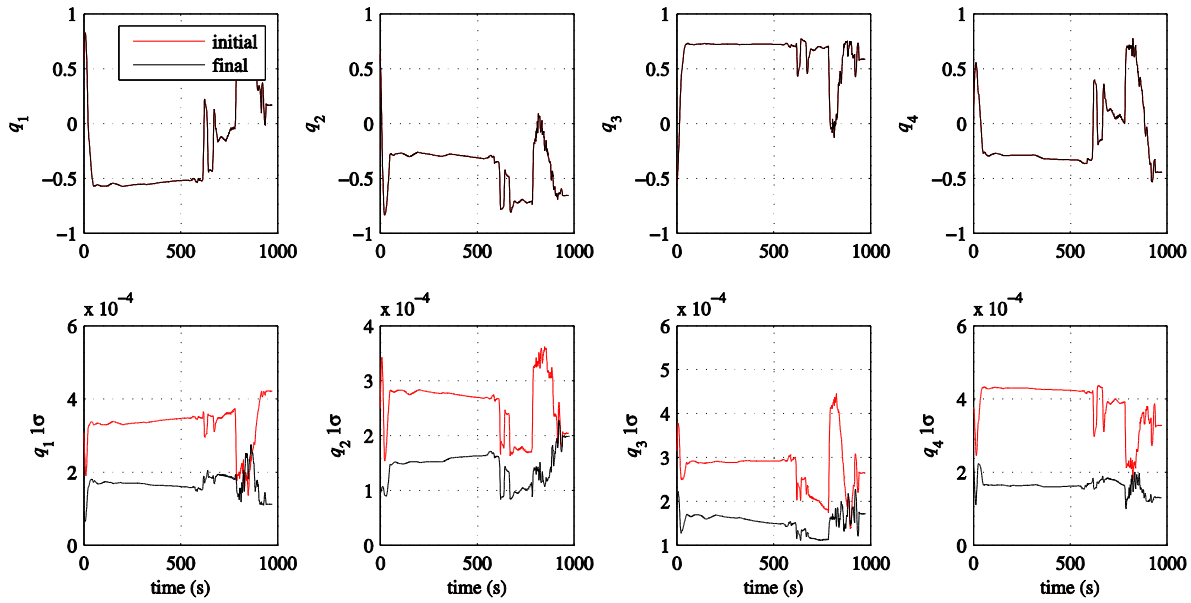

Figure 6.3. Reference and final quaternion profiles and uncertainties, first and final INSTAR iterations.

Altitude history in the M frame referenced from the vehicle landing radius in Table 2.4 is shown in Figure 6.4. Note that the lower left panel is a zoomed view of the upper left panel, spanning the relevant MEADS times. The peak difference between the INSTAR and NewSTEP altitudes is 237 m at 640 s. The INSTAR altitude at 640 s is 18.7 km, and as will be shown later, the Mach number is 10. The altitude uncertainties from INSTAR stay between 30 and 40 m beginning at this time, which is higher than those from NewSTEP. Note that the period between 660 s and 710 s is when the vehicle is increasing in altitude due to lift control, a feature of the EDL that has not been performed on any other Mars entry. The altitude difference between the two solutions at landing is 2.3 m.

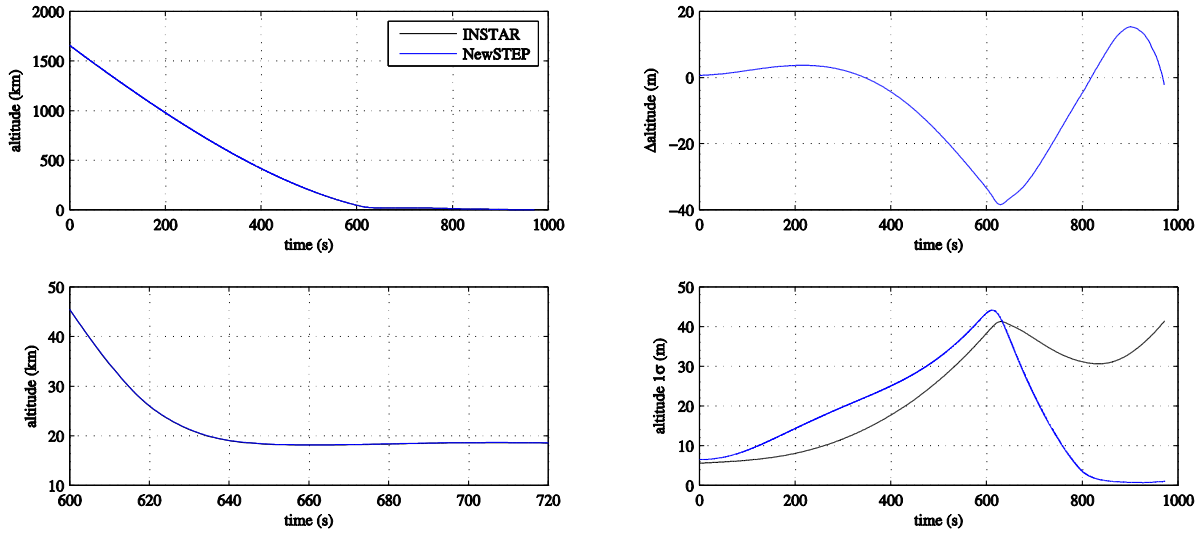

Figure 6.4. Altitude estimates, differences from INSTAR estimate, and uncertainties. The lower left panel is a zoomed-in view of the upper left panel.

INSTAR updates to the landing site are listed in Table 6.3. Since landing site is used to constrain and update the initial conditions in INSTAR, there is of course a significant improvement in the computed landing site. The reference trajectory, obtained from the radio tracking initial conditions, lands nearly a kilometer away from the reference landing site. The landing site from the initial conditions obtained by the INSTAR process has decreased this distance to less than ten meters. In comparison, the NewSTEP landing site difference is 27 m.[35]

Table 6.3. Comparison of landing site differences from reference using a) *a priori* initial conditions from JPL and b) converged intial conditions from INSTAR.

Component	*A priori* difference from reference landing site (m)	Final difference from reference landing site (m)
X	-522.614	6.702
Y	502.595	-1.604
Z	572.713	6.350
Magnitude	923.974	9.371

The implications of a decrease in landing site location difference are significant when the updates to the initial conditions and IMU errors are considered. Recall from Table 6.1 and Table 6.2 that nearly all of the differences between the reference initial conditions and IMU errors and the converged initial conditions and IMU errors are below the estimated 1σ values. Thus, there exists a combination of initial conditions and IMU errors that fall within the *a priori* uncertainties that enables the vehicle to arrive at the observed landing site to within several meters. Consider now that this improvement has been achieved simply by using landing site location as the redundant observation to constrain the trajectories. The assumption is therefore made that no further improvements may be made to the trajectory solution by considering other redundant data, though improvements may still be made to the atmosphere and aerodynamics using MEADS observations.

6.2 Atmosphere

Analysis of the atmospheric parameter estimates and uncertainties in the present work are limited to the times between 600 s and 720 s, which approximately corresponds to the range where the MEADS measurements are above the limit of 850 Pa. Note that in any plot in this work that displays a difference or Δ, the convention is that the parameter of interest is subtracted from the INSTAR- or IMU-derived parameter. Thus, a negative difference or Δ indicates that the parameter of interest is larger in magnitude than the INSTAR-derived parameter.

Also note that unless otherwise specified in the legends, black curves are INSTAR results, red curves are MEADS/INSTAR results, blue curves are NewSTEP extended Kalman filter results from LaRC, and green curves are the LaRC MEADS/INSTAR results.

When examining the atmosphere and aerodynamic results, recall from §2.3, §4.3, and §5.4 that the MEADS dynamic pressure estimate is determined primarily by the pressure at the port nearest to the stagnation point, a region that is well-characterized by CFD and supported by analytical flowfield solutions. Thus, the MEADS dynamic pressure estimate is essentially independent of the surface pressure coefficient distribution, which is not as well-characterized due to higher variances in CFD solutions and lack of analytical solutions near the edges of the heat shield. This distribution directly influences the CFD axial force coefficients and increases the associated uncertainties. Using a

minimum variance algorithm with Monte Carlo dispersion techniques permits the recovery of axial force coefficient and density estimates from MEADS pressures independent of the CFD axial force coefficients. MEADS-derived freestream temperature and Mach number rely on both the MEADS dynamic pressure and freestream pressure estimates, the latter of which are simply the hydrostatic pressures from INSTAR and therefore contain CFD axial force coefficient information. Thus, the MEADS dynamic pressures permit the comparison of these MEADS-derived estimates to those obtained through INSTAR.

Freestream density estimates, differences, and uncertainties are shown as a function of altitude in Figure 6.5 and as a function of time in Figure 6.6. The oscillations seen in the INSTAR estimate are of the same frequency as total angle of attack and have been smoothed out of the LaRC solutions. The density ratios in Figure 6.5 and the estimates in Figure 6.6 indicate that the INSTAR density solution from Eq. (5.16a) is overestimating freestream density by approximately 1-4% compared to the MEADS-derived density from Eq. (5.16b). As will be shown later, this is agreement with the CFD axial force coefficient, which is lower in magnitude than the axial force coefficient determined from the MEADS pressure-based solutions.

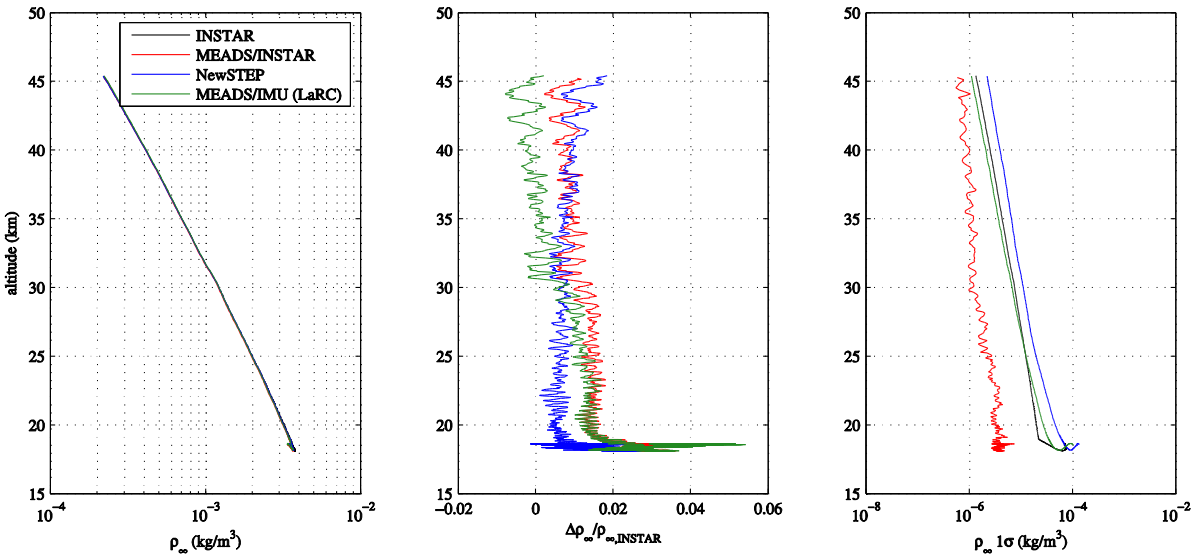

Figure 6.5. Freestream density estimates, differences from INSTAR estimate, and uncertainties, vs. altitude.

The INSTAR density uncertainties σ_{ρ_∞} derived from the dispersions of Eq. (5.16a) follow the behavior of the CFD axial force coefficient uncertainty shown later in Figure 6.15, indicating that the

CFD aerodatabase uncertainties are the dominant contributor. The MEADS/INSTAR σ_{ρ_∞} derived from the dispersions of Eq. (5.16b) is significantly smaller in magnitude than the other uncertainties, which is due to the relatively smaller distributions in $q_{\infty,\mathrm{MEADS}}$ (recall that the MEADS/INSTAR density is a function of the IMU freestream velocity, which has almost negligible uncertainty, and the MEADS/INSTAR dynamic pressure, which will be shown in Figure 6.11). The MEADS/INSTAR σ_{ρ_∞} is not representative of the true uncertainty as it does not include systematic errors in the transducers and does not totally account for the large uncertainties in the axial force coefficient because of its independence from the surface pressure coefficient distribution (recall that the surface pressure coefficient distribution is used to compute CFD axial force coefficient and has relatively high uncertainty).

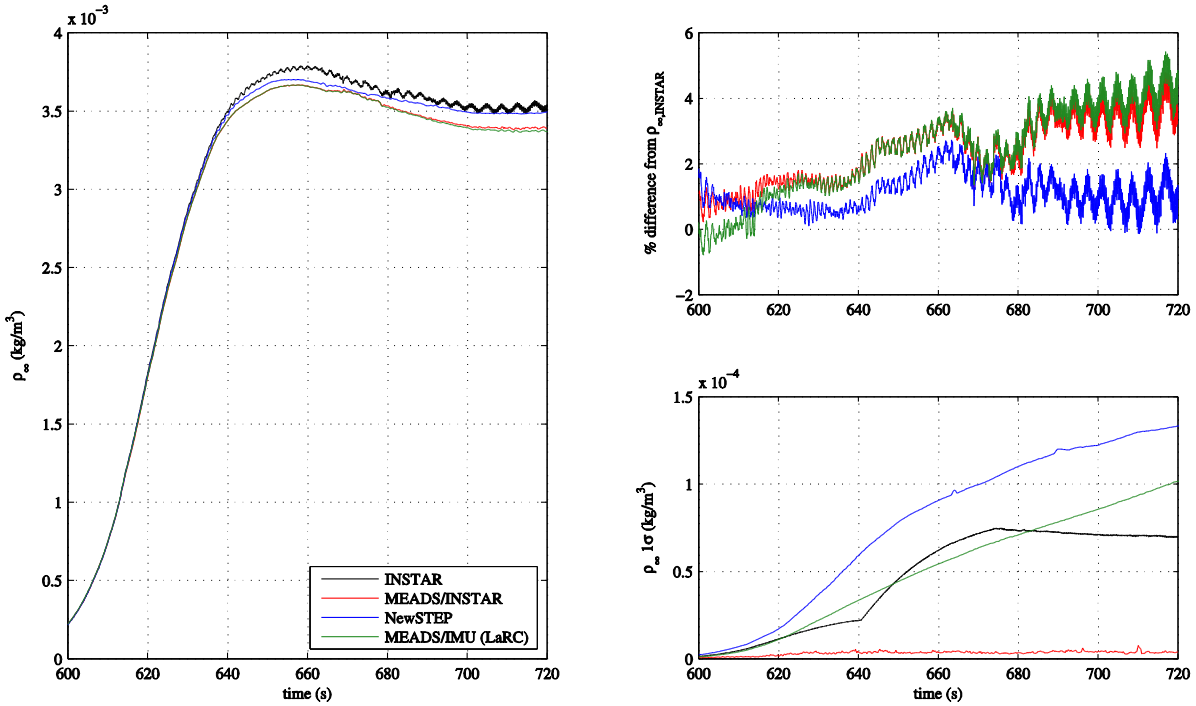

Figure 6.6. Freestream density estimates, differences from INSTAR estimate, and uncertainties, vs. time.

Freestream pressure estimates, differences, and uncertainties are shown as a function of altitude in Figure 6.7 and as a function of time in Figure 6.8. Rather than the solution presented in Ref. 35, the NewSTEP freestream pressure presented here is obtained by integrating the NewSTEP density in the

hydrostatic equation (this hydrostatic pressure will in turn be used to obtain the NewSTEP freestream temperature). Recall that in the present work, the MEADS freestream pressure is simply the IMU-derived hydrostatic pressure from Eq. (5.17a); thus, the MEADS freestream pressure is not shown in this plot.

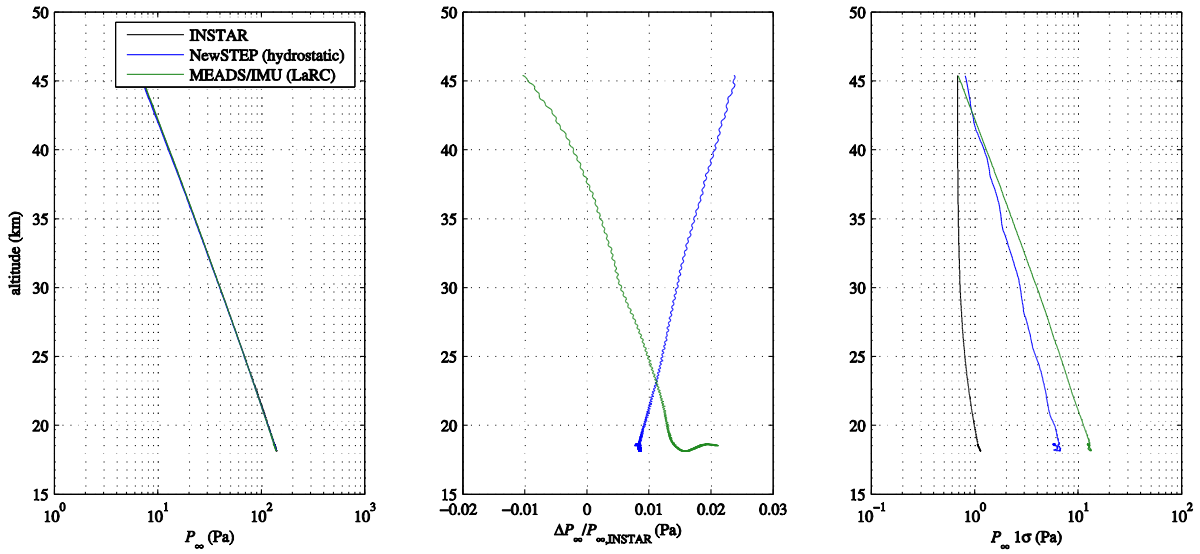

Figure 6.7. Freestream pressure estimates, differences from INSTAR estimate, and uncertainties, vs. altitude.

There is agreement between all three solutions to within 2%. Because of the small freestream pressure magnitude, the initial P_∞ uncertainty (10% 3σ, normal distribution) is quickly overtaken by the uncertainty in the integral term of Eq. (5.17a). Note the overall low uncertainty, less than 2 Pa, in the INSTAR freestream pressure compared to the other solutions. The density uncertainty behavior that is dominated by the CFD axial force coefficient uncertainty is not exhibited here since the density is integrated in the hydrostatic equation. Because the INSTAR freestream pressure is the only atmospheric parameter passed into the MEADS minimum variance algorithm, it will be shown that the resultant standard deviations of the MEADS parameter dispersions are small relative to the uncertainties in the CFD axial force coefficient.

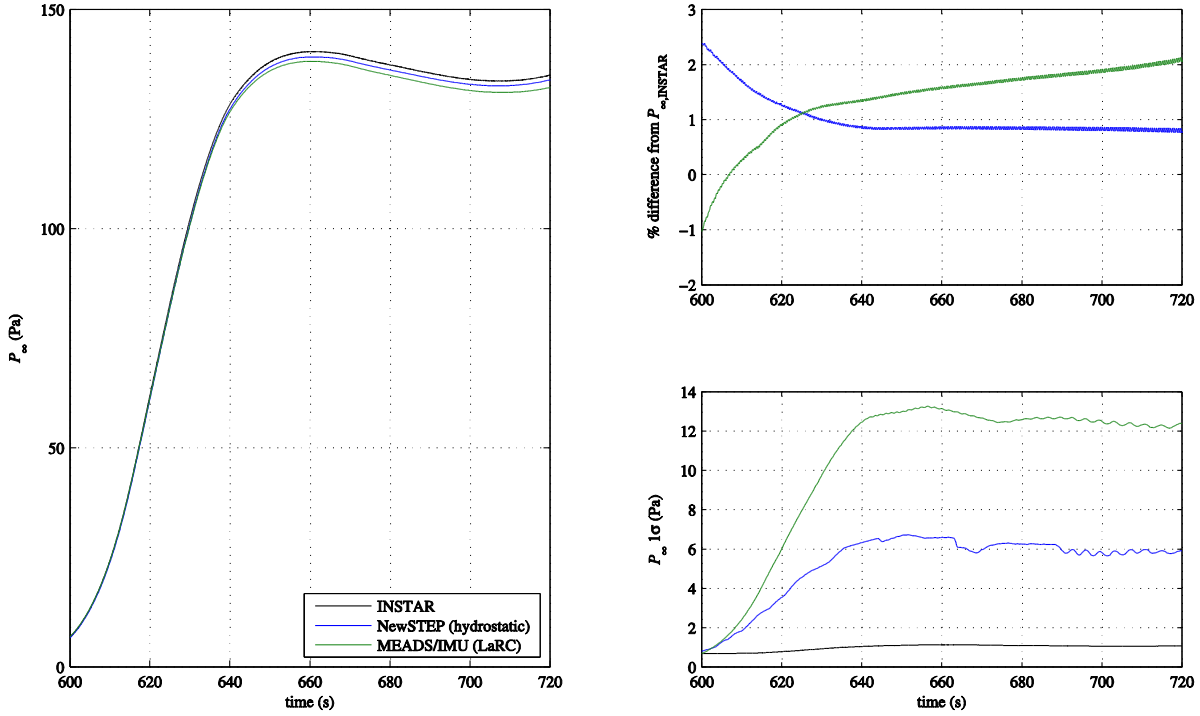

Figure 6.8. Freestream pressure estimates, differences from INSTAR estimate, and uncertainties, vs. time.

Freestream temperature estimates, differences, and uncertainties are shown as a function of altitude in Figure 6.9 and as a function of time in Figure 6.10. The NewSTEP solution presented here is obtained by using the NewSTEP density and the NewSTEP hydrostatic pressure in the equation of state. The oscillations due to the navigation filter accelerations are again present in the INSTAR solution.

The NewSTEP temperatures agree with the INSTAR-derived temperatures from Eq. (5.18.a) to within 2%. The MEADS/INSTAR freestream temperatures from Eq. (5.18.b) and MEADS/IMU (LaRC) freestream temperatures agree with the INSTAR freestream temperature to within approximately 2% before 640 s, with agreement within 4% outside of this range. Note the change in behavior in all curves just after 660 s, which again is at the third commanded bank reversal and approximately the time when the vehicle encountered an apparent crosswind.[35,36]

The INSTAR and MEADS/INSTAR-derived freestream temperature uncertainties σ_{T_∞} from the dispersions of Eqs. (5.18) are smaller than those from the LaRC solutions, since these derived uncertainties come from the INSTAR and MEADS/INSTAR σ_{ρ_∞} and σ_{P_∞}. The effects of the initial freestream pressure uncertainty are prevalent in the hypersonic regime, from 600-640 s, before the

CFD axial force coefficient uncertainty begins to dominate. As with the freestream density, the MEADS/INSTAR σ_{T_∞} is not completely representative of the true uncertainty due to the lack of systematic errors in the transducers and the small uncertainties in freestream pressure.

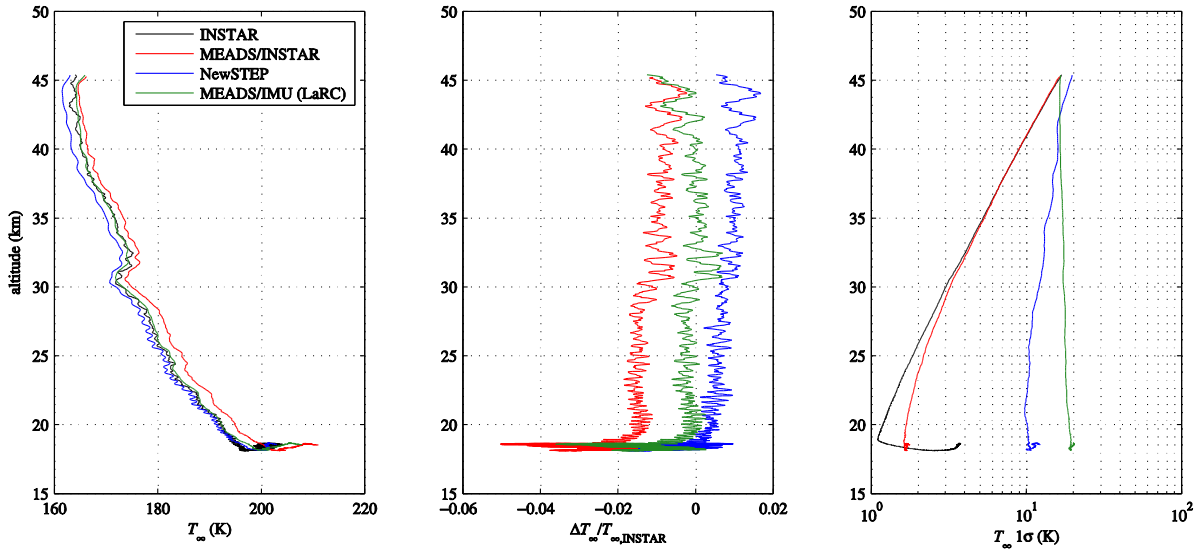

Figure 6.9. Freestream temperature estimates, differences from INSTAR estimate, and uncertainties, vs. altitude.

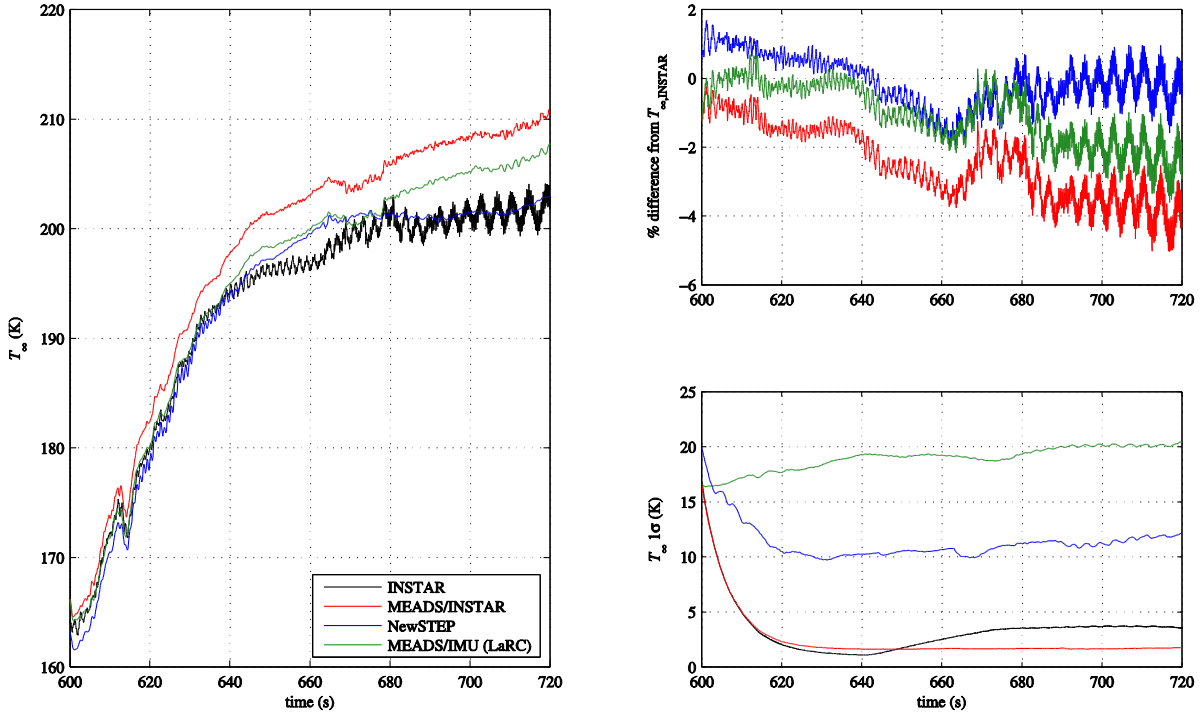

Figure 6.10. Freestream temperature estimates, differences from INSTAR estimate, and uncertainties, vs. time.

6.3 Aerodynamics

The vehicle aerodynamics consist of wind angles, dynamic pressure, Mach number, and forces and moments through EDL. Of the forces and moments, only the axial force coefficient will be analyzed in the present work.

Though not strictly considered aerodynamic parameters, the MEADS transducer error estimates and uncertainties from the minimum variance algorithm are listed in Table 6.4. The error estimates are obtained from the MEADS algorithm solution for the final converged trajectory defined by the initial conditions in Table 6.1 and IMU errors in Table 6.2. The statistics are obtained from the standard deviations of the dispersed transducer errors. Overall, the transducer errors are quite similar to those obtained by the LaRC reconstruction group and presented in Ref. 35, with all differences below 2σ with the exceptions of the port 1 scale factor (2.1σ), the port 6 scale factor (2.2σ), and the port 6 nonlinear term (3.3σ). Note, however, that the LaRC estimates are obtained by processing MEADS data for a longer period than the present work (up to 780 s as opposed to 720 s). Thus, differences in the solutions may be attributed in part to this, as well as to different data smoothing methods.

Table 6.4. MEADS transducer error estimates and uncertainties, with comparison to LaRC estimates.[35]

Port	Bias (Pa)	LaRC Bias	1σ (Pa)	Scale factor	LaRC scale factor	1σ	Nonlinearity (1/Pa)	LaRC Nonlinearity	1σ (1/Pa)
1	-8.21	-1.04	4.96	0.9994	0.9958	0.0017	-1.12E-08	7.64E-08	6.21E-08
2	-12.65	-2.83	6.95	0.9981	0.9947	0.0026	-8.55E-08	7.37E-09	1.08E-07
3	-6.26	4.77	8.46	1.0232	1.0209	0.0032	-1.23E-07	-3.94E-08	1.26E-07
4	-18.00	-7.05	8.93	1.0152	1.0100	0.0039	-3.56E-07	-7.83E-08	1.81E-07
5	42.64	47.05	9.40	0.9644	0.9635	0.0053	5.51E-07	7.26E-07	3.61E-07
6	6.44	7.89	9.81	0.9959	0.9868	0.0042	-5.60E-07	1.07E-07	2.03E-07
7	1.99	3.64	8.43	0.9936	0.9930	0.0037	-2.39E-07	-1.17E-08	1.87E-07

Reconstructed dynamic pressure estimates, residuals, and uncertainties are shown in Figure 6.11. Immediately it can be seen that the INSTAR dynamic pressure solution obtained from Eq. (5.19a) is consistently higher by up to 5% (250 Pa at $q_{\infty,\max}$) than the estimates obtained using other methods. This is consistent with the density differences in Figure 6.6, which show that the INSTAR density is approximately 1-4% higher than densities derived from MEADS and by LaRC. The MEADS-derived dynamic pressure from Eq. (5.19b) is in close agreement with the LaRC estimates.

Two versions of the dynamic pressure uncertainties σ_{q_∞} obtained from the covariance in Eq. (4.39) are shown in the lower right panel. The curve labeled "MEADS/INSTAR full instrumentation" are the uncertainties obtained from the MEADS solution covariance when the *a priori* pressure measurement uncertainty is used in Γ_ε, and are directly comparable to the LaRC MEADS/IMU uncertainties. The curve labeled "MEADS/INSTAR noise-only" are the uncertainties obtained from the MEADS solution covariance when the data-derived pressure noise uncertainty described in §5.4.2 is used in Γ_ε. As expected, these noise-only uncertainties are for the most part smaller in magnitude than those derived from the MEADS/INSTAR Monte Carlo dispersions. Recall that the MEADS/INSTAR σ_{q_∞} contains uncertainty contributions from all assumed sources of error except for systematic measurement errors such as those due to hysteresis. These types of errors will have to be included as either "considered parameters" or in a Monte Carlo sense, and are not considered in this work.

The INSTAR-derived σ_{q_∞} is obtained from the dispersions of Eq. (5.19a). Thus, the main contributor to this uncertainty is the INSTAR freestream density uncertainty from the dispersions of Eq. (5.16a), which is in turn dominated by the CFD axial force coefficient uncertainty, shown later in Figure 6.15. In fact, the change in σ_{C_A} behavior is visible at 640 s, which corresponds to Mach 10 and when σ_{C_A} begins to increase from 3% to 10%. Again, recall that the dynamic pressure estimate from MEADS is largely independent of the CFD surface pressure coefficient distribution that is used to obtain the CFD axial force coefficient and has relatively large uncertainty. INSTAR-derived σ_{q_∞} magnitude is therefore large compared to the MEADS σ_{q_∞} derived from the dispersions of Eq. (5.19b).

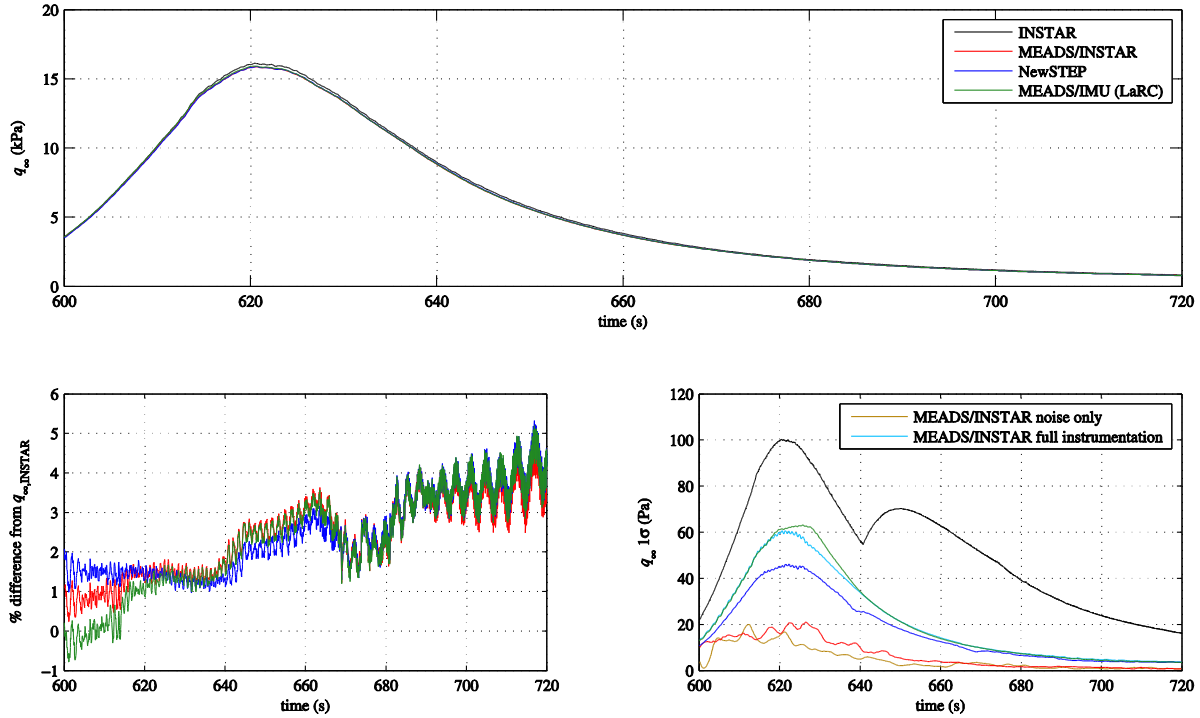

Figure 6.11. Dynamic pressure estimates, differences from INSTAR estimate, and uncertainties.

Finally, note that the MEADS/INSTAR full instrumentation uncertainties are generally smaller than the LaRC MEADS/IMU uncertainties. This is because *a priori* information is included in the MEADS/INSTAR covariance (see §3.4.2), though the MEADS/INSTAR uncertainty may occasionally be higher because of covariance inflation due to the effects of the considered parameters (see §4.3.1). This will be seen in the wind angle uncertainties.

Reconstructed angle of attack and sideslip are shown in Figure 6.12 and Figure 6.13, respectively. Recall that the INSTAR angle of attack and sideslip are obtained assuming no winds, such that the wind angles define the orientation of the inertial velocity vector with respect to a rigidly rotating atmosphere. The INSTAR solution from Eq. (5.20a) and the MEADS solution from Eq. (5.20b) agree to within a half of a degree until approximately 660 s, which is just after the third programmed bank reversal and the start of an apparent crosswind that causes the deviation between the INSTAR and MEADS solutions. At this time the MEADS minimum variance algorithm also began requiring 5-10 iterations to converge on local parameters, rather than 2-3 in other regions. The apparent crosswind and its effects on vehicle dynamics are discussed at length in Refs. 35 and 36.

As with dynamic pressure, there is good agreement between the MEADS estimates and the LaRC MEADS estimates. Differences in noise level are due to differences in data filtering prior to

processing. The LaRC MEADS estimate does not capture the amplitude of the angle of attack oscillations in the hypersonic regime because of the 1 Hz optimal Fourier filter used in that analysis.[35] This causes the high-amplitude differences between the INSTAR solution and the LaRC MEADS/IMU solutions in the lower left panels.

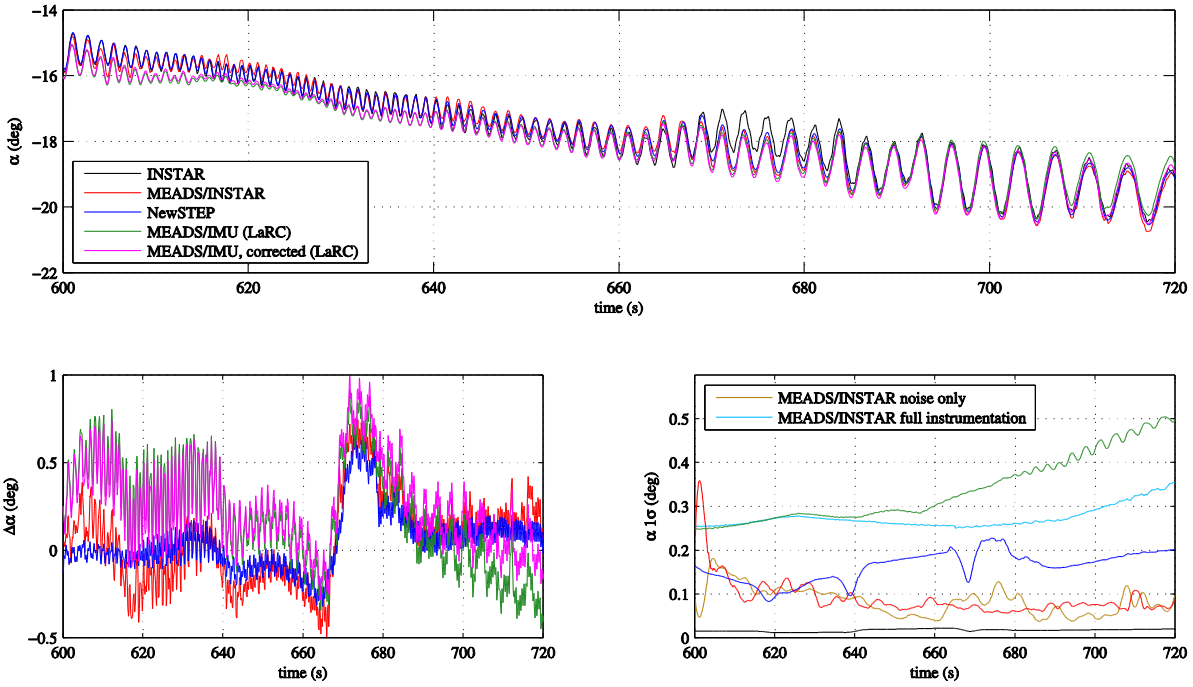

Figure 6.12. Angle of attack estimates, differences from INSTAR estimate, and uncertainties, planet- and wind-relative.

The angle of sideslip is expected to oscillate about zero because of the zero radial center of gravity offset, however, neither the inertial or MEADS sideslip estimates reflect this. Karlgaard *et al.* determined[35] that a hysteresis in either port 6 or 7 that results in a 25 Pa bias on either of those ports (negative for port 6, positive to port 7) can adjust the MEADS solution. This "corrected" LaRC MEADS/IMU solution is shown as the magenta curve (the green curve is the LaRC MEADS/IMU solution prior to this correction). It has been shown that accounting for this bias results in better agreement between the inertial and wind-relative sideslip angles.[35,36]

The wind angle uncertainties σ_α and σ_β are shown in the lower right panels of Figure 6.12 and Figure 6.13. The uncertainties from the noise-only covariance have high variation due to the point-to-point variations in the data-derived measurement uncertainties shown in Figure 5.4. The INSTAR-

derived angle uncertainties from the dispersions of Eq. (5.20a) and Eq. (5.21a) are relatively small because these are planet-relative angles that assume zero winds and depend only on the uncertainties in the trajectory. These uncertainties are therefore not directly comparable to the other uncertainties and are shown only for completeness.

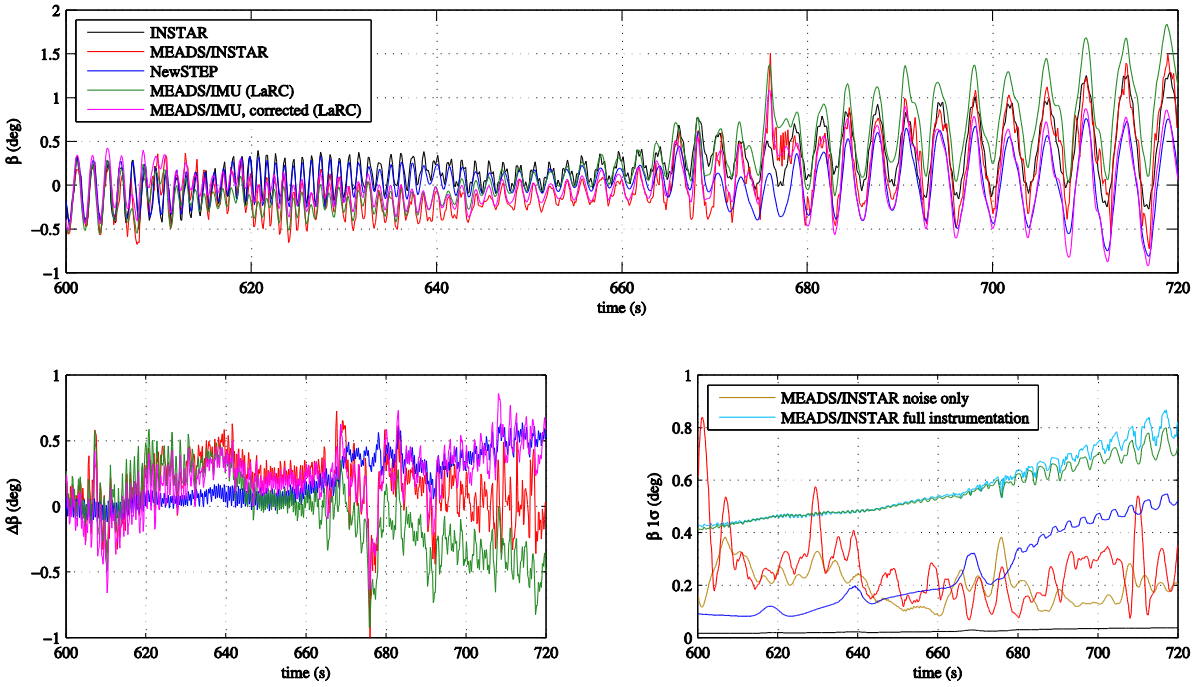

Figure 6.13. Angle of sideslip estimates, differences from INSTAR estimate, and uncertainties, planet- and wind-relative.

It is interesting to note that while the MEADS dynamic pressure uncertainties from the covariance in Eq. (4.39) are for the most part smaller in magnitude than the MEADS Monte Carlo uncertainties, the same cannot be said for the wind angle uncertainties from the MEADS covariance and the MEADS Monte Carlo dispersions. The implication is that in the case of the wind angles, the measurement noise dominates σ_α and σ_β. As before, neither sets of uncertainties include transducer calibration errors. Comparison to the uncertainties from the LaRC MEADS/IMU solution implies that the transducer calibration is a significant source of uncertainty, which has been determined to be the case.[48]

As in the case of dynamic pressure, the MEADS/INSTAR angle of attack uncertainties are generally smaller than the LaRC MEADS/IMU uncertainties because *a priori* information is included

in the covariance. However, the MEADS/INSTAR sideslip angle uncertainties are slightly larger than the LaRC MEADS/IMU uncertainties. This is likely because of covariance inflation due to the effects of the considered parameters. Thus, it may be concluded that the *a priori* information has a stronger effect on reducing the angle of attack uncertainties than the sideslip angle uncertainties.

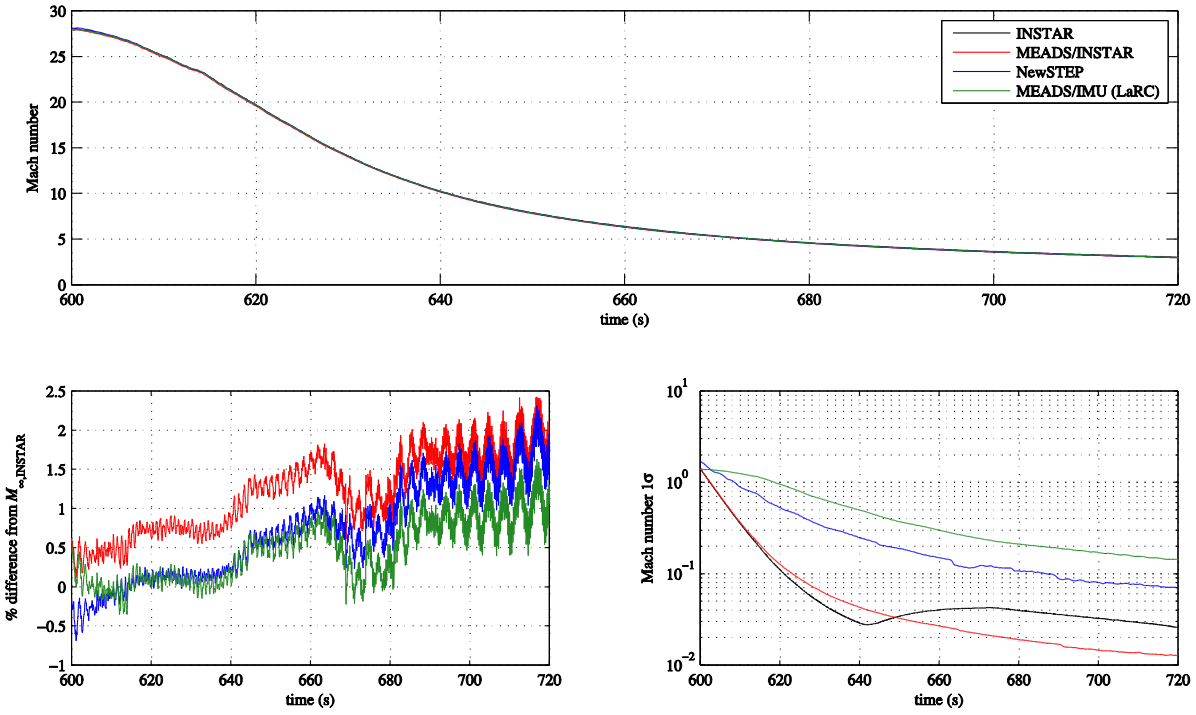

Figure 6.14. Mach number estimates, differences from INSTAR estimate, and uncertainties.

Mach number estimates and uncertainties are shown in Figure 6.14. The NewSTEP Mach number is obtained from the hydrostatically-derived freestream temperature profile, and agrees with the INSTAR Mach number to within approximately 1%. There is agreement to within 2% between the INSTAR Mach number from Eq. (5.22a) and MEADS-derived Mach number from Eq. (5.22b). Slightly better agreement exists between the MEADS/INSTAR and LaRC MEADS/INSTAR-derived solutions. Overall, the high INSTAR Mach number relative to the MEADS solution is consistent with the low INSTAR temperature and the relationship in Eq. (5.22a).

Mach number uncertainties σ_M are shown in the lower right panel. The relatively large initial INSTAR σ_M is due to the 10% uncertainty in the initial static pressure, which is used to begin the integration of the hydrostatic equation to get static pressure. As the magnitude of static pressure

increases, the initial static pressure uncertainty contribution decreases and the CFD aerodatabase uncertainty becomes dominant. This is indicated by the now-familiar increase in the INSTAR σ_M at 640 s. This increase does not appear in the MEADS-derived σ_M which recall is obtained from the standard deviations of the dispersion of Eq. (5.22b) and do not rely directly on the CFD axial force coefficient.

The reconstructed axial force coefficient with differences from the INSTAR solution are shown in Figure 6.15. Immediately it can be seen that there are two sets of curves following distinct behaviors. The lower C_A curves are obtained using the CFD aerodatabase from Eqs. (5.13) and (5.14) (labeled "ADB" and shown as the black, gray, and purple curves). The upper C_A curves are extracted from MEADS using Eq. (5.15b) (labeled "MEADS/INSTAR extracted" and "MEADS/IMU (LaRC) extracted" and shown as the red and green curves). Within these two sets there is agreement to within 1%. This is consistent with the similarity between the MEADS solutions obtained in this work and those obtained by LaRC.

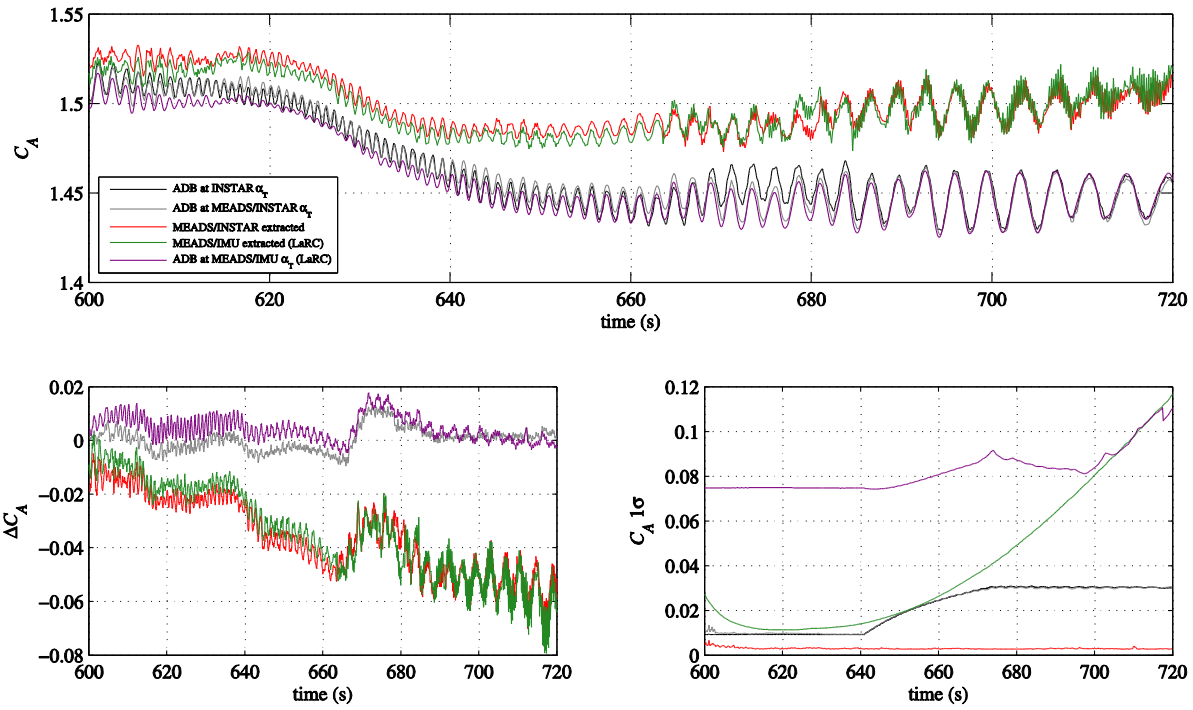

Figure 6.15. Axial force coefficient estimates, differences from INSTAR estimate, and uncertainties.

There is a marked difference between the two types of solutions, i.e., the difference between the aerodatabase-derived C_A and the MEADS-extracted C_A. This difference is between 1% and 2% in the hypersonic regime, before 640 s, and begins to increase thereafter to approximately 5% by 720 s. Schoenenberger *et al*. hypothesized that some of the differences between the aerodatabase-derived and MEADS-extracted hypersonic C_A could be reconciled by a combination of changes in heat shield mass caused by ablation, moisture absorption and outgassing, and CFD grid resolution in the shock structure. A "reconciled" C_A obtained by shifting the aerodatabase-derived curve to closer agreement with the MEADS-derived curve using hypersonic and supersonic multipliers is presented in that work.[36]

Consider that the C_A recovered from the CFD aerodatabase from Eq. (5.15a) is lower in magnitude than that of the C_A extracted from the MEADS solution in Eq. (5.15b). The immediate effect is that the INSTAR-derived freestream density, which is obtained using the CFD C_A as in Eq. (5.16a), is higher than that obtained using other methods. This was shown in Figure 6.5 and Figure 6.6 and is consistent with the behavior of other atmospheric and aerodynamic parameters derived from the axial force coefficient.

The axial force coefficient uncertainties provide some insight into the performance of the methods in this work. The σ_{C_A} from the aerodatabase at the INSTAR total angle of attack, derived from the dispersions of Eq. (5.15a), is essentially the *a priori* σ_{C_A} from Eq. (5.8) (recall that this uncertainty was chosen to define the upper and lower bounds of the dispersions). The similarity between the two uncertainty curves indicates that trajectory, mass, and initial static pressure uncertainties do not contribute significantly to the axial force coefficient uncertainty. However, there is some variation in σ_{C_A} derived from the dispersions of Eq. (5.14) and shown as the gray curve, obtained when the same aerodatabase is queried at the MEADS/INSTAR total angle of attack. This indicates that introducing dispersions due to pressure database uncertainties and transducer errors modestly increases the axial force coefficient uncertainty. The MEADS/INSTAR extracted σ_{C_A}, computed from the dispersions of Eq. (5.15b), is smaller in magnitude since the major contributor to these dispersions are those from dynamic pressure and this method does not rely directly on the CFD aerodatabase. Thus, it may be concluded that the majority of the axial force coefficient uncertainty is due to the CFD aerodatabase uncertainty.

Finally, recall that the LAURA CFD solutions near the edges of the heat shield are not as well-determined as the solutions near the stagnation region, and therefore the CFD C_A solutions have higher uncertainties than the uncertainties of C_P at a given location on the heat shield. Thus, it is expected that an improvement in the CFD aerodynamic database will improve the INSTAR-derived freestream density estimates, which will in turn improve the freestream pressure and temperature estimates. A more accurate C_P uncertainty model would also enable a better characterization of the relationship between the axial force coefficient and density solutions derived from MEADS and INSTAR.

6.4 Probability and Performance Analyses

As previously discussed, Gaussian distributions specified by the *a priori* covariance are assumed for the initial state dispersions. Also recall that a uniform distribution is assumed in the landing site space, i.e., every trajectory that terminates within 150 m of the reference landing site has an equal probability of occurring. The validity of the Gaussian assumption for the initial conditions and the uniform assumption for the landing site dispersions will now be investigated.

6.4.1 Initial Condition Probability Densities

Figure 6.16, Figure 6.17, and Figure 6.18 show probability density functions for the 822 *valid* initial position, velocity, and orientation parameters at the end of INSTAR iteration 1, respectively. Recall that *valid* in this case means that these initial conditions correspond to trajectories that satisfy the landing site uncertainty, i.e., these trajectories terminate within 150 m of the reference landing site. Although the initial condition dispersions were generated assuming Gaussian distributions, the distributions of the valid trajectories do not necessarily follow the same distribution. This delineation is important because the new initial conditions are generated from this valid pool by again assuming Gaussian distributions.

Note that in this analysis, correlations are not taken into account and the Gaussian density functions shown in the following figures are not precisely the functions used to generate new initial conditions and IMU errors (see §4.2.1 for a description of how the parameters are dispersed with correlations between iterations). Nevertheless, examining the distributions of each parameter separately can provide insight into the validity of the density assumptions.

Figure 6.19 through Figure 6.23 show probability density functions for the 822 valid acceleration scale factors and biases, body rate scale factors and biases, and misalignments. In each figure, there is a histogram and a Gaussian density function. The histogram is constructed with an optimal number of bins k based on Scott's method[63] that range from 16 to 21 depending on the parameter. The Gaussian density function is constructed with the means μ obtained from the 822 valid trajectories (see Table 4.5) and the corresponding standard deviations σ (recall that these are the same means and variances used to generate new dispersed trajectories for INSTAR iteration 2).

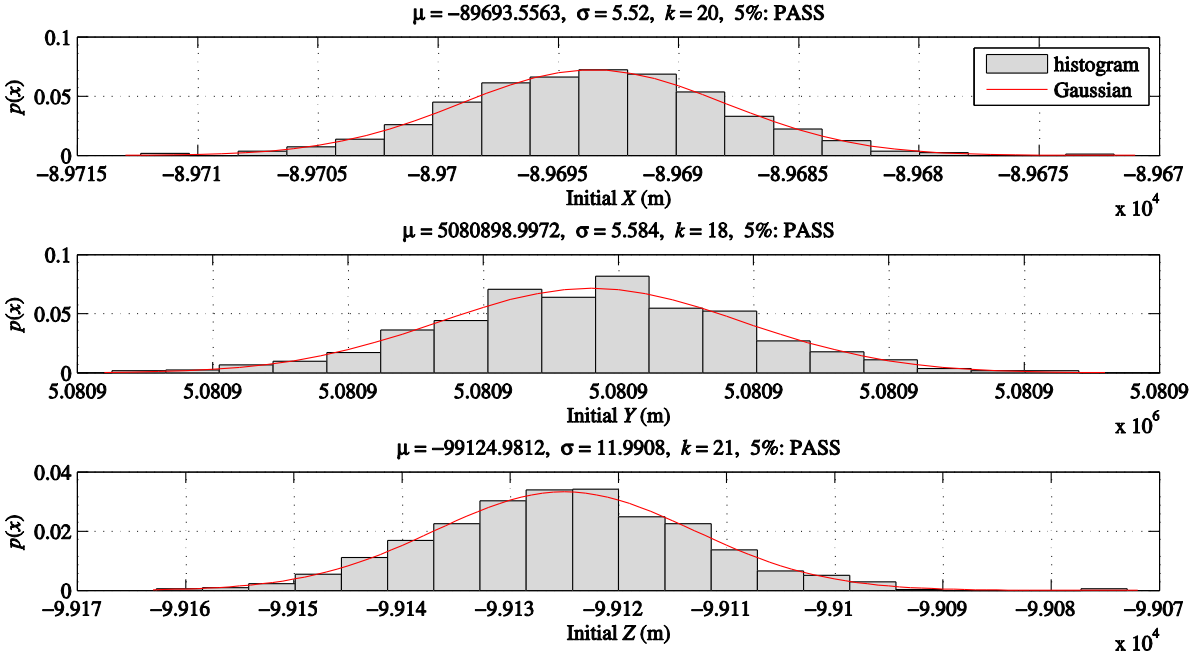

Figure 6.16. Initial position probability densities of valid trajectories, 1st iteration.

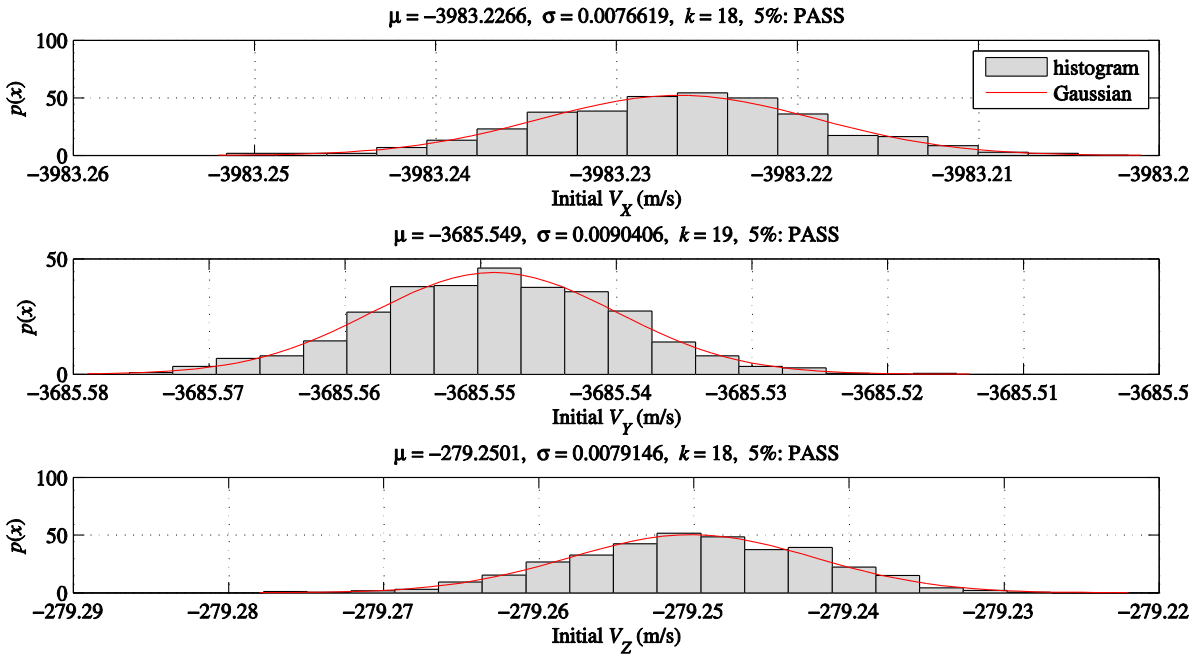

Figure 6.17. Initial velocity probability densities of valid trajectories, 1st iteration.

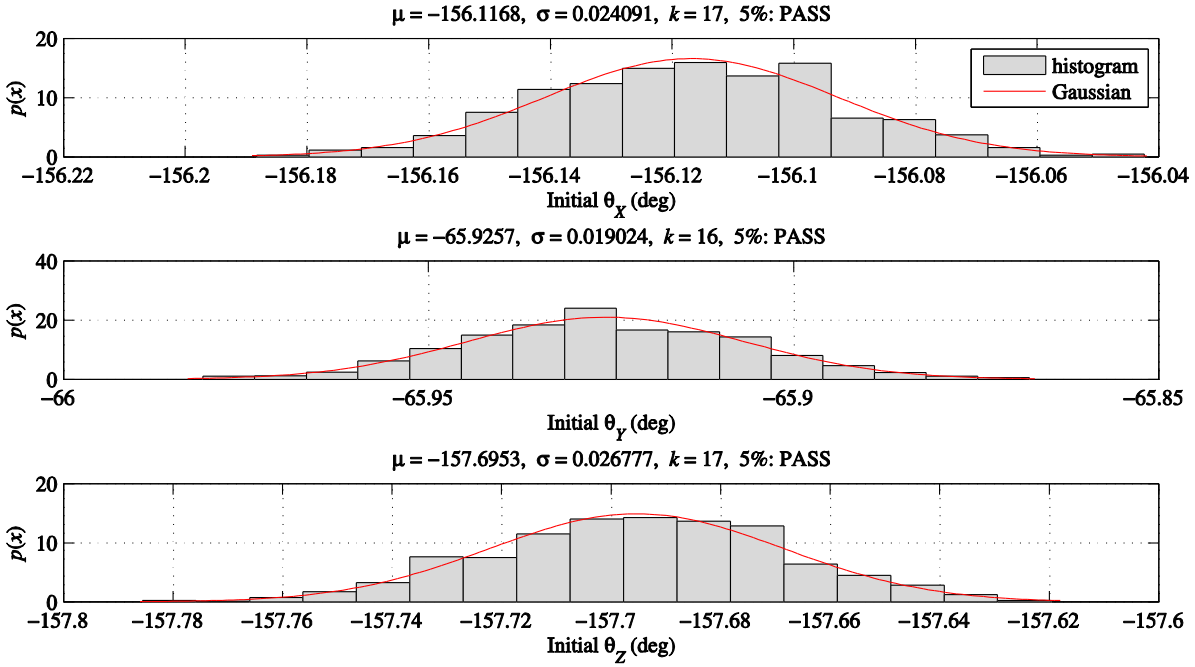

Figure 6.18. Initial attitude probability densities of valid trajectories, 1st iteration.

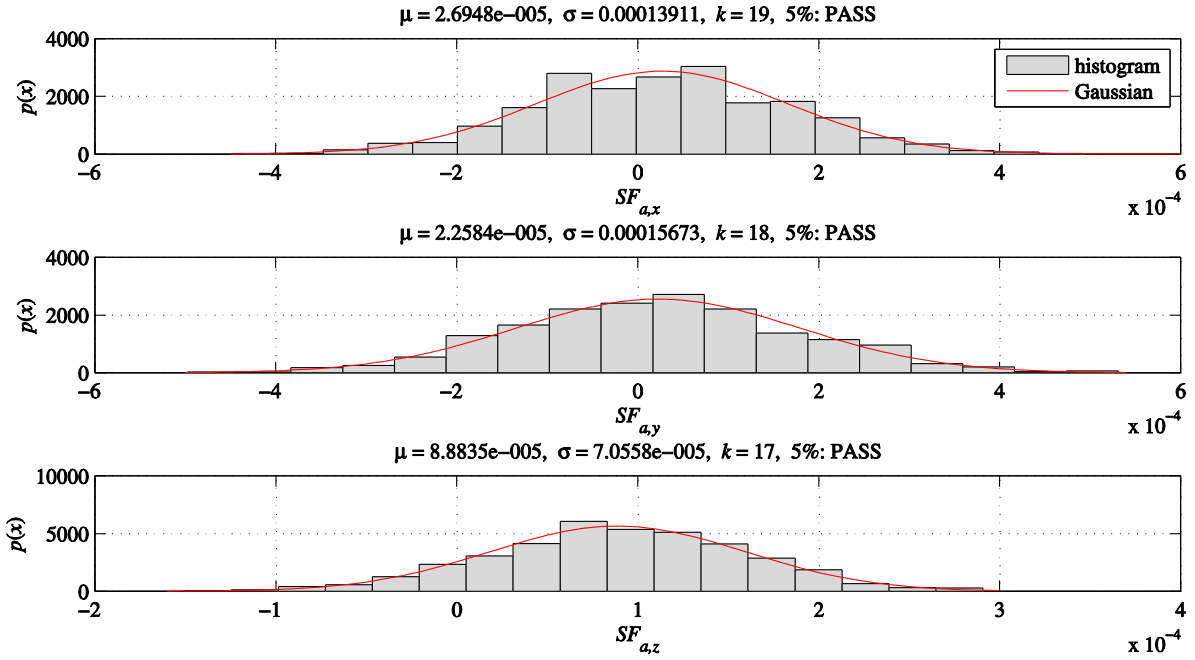

Figure 6.19. Accelerometer scale factor probability densities of valid trajectories, 1st iteration.

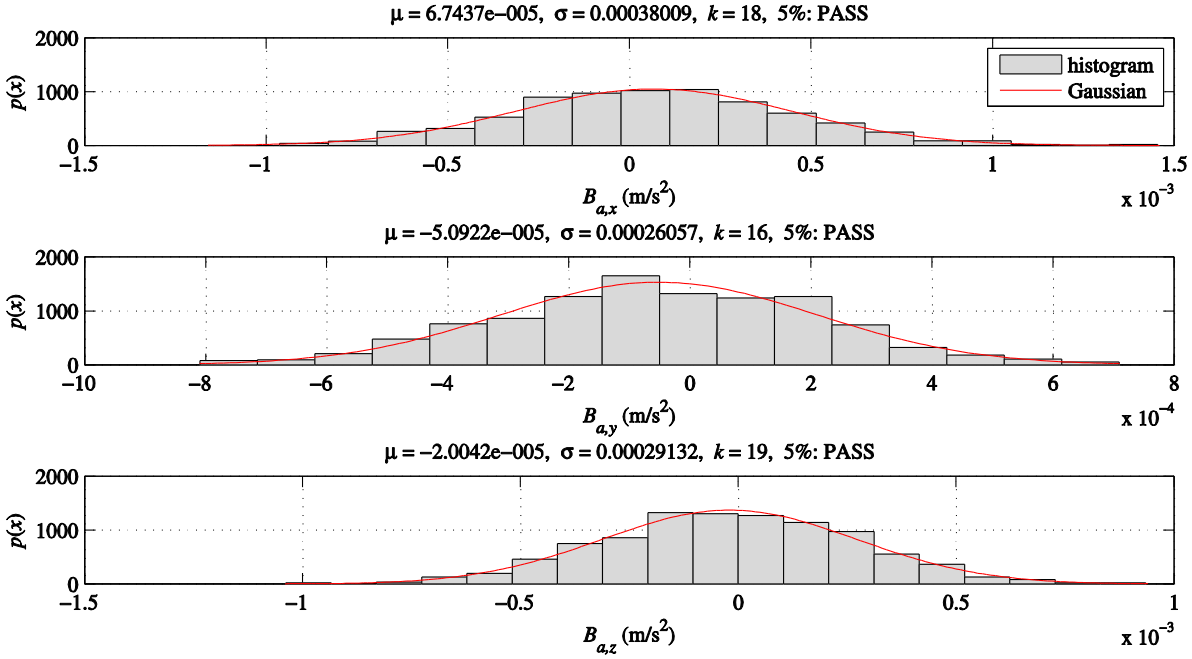

Figure 6.20. Accelerometer bias probability densities of valid trajectories, 1st iteration.

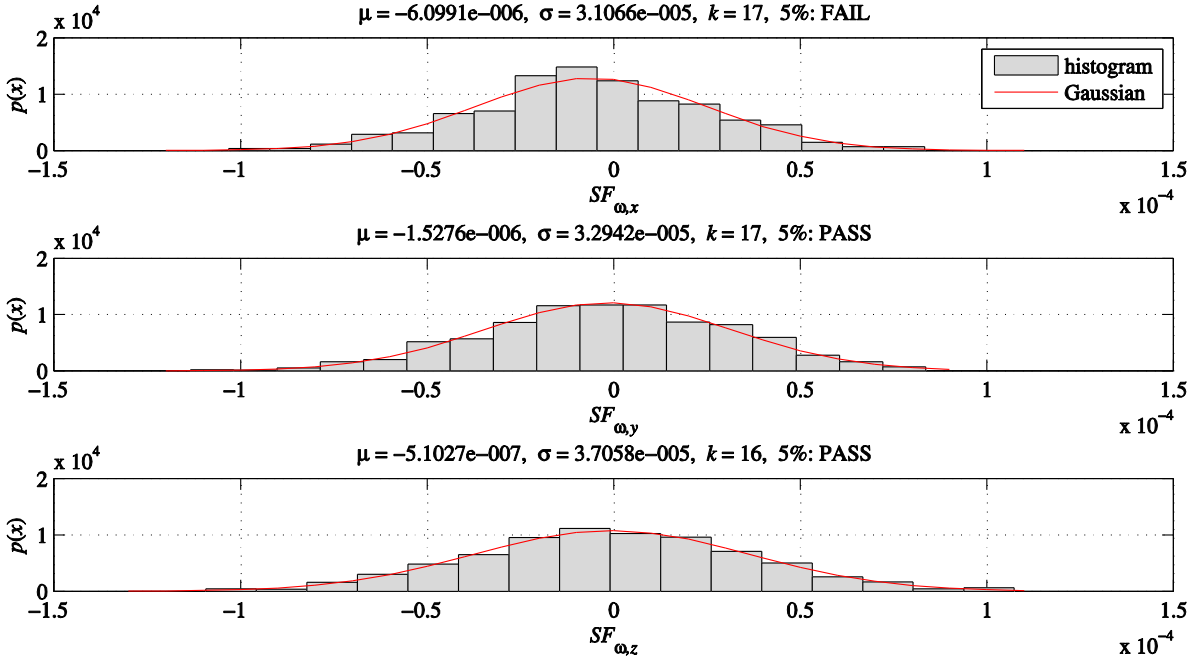

Figure 6.21. Gyroscope scale factor probability densities of valid trajectories, 1st iteration.

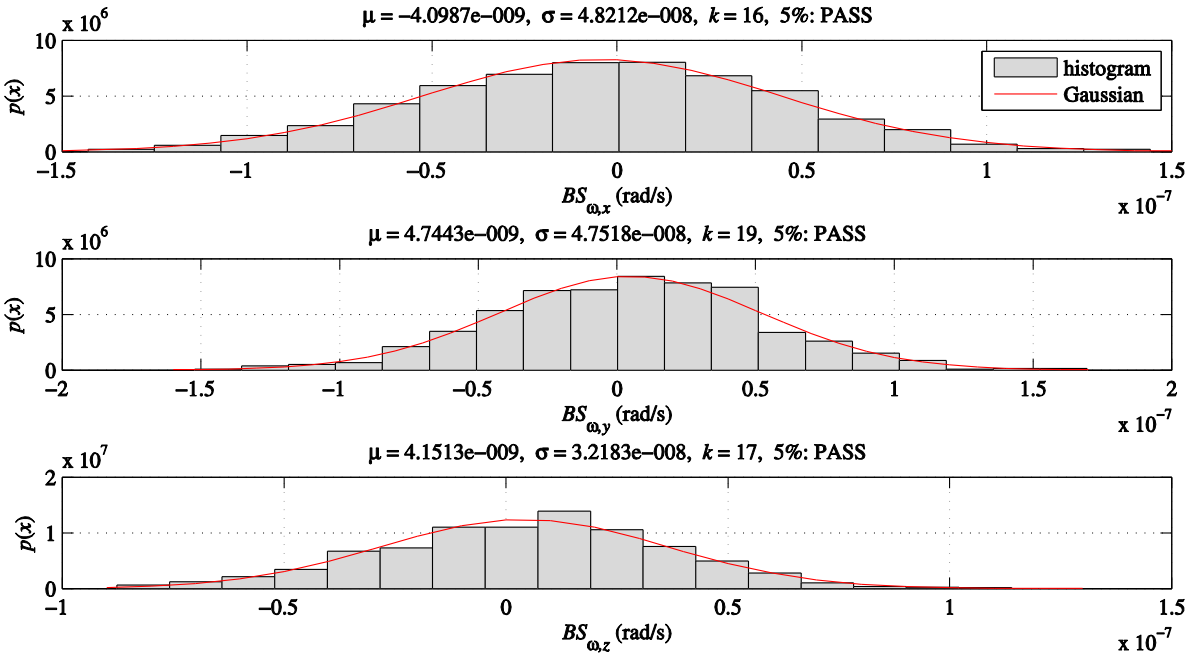

Figure 6.22. Gyroscope bias probability densities of valid trajectories, 1st iteration.

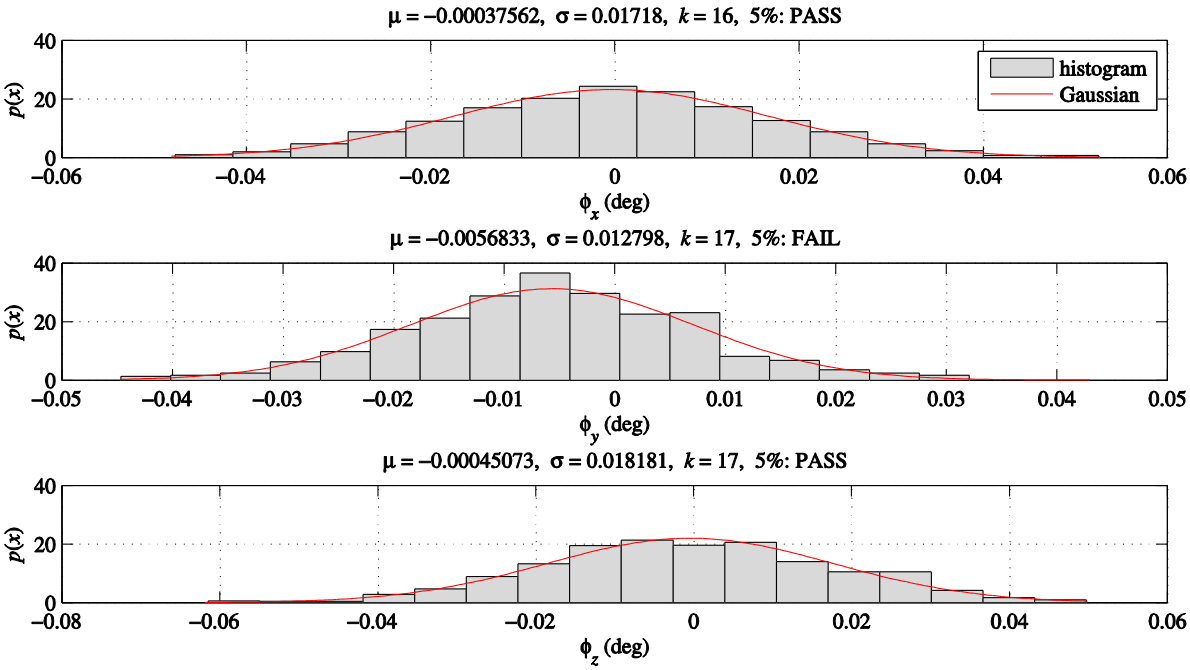

Figure 6.23. Misalignment probability densities of valid trajectories, 1st iteration.

To test the Gaussian assumption, a chi-squared goodness-of-fit test is applied to each set of 822 observations with the same number of optimal bins as the histograms (obtained using Scott's method) and a standard significance level of 5%. With the exception of the *x*-axis gyroscope scale factor and the *y*-axis misalignment, all of the parameters pass the test, indicating that in general the Gaussian assumption used to generate new initial conditions is, in this case, sufficiently accurate.

The tests are also applied to subsequent INSTAR iterations. Results are similar, although in some iterations all parameters pass the test and in other cases, a parameter other than *x*-axis gyroscope scale factor or *y*-axis misalignment fails the test. These are listed in Table 6.5.

Table 6.5. Summary of initial condition and IMU error goodness-of-fit tests for all INSTAR iterations.

Parameter	Iteration 1	Iteration 2	Iteration 3	Iteration 4	Iteration 5	Iteration 6
X_i	PASS	PASS	PASS	PASS	PASS	PASS
Y_i	PASS	PASS	PASS	PASS	PASS	PASS
Z_i	PASS	PASS	PASS	PASS	PASS	PASS
$V_{X,i}$	PASS	PASS	PASS	PASS	PASS	PASS
$V_{Y,i}$	PASS	PASS	**FAIL**	PASS	PASS	PASS
$V_{Z,i}$	PASS	PASS	PASS	PASS	**FAIL**	PASS
$\theta_{X,i}$	PASS	PASS	PASS	**FAIL**	PASS	PASS
$\theta_{Y,i}$	PASS	PASS	PASS	PASS	PASS	PASS
$\theta_{Z,i}$	PASS	PASS	PASS	PASS	PASS	PASS
$SF_{a,x}$	PASS	**FAIL**	PASS	PASS	PASS	PASS
$SF_{a,y}$	PASS	PASS	PASS	PASS	PASS	PASS
$SF_{a,z}$	PASS	PASS	PASS	PASS	PASS	PASS
$B_{a,x}$	PASS	PASS	PASS	PASS	PASS	PASS
$B_{a,y}$	PASS	PASS	PASS	PASS	PASS	PASS
$B_{a,z}$	PASS	PASS	PASS	PASS	PASS	PASS
$SF_{\omega,x}$	**FAIL**	PASS	PASS	**FAIL**	PASS	PASS
$SF_{\omega,y}$	PASS	PASS	PASS	PASS	PASS	PASS
$SF_{\omega,z}$	PASS	PASS	PASS	PASS	PASS	PASS
$B_{\omega,x}$	PASS	PASS	PASS	**FAIL**	PASS	PASS
$B_{\omega,y}$	PASS	PASS	PASS	PASS	PASS	PASS
$B_{\omega,z}$	PASS	PASS	PASS	PASS	PASS	PASS
ϕ_x	PASS	PASS	PASS	PASS	PASS	PASS
ϕ_y	**FAIL**	PASS	PASS	PASS	PASS	PASS
ϕ_z	PASS	PASS	PASS	PASS	PASS	PASS

In most cases the data satisfy the chi-squared goodness-of-fit test at a 5% significance level. However, some parameters fail this test, i.e., they are likely non-Gaussian. These distributions are checked again at the less-stringent 1% significance level, and in each case the distributions that failed at the 5% significance level pass at the 1% significance level, with two exceptions: the *x*-axis gyroscope scale factor for iteration 4 and the *Z*-axis velocity for iteration 5. Thus, in future INSTAR

applications, it will be of interest to generate the random initial conditions using an estimate of the density function, rather than assuming a Gaussian distribution.

6.4.2 Landing Condition Probability Densities

Similar checks and tests are carried out on the final landed position. Recall that although the final positions are not dispersed using a particular distribution (they are simply computed by mapping the initial conditions down using inertial navigation), they are used to determine which trajectories are valid. The probability densities of the areocentric latitude, East longitude and radius at the landing conditions of all 1,000 trajectories for INSTAR iteration 1 are shown in Figure 6.24. Note that latitude and longitude are shown in degrees. As before, shown are histograms and Gaussian densities. Note that unlike the initial conditions, the assumed distribution at the landing site is uniform rather than Gaussian. The Gaussian densities are therefore shown here as a matter of interest. The histograms are again constructed using the optimal number of bins specified by Scott's method.[63]

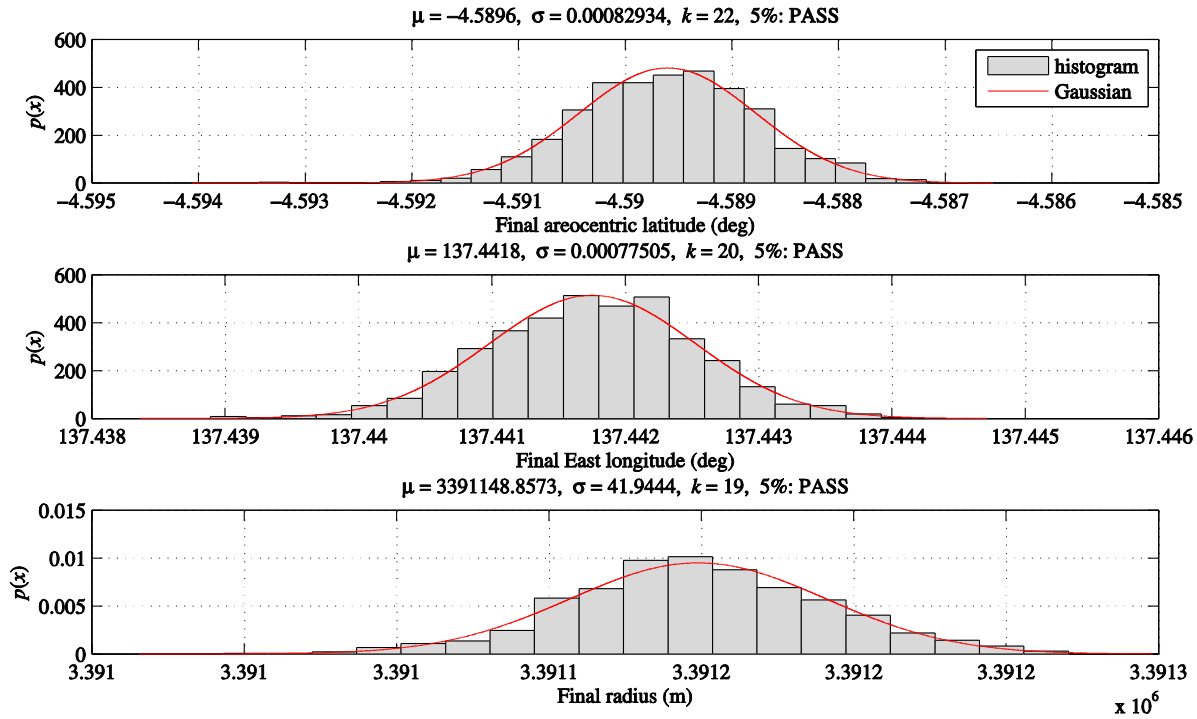

Figure 6.24. Probability density functions at landing conditions of all trajectories, 1st iteration.

For this iteration, all three parameters pass the chi-squared goodness-of-fit test at a 5% significance level, indicating that the densities are near-Gaussian. Moreover, the distributions are clearly not uniform, which is the assumption used in determining which trajectories are valid. Recall that the uniform probability density assumption relates to the information (or rather, the lack of information) regarding the reference landing site uncertainty, which is simply assumed to be accurate to within 150 meters.

The chi-squared goodness-of-fit test at a 5% significance level is repeated for the final positions of each subsequent INSTAR iteration, the results of which are listed in Table 6.6. It can be seen that all of the densities are indeed near-Gaussian. Thus, assuming that the initial conditions are normally distributed results in trajectories with normally distributed final positions.

Table 6.6. Summary of landing condition goodness-of-fit tests for all INSTAR iterations.

Parameter	Iteration 1	Iteration 2	Iteration 3	Iteration 4	Iteration 5	Iteration 6
Areocentric latitude	PASS	PASS	PASS	PASS	PASS	PASS
East longitude	PASS	PASS	PASS	PASS	PASS	PASS
Radius	PASS	PASS	PASS	PASS	PASS	PASS

The start of an INSTAR iteration is formulated with a trajectory being either valid or invalid. The *probability* of a particular trajectory occurring is determined afterwards and does not necessarily impact the value of the estimates or uncertainties. Thus, INSTAR trajectory results may be interpreted in a probabilistic sense by using histogram approximations. The same techniques may be applied to the reconstructed atmospheres by estimating the probability densities at any point along the trajectory.

6.4.3 INSTAR Convergence Analysis

A convergence analysis is carried out to determine if the INSTAR solutions presented in Table 6.1 and Table 6.2 may be obtained when beginning from a different set of *a priori* initial conditions and IMU errors. Recall that the presented solution, which will be referred to here as the *original solution*, was obtained by dispersing all 24 parameters simultaneously. To conduct the convergence analysis, first only the initial state conditions (position, velocity, and orientation) and acceleration biases are dispersed and estimated.[*] After these twelve parameters have converged, the remaining 12 IMU error parameters are considered by including their uncertainties in the covariance, and the iteration process is continued until a second convergence, or *test solution*.

[*] Ref. 24 discusses how the reference landing location cannot be "captured" by initial state dispersions only. It was determined that including acceleration biases is both reasonable and enables "capture" of the landing site. The solutions presented in that study, which only solved for the initial state and acceleration biases, were within one to two standard deviations from the *a priori* values.

The test process converges (using a 98.5% convergence criteria) in 13 iterations: six iterations to converge on the 12 initial conditions and acceleration biases, and seven more to converge on all subsequent 24 parameters. Table 6.7 lists and compares the original and test initial condition solutions and standard deviations computed from the Monte Carlo dispersions. Table 6.8 lists and compares the original and test IMU error parameter solutions and standard deviations computed from the Monte Carlo dispersions. The Δ convention is Test – Original so that a negative Δ indicates that the test value is smaller.

Table 6.7. Comparison of converged initial conditions and uncertainties, original and test cases.

Parameter	Units	Initial conditions		Standard deviations		ΔIC	$\Delta\sigma$	ΔIC as σ
		Original	Test	Original	Test			
X_i	m	-89693.52	-89693.18	5.60	7.14	3.44E-01	1.54	0.06
Y_i	m	5080898.88	5080899.72	5.52	6.76	8.43E-01	1.24	0.15
Z_i	m	-99125.16	-99121.38	12.54	17.04	3.78E+00	4.50	0.30
$V_{X,i}$	m/s	-3983.23	-3983.22	7.43E-03	5.60E-03	2.07E-03	-1.82E-03	0.28
$V_{Y,i}$	m/s	-3685.55	-3685.55	8.78E-03	6.34E-03	-6.20E-04	-2.45E-03	-0.07
$V_{Z,i}$	m/s	-279.25	-279.25	8.07E-03	8.24E-03	2.54E-03	1.73E-04	0.31
$\theta_{X,i}$	deg	-156.12	-156.12	2.45E-02	2.56E-02	-5.56E-04	1.02E-03	-0.02
$\theta_{Y,i}$	deg	-65.93	-65.92	1.84E-02	8.42E-03	6.83E-03	-9.94E-03	0.37
$\theta_{Z,i}$	deg	-157.70	-157.69	2.50E-02	2.80E-02	1.03E-03	2.93E-03	0.04

Table 6.8. Comparison of converged IMU errors and uncertainties, original and test cases.

Parameter	Units	IMU errors		Standard deviations		ΔIC	$\Delta\sigma$	ΔIC as σ
		Original	Test	Original	Test			
$SF_{a,x}$	--	2.54E-05	-1.38E-05	1.49E-04	1.34E-04	-3.93E-05	-1.55E-05	-0.26
$SF_{a,y}$	--	2.27E-05	-7.98E-06	1.67E-04	1.48E-04	-3.07E-05	-1.85E-05	-0.18
$SF_{a,z}$	--	8.77E-05	4.18E-06	6.27E-05	3.39E-05	-8.36E-05	-2.88E-05	-1.33
$B_{a,x}$	μg	6.54	-9.22	38.97	30.71	-1.58E+01	-8.26	-0.40
$B_{a,y}$	μg	-4.92	-13.17	25.06	31.49	-8.25E+00	6.43	-0.33
$B_{a,z}$	μg	-2.65	-35.73	27.07	15.27	-3.31E+01	-11.80	-1.22
$SF_{\omega,x}$	--	-6.37E-06	-1.68E-06	2.99E-05	3.31E-05	4.69E-06	3.23E-06	0.16
$SF_{\omega,y}$	--	-1.07E-06	1.73E-06	3.15E-05	3.08E-05	2.80E-06	-7.62E-07	0.09
$SF_{\omega,z}$	--	-6.77E-08	-5.11E-06	3.59E-05	3.08E-05	-5.04E-06	-5.17E-06	-0.14
$B_{\omega,x}$	deg/s	-2.16E-07	-1.99E-07	2.73E-06	2.71E-06	1.71E-08	-2.13E-08	0.01
$B_{\omega,y}$	deg/s	2.50E-07	-4.94E-07	2.56E-06	2.82E-06	-7.44E-07	2.54E-07	-0.29
$B_{\omega,z}$	deg/s	2.50E-07	-3.82E-07	2.22E-06	2.52E-06	-6.32E-07	2.95E-07	-0.28
ϕ_x	deg	-7.17E-04	-3.82E-05	1.68E-02	6.28E-03	6.79E-04	-1.06E-02	0.04
ϕ_y	deg	-5.78E-03	-1.69E-05	1.31E-02	6.96E-03	5.77E-03	-6.19E-03	0.44
ϕ_z	deg	-4.88E-04	1.73E-03	1.84E-02	1.51E-02	2.22E-03	-3.31E-03	0.12

Several observations may be made from these tables. Roughly half (11 of 24) of the standard deviations from the test solution are smaller in magnitude than those from the original solution. Furthermore, nearly all of the standard deviations are on the same order of magnitude. Thus, it may be said that the uncertainties from both solutions are comparable, and neither solution offers a uniformly smaller covariance.

Nearly every difference in converged initial conditions and IMU errors is below the 1σ value from the original solution. The two exceptions are the *z*-axis acceleration scale factor and the *z*-axis acceleration bias, both of which are below 2σ. While the standard deviations are still similar in this statistical sense, it is worth noting that the body *z*-axis is parallel to the flight trajectory. Thus, the INSTAR solution is particularly sensitive to these two parameters, which is an intuitive result as the trajectory is sensitive to axial accelerations. To illustrate this, it is useful to examine the correlations between these two parameters by computing the *correlation matrix*.

Consider a covariance Γ and let Φ be a square diagonal matrix with diagonal values given by the variances of Γ, i.e., $\Phi = \sqrt{\text{diag}(\Gamma)}$. The correlation matrix, which is positive semi-definite, is then given by

$$\mathrm{R} = \Phi^{-1}\Gamma\Phi^{-1} \tag{6.1}$$

The correlation matrix is computed for the converged "original" solution covariance. Thus, the variances are precisely the final standard deviations presented in Table 6.1 and Table 6.2. A "heat map" is generated from this correlation matrix, such that elements with higher correlations are lighter and lower correlations are darker. This heat map is shown in Figure 6.25. The diagonals of the matrix are unity. The highest correlations, at 0.8449, are between the 12th and 15th variables. The 12th variable is the *z*-axis acceleration scale factor, and the 15th variable is the *z*-axis acceleration bias, which are the two variables that changed the most between the original and test solutions. The next-highest correlations, at -0.7397, are between the *x*- and *y*-axis Euler angles.

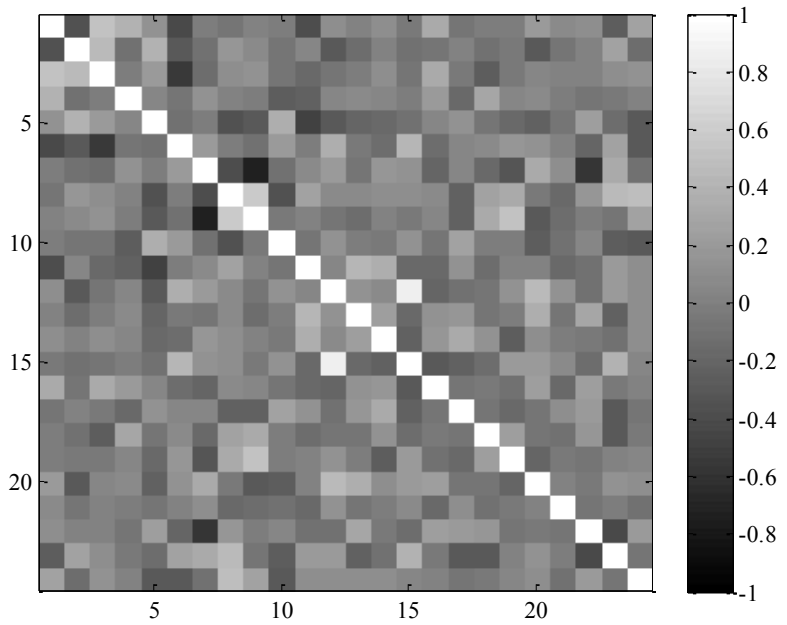

Figure 6.25. Heat map of correlation matrix, final INSTAR iteration.

In summary, the similarity between the original and test solutions indicate that if the initial conditions and IMU errors are within one or two standard deviations from the *a priori* conditions, the INSTAR process will converge on solutions that are within one or two standard deviations from each other.

Chapter 7: Summary and Conclusions

The bulk of this dissertation is based on a recently-developed data-driven navigation approach to EDL trajectory reconstruction. The process, called Inertial Navigation Statistical Trajectory and Atmosphere Reconstruction (INSTAR), utilizes inertial navigation and classical atmosphere reconstruction techniques to deterministically reconstruct a trajectory without the use of aerodynamic, control, or noise models. Statistics and redundant data are introduced into the INSTAR process using Monte Carlo dispersion techniques.

7.1 Summary of Dissertation

The purpose of this dissertation was to formally develop an alternative to traditional statistical approaches to EDL reconstruction, to implement it using flight data with multiple sources of redundant observations, and to compare the resultant parameter estimates and uncertainties to those from corresponding Kalman filter solutions. Pursuant to these objectives, a method was introduced to consider FADS pressures using a technique based on inertial navigation to reconstruct the trajectory and atmosphere along the flight path of a blunt-body entry vehicle. The method augments the INSTAR approach and assumes that the trajectory solution and uncertainties could not be appreciably improved after introducing landing site location as a redundant observation in INSTAR.

The method developed in this dissertation was demonstrated using flight data from the Mars Science Laboratory entry vehicle, which contained an IMU and a flush air data system called MEADS. An MSL trajectory and atmosphere solution that was updated using landing site location in INSTAR was first presented. This solution and corresponding uncertainties, which were obtained from Monte Carlo dispersions, was then used in a minimum variance algorithm to obtain aerodynamic estimates and uncertainties from the MEADS observations. MEADS-derived axial force

coefficient and freestream density estimates and uncertainties were also derived from the minimum variance solutions independent of the CFD-derived axial force coefficients, which have relatively high *a priori* uncertainty. Results from probabilistic analyses of the solutions were also presented.

This dissertation also introduced a method to consider correlated CFD uncertainties in INSTAR. From *a priori* CFD uncertainties, CFD force and pressure coefficients were dispersed in a Monte Carlo sense and carried over into the reconstructions. An analysis of the subsequent effects on the trajectory, atmosphere, and aerodynamic estimates and statistics was presented.

There was favorable agreement between trajectory, atmospheric, and aerodynamic estimates and the extended Kalman filter solutions obtained by the MSL reconstruction team at NASA Langley Research Center. The MEADS-derived uncertainties obtained through the methods from this work were generally smaller in magnitude because of the assumptions made regarding systematic error sources in the MEADS pressure transducer uncertainties. Using data-derived uncertainties in the pressure measurement noise covariance resulted in aerodynamic estimate uncertainties that were in better agreement with the uncertainties derived from Monte Carlo dispersions. CFD database errors dominated the uncertainties of parameters derived from aerodatabase axial force coefficients.

The following conclusions may be drawn:

- Small adjustments to the initial conditions and IMU errors that are within the *a priori* uncertainties results in a trajectory solution that lands within ten meters of the reference landing site.
- Differences between INSTAR and MEADS freestream density solutions, on the order of 1-4%, are due to differences in axial force coefficient solutions. Specifically, CFD-based axial force coefficient solutions are lower in magnitude than those from MEADS by 1-4%. This is also consistent with differences in solutions that are derived from freestream density, such as dynamic pressure.
- The MEADS dynamic pressure estimate is determined primarily by the pressure at the port nearest to the stagnation point, a region that is well-characterized by CFD and supported by analytical flowfield solutions. Thus, the MEADS dynamic pressure estimate is independent of the surface pressure coefficient distribution, which have higher CFD solution variances due in part to lack of analytical solutions near the edges of the heat shield. This distribution directly influences the CFD axial force coefficients and increases the associated uncertainties. Using a minimum variance algorithm with Monte Carlo dispersion techniques permits the recovery of axial force coefficient and density estimates from MEADS pressures independent of the CFD surface pressure coefficient distribution.
- The minimum variance equations assume random measurement uncertainties, i.e., noise. However, *a priori* MEADS measurement uncertainties contain contributions from systematic errors, resulting in inflated aerodynamic parameter uncertainties that approximate the true

and unknowable uncertainties. By computing noise-only uncertainties from the measurements, new aerodynamic parameter uncertainties are obtained that are closer in magnitude to the uncertainties obtained from Monte Carlo dispersions. The true and unknowable aerodynamic and atmospheric uncertainties therefore are bounded by the noise-only uncertainties and the INSTAR uncertainties that are dominated by CFD errors.

- Use of Gaussian distributions for initial conditions during the INSTAR process is, in general, not an unreasonable assumption, although in some cases some parameters do not satisfy the chi-squared goodness-of-fit test for normal distributions. Furthermore, assuming Gaussian distributions for initial conditions result in Gaussian distributions for landing site parameters. It will be of interest to include more accurate probability density distributions in future INSTAR applications.
- Running the INSTAR process with different *a priori* initial conditions and IMU errors results in solutions that are within one or two standard deviations from each other. The largest differences are in the axial acceleration scale factor and bias, which are highly correlated.

7.2 Concluding Remarks

While the fundamental concept of INSTAR has been demonstrated in this dissertation, it is continually being updated and refined. Major avenues of investigation include inclusion of MSL altimetry information as a redundant data source, implementing MEADS pressure observations within INSTAR without using a statistical algorithm, using observation probability distributions to inform trajectory updates in INSTAR, using a more accurate CFD surface pressure uncertainty model, and correlating dispersions in CFD surface pressures to CFD axial force coefficients.

There is ample opportunity to apply INSTAR to flight data in the coming years. At the time of this writing, there are two NASA Mars EDL missions in planning stages. The Discovery-class Mars Interior Exploration using Seismic Investigations, Geodesy, and Heat Transport (InSight) mission is scheduled to launch in 2016, and a re-fly of Mars Science Laboratory mission is scheduled for a 2020 launch. Although InSight will not carry a MEADS-like flush air data system, the MSL re-fly will use a revised MEADS design tentatively called MEADS+, with potential for additional ports on the backshell to measure base pressure. In either case, the INSTAR process will still be applicable with other redundant data, and in the case of the MSL re-fly, the techniques described in this dissertation may be used.

The INSTAR technique, however, is not limited to Mars missions or even EDL. It may be applied to any data set that includes information from an inertial measurement unit and at least one piece of additional data. It is the hope of this author that INSTAR may continue to be refined and used in parallel with statistical techniques to provide a comparable method of obtaining useful statistics in post-flight reconstructions.

References

1. Woodfill, J., "How Columbus and the Apollo Astronauts Navigated," NASA Johnson Space Center, URL: http://er.jsc.nasa.gov/seh/navigate.htm [cited 11 October 2013].

2. Peck, D. T., Cristoforo Colombo – God's Navigator, Columbian Publishers, Columbus, WI, 1993, pp. 51-115.

3. MacKenzie, D. A., *Inventing Accuracy: A Historical Sociology of Nuclear Missile Guidance*, The MIT Press, Cambridge, MA, 1990.

4. Titterton, D., and Weston, J., *Strapdown and Inertial Navigation Technology*, The Institution of Electrical Engineers, Cornwall, UK, 2004, 2nd Edition.

5. Grewal, S. M., Weill, L. R., and Andrews, A. P., *Global Positioning Systems, Inertial Navigation, and Integration*, John Wiley & Sons, Inc., New York, NY, 2001.

6. Braun, R. D., and Manning, R. M., "Mars Exploration Entry, Descent, and Landing Challenges," *Journal of Spacecraft and Rockets*, Vol. 44, No. 2, March-April 2007, pp. 310-23.

7. Hopper, F. W., "Trajectory, Atmosphere, and Wind Reconstruction from Viking Measurements," AAS/AIAA Astrodynamics Specialist Conference, Nassau, Bahamas, July 1975, AAS 75-068.

8. Ingoldby, R. N., Michel, F. C., Flaherty, T. M., Doty, M. G., Preston, B., Villyard, K. W., and Steele, R. D., "Entry Data Analysis for Viking Landers 1 and 2 Final Report," Martin Marietta Corporation, NASA TN-3770218 (also NASA CR-159338), November 1976.

9. Euler, E. A., Adams, G. L., and Hopper, F. W., "Design and Reconstruction of the Viking Lander Descent Trajectories," *Journal of Guidance and Control*, Vol. 1, No. 5, September-October 1978, pp. 372-8.

10. Spencer, D. A., Blanchard, R. C., Braun, R. D., Kallemeyn, P. H., and Thurman, S. W., "Mars Pathfinder Entry, Descent, and Landing Reconstruction," *Journal of Spacecraft and Rockets*, Vol. 36, No. 3, May-June 1999, pp. 357-66.

11. Blanchard, R. C., "Entry Descent and Landing Trajectory and Atmosphere Reconstruction for the Mars Exploration Rovers Missions A and B," The George Washington State University, Contractor Report, April 2008.

12. Blanchard, R. C., and Desai, P. N., "Mars Phoenix Entry, Descent, and Landing Trajectory and Atmosphere Reconstruction," *Journal of Spacecraft and Rockets*, Vol. 48, No. 5, September-October 2011, pp. 809-21.

13. Sheehan, W., *The Planet Mars: A History of Observation and Discovery*, The University of Arizona Press, Tuscon, AZ, 1996.

14. Seiff, A., "Some Possibilities for Determining the Characteristics of the Atmospheres of Mars and Venus from Gas-Dynamic Behavior of a Probe Vehicle," National Aeronautics and Space Adminsitration, Washington, NASA TN D-1770, 1963.

15. Seiff, A., and Reese, D. E., "Use of Entry Vehicle Responses to Define the Properties of the Mars Atmosphere," *Advances in the Astronautical Sciences*, Vol. 19, 1965, pp. 419-44.

16. McKim, R., "The dust storms of Mars," *Journal of the British Astronomical Association*, Vol. 106, No. 4, 1996, pp. 185-200.

17. Williams, D. R., "Mars Fact Sheet," *Planetary Fact Sheets* [online database], NASA Goddard Space Flight Center, URL: http://nssdc.gsfc.nasa.gov/planetary/factsheet/marsfact.html [cited 23 July 2013].

18. Oberkampf, W. L., and Trucano, T. G., "Verification and validation in computational fluid dynamics," *Progress in the Aerospace Sciences*, Vol. 38, 2002, pp. 209-72.

19. "Guide for the Verification and Validation of Computational Fluid Dynamics Simulations," American Institute of Aeronautics and Astronautics, 1998, AIAA Guide G-077-1998, Chap. 2.

20. Crassidis, J. L., and Junkins, J. L., *Optimal Estimation of Dynamic Systems*, Chapman & Hall/CRC, Washington, D.C., 2004.

21. Gelb, A., *Applied Optimal Estimation*, The MIT Press, Cambridge, MA, 1974.

22. Wertz, J. R., *Spacecraft Attitude Determination and Control*, D. Reidel Publishing Company, Dordrecht, Holland, 1978, Chap. 13.

23. Huh, L., "Statistical Analysis of the Uncertainty in Pre-Flight Aerodynamic Database of a Hypersonic Vehicle," Dissertation, Department of Mechanical and Aerospace Engineering, North Carolina State University, Raleigh, NC, 2012.

24. Blanchard, R. C., Tolson, R. H., Lugo, R. A., Huh, L., "Inertial Navigation Entry, Descent, and Landing Reconstruction using Monte Carlo Techniques," 23rd AAS/AIAA Spaceflight Mechanics Meeting, Kauai, HI, February 2013, AAS 13-308.

25. Pruett, C. D., Wolf, H., Heck, M. L., and Siemers, P. M., "Innovative Air Data System for the Space Shuttle Orbiter," *Journal of Spacecraft and Rockets*, Vol. 20, No. 1, January-February 1983, pp. 61-69.

26. Siemers III, P. M., Henry, M. W., and Flanagan, P.F., "Shuttle Entry Air Data System Concepts Applied to Space Shuttle Orbiter Flight Pressure Data to Determine Air Data – STS 1-4," 21st AIAA Aerospace Sciences Meeting, Reno, NV, January 1983, AIAA 83-0118.

27. Baumann, E., Pahle, J. W., Davis, M. C., and White, J. T., "X-43A Flush Airdata Sensing System Flight-Test Results," *Journal of Spacecraft and Rockets*, Vol. 47, No. 1, January-February 2010, pp. 48-61.

28. Sebastian, T., and Tolson, R. H., "Methods for the Determination of Aerodynamic Parameters and Trajectory Reconstruction of the Orion Command Module from Scale Model Aeroballistic Flight Data," 47th AIAA Aerospace Sciences Meeting including the New Horizons Forum and Aerospace Exposition, Orlando, FL, January 2009, AIAA 2009-882.

29. Lugo, R. A., "Methods of Flight Parameter Recovery from Orion Crew Module Using Scale Model Aeroballistic Flight Data," Master's Thesis, Department of Mechanical and Aerospace Engineering, North Carolina State Univ., Raleigh, NC, 2011.

30. Lugo, R. A., Tolson, R. H., and Schoenenberger, M., "Trajectory Reconstruction and Uncertainty Analysis using Mars Science Laboratory Pre-Flight Scale Model Aeroballistic Testing," 51st AIAA Aerospace Sciences Meeting including the New Horizons Forum and Aerospace Exposition, Grapevine, TX, January 2013, AIAA 2013-1132.

31. Karlgaard, C. D., Beck, R. E., O'Keefe, S. A., Siemers, P. M., White, B. A., Engelund, W. C., and Munk, M. M., "Mars Entry Atmospheric Data System Modeling and Algorithm Development," 41st AIAA Thermophysics Conference, San Antonio, TX, June 2009, AIAA 2009-3916.

32. Karlgaard, C. D., Kutty, P., Schoenenberger, M., Shidner, J., and Munk, M. M., "Mars Entry Atmospheric Data System Trajectory Reconstruction and Flight Results," 51st AIAA Aerospace Sciences Meeting including the New Horizons Forum and Aerospace Exposition, Grapevine, TX, January 2013, AIAA 2013-0028.

33. Grotzinger, J. P., Crisp, J., Vasavada, A. R., Anderson, R. C., Baker, C. J., Barry, R., Blake, D. F., Conrad, P., Edgett, K. S., Ferdowski, B., Gellert, R., Gilbert, J. B., Golombek, M., Gomez-Elvira, J., Hassler, D. M., Jandura, L., Litvak, M., Mahaffy, P., Maki, J., Meyer, M., Malin, M. C., Mitrofanov, I., Simmonds, J. J., Vaniman, D., Welch, R. V., and Wiens, R. C., "Mars Science Laboratory Mission and Science Investigation," *Space Science Reviews*, Vol. 170, 2012, pp. 5-56.

34. Karlgaard, C. D., Kutty, P., Schoenenberger, M., and Shidner, J., "Mars Science Laboratory Entry, Descent, and Landing, Trajectory and Atmosphere Reconstruction," 23rd AAS/AIAA Spaceflight Mechanics Meeting, Kauai, HI, February 2013, AAS 13-307.

35. Karlgaard, C. D., Kutty, P., Schoenenberger, M., Michelle, M. M., Little, A., Kuhl, C., and Shidner, J., "Mars Entry Atmospheric Data System Trajectory and Atmosphere Reconstruction of the Mars Science Laboratory Entry, Descent, and Landing," *Journal of Spacecraft and Rockets*, submitted.

36. Schoenenberger, M., Van Norman, J. W., Karlgaard, C. D., Kutty, P., and Way, D., "Assessment of the Reconstructed Aerodynamics of the Mars Science Laboratory Entry Vehicle," *Journal of Spacecraft and Rockets*, submitted.

37. Essmiller, J., Brugarolas, P., and San Martin, M., "MSL EDL GN&C Reference Frames," PowerPoint presentation, Jet Propulsion Laboratory, Pasadena, CA, September 2012.

38. Sirlin, S. W., and Vanelli, C. A., "MSL EDL KAST MIMU Model Implementation Update," Jet Propulsion Laboratory, EM 343H, 9 January 2008.

39. Gazarik, M. J.,Wright, M. J., Little, A., Cheatwood, F. M., Herath, J. A., Munk, M. M., Novak, F. J., and Martinez, E. R., "Overview of the MEDLI Project," IEEE 2008 Aerospace Conference, March 2008.

40. Little, A., Bose, D., Karlgaard, C. D., Munk, M. M., Kuhl, C., Schoenenberger, M., Antill, C., Verhappen, R., Kutty, P., and White, T., "The Mars Science Laboratory (MSL) Entry, Descent, and Landing Instrumentation (MEDLI): Hardware Performance and Data Reconstruction," 23rd AAS/AIAA Spaceflight Mechanics Meeting, Kauai, HI, February 2013, AAS 13-078.

41. Seiff, A., "The Viking Atmosphere Structure Experiment – Techniques, Instruments, and Expected Accuracies," *Space Science Instrumentation*, Vol. 2, 1976, pp. 381-423.

42. Blanchard, R. C., and Walberg, G. D., "Determination of the Hypersonic-Continuum/Rarefied-Flow Drag Coefficient of the Viking Lander Capsule 1 Aeroshell from Flight Data," NASA TP 1793, December 1980.

43. Bose, D., White, T., Santos, J. A., Feldman, J., Mahzari, M., Olson, M., and Laub, B., "Initial Assessment of the Mars Science Laboratory Heatshield Instrumentation and Flight Data," 51st AIAA Aerospace Sciences Meeting including the New Horizons Forum and Aerospace Exposition, Grapevine, TX, January 2013, AIAA 2013-0908.

44. White, T. R., Mahzari, M., Bose, D., and Santos, J. A., "Post-flight Analysis of the Mars Science Laboratory Entry Aerothermal Environment and Thermal Protection System Response," 44th AIAA Thermophysics Conference, San Diego, CA, June 2013, AIAA 2013-2779.

45. Dyakonov, A. A., Schoenenberger, M., and Van Norman, J. W., "Hypersonic and Supersonic Static Aerodynamics of the Mars Science Laboratory Entry Vehicle," 43rd AIAA Thermophysics Conference, New Orleans, LA, June 2012, AIAA 2012-2999.

46. Schoenenberger, M., Dyakonov, A., Buning, P., Scallion, W., Van Norman, J., "Aerodynamic Challenges for the Mars Science Laboratory Entry, Descent, and Landing," 41st AIAA Thermophysics Conference, San Antonio, TX, June 2009, AIAA 2009-3914.

47. Way, D. W., Davis, J. L., and Shidner, J., "Assessment of the Mars Science Laboratory Entry, Descent, and Landing Simulation," 23rd AAS/AIAA Spaceflight Mechanics Meeting, Kauai, HI, February 2013, AAS 13-420.

48. Munk, M. M., Karlgaard, C. D., and Schoenenberger, M., "MEADS Error Budget Report," NASA Langley Research Center, MEDLI Report, 22 August 2011, MEDLI-0239 version 1.2.

49. Anderson, J. D., *Modern Compressible Flow with Historical Perspective*, McGraw-Hill, Boston, MA, 2004, 3rd Edition.

50. Anderson, J. D., *Hypersonic and High-Temperature Gas Dynamics*, American Institute of Aeronautics and Astronautics, Inc., Reston, VA, 2006, 2nd Edition.

51. "Equations, Tables, and Charts for Compressible Flow," Ames Aeronautical Laboratory, NACA TR 1135, 1953.

52. Mase, R. A., "Update to Mars Coordinate Frame Definitions," Interoffice Memorandum, Jet Propulsion Laboratory, 15 July 1999, 312.B/015-99.

53. de Vancouleurs, G., Davies, M. E., Sturms, Jr., F. M., "Mariner 9 Aerographic Coordinate System," *Journal of Geophysical Research*, Vol. 78, 1973, pp. 4395-404.

54. "atan2," The MathWorks, Inc., [online manual], URL: http://www.mathworks.com/help/matlab/ref/atan2.html [cited 2 February 2014].

55. Merriman, M., "On the History of the Method of Least Squares," Annals of Mathematics, *The Analyst*, Vol. 4, No. 2, March 1877, pp. 33-6.

56. Hamming, R. W., *Numerical Methods for Scientists and Engineers*, Dover Publications, Inc., New York, NY, 1973, 2nd Edition.

57. Metropolis, N., and Ulam, S., "The Monte Carlo Method," *Journal of the American Statistical Association*, Vol. 44, No. 247, 1949, pp. 335-41.

58. "OpenMP Application Program Interface," OpenMP Architecture Review Board, Version 4.0, July 2013, [online manual], URL: http://www.openmp.org/mp-documents/OpenMP4.0.0.pdf [cited 25 September 2013].

59. Thomson, W. T., *Introduction to Space Dynamics*, Dover Publications, Inc., New York, NY, 1986.

60. Tolson, R. H., Blackshear, W. T., and Anderson, S. G., "Orbit and Position Determination for Mars Orbiters and Landers," AIAA 8th Aerospace Sciences Meeting, New York, NY, January 1970, AIAA 70-160.

61. Sturges, H. A. "The Choice of a Class Interval," *Journal of the American Statistical Association*, Vol. 21, No. 153, 1926, pp. 65-6.

62. Freedman, D. and Diaconis, P., "On the Histogram as a Density Estimator: L2 Theory," Zeitschrift für Wahrscheinlichkeitstheorie und Verwandte Gebiete, Vol. 57, No. 4, 1981, pp. 453-76.

63. Scott, D. W., "On Optimal and Data-Based Histograms," *Biometrika*, Vol. 66, No. 3, December 1979, pp. 605-10.

64. Scott, D. W., *Multivariate Density Estimation: Theory, Practice, and Visualization*, John Wiley & Sons, 2009.

65. Pearson, K., "On the Criterion that a given System of Deviations from the Probable in the Case of a Correlated System of Variables is such that it can be reasonably supposed to have arisen from Random Sampling," *London, Edinburgh, and Dublin Philosophical Magazine and Journal of Science Series 5*, Vol. 50, Issue 302, 1900, pp. 157-75.

66. Pinier, J. T., "New Aerodynamic Data Dispersion Method with Application to Launch Vehicle Design," *Journal of Spacecraft and Rockets*, Vol. 49, No. 5, September-October 2012, pp. 834-41.